University of Silesia in Katowice

Andrzej Wilczek

Lambda production in p+p interactions at SPS energies

Doctoral Thesis

Thesis Supervisor
Prof. dr hab. W. Zipper

Thesis Co-Supervisor
Dr hab. S. Kowalski

Katowice 2015

Abstract

NA61/SHINE is an experiment, which performance is optimal for studies on the phase diagram of strongly interacting matter in a systematic way, in particular on the phase transition from hadron gas to the quark-gluon plasma (QGP), where the quarks are not confined.

Strangeness enhancement is known to be one of the key signatures of the onset of deconfinement. One of the particles carrying strangeness is Λ-hyperon. As an electrically neutral particle, it can not be easily detected in a direct way, but its track can be reconstructed by analysing its charged decay products.

The main aim of this thesis is to calculate Λ-yields and Λ mean multiplicity for p+p interactions at 158 GeV/c with the use of the NA61/SHINE data acquired in 2009, the first task being the preparation and validatation of a procedure for identification and extraction of Λ-particles for p+p at SPS energies.

The procedure was employed in order to calculate double-differential spectra $\left(\frac{d2n}{dydp_T}, \frac{d^2n}{dydm_T}, \frac{d2n}{dx_F dp_T}\right)$, single-differential distributions $\left(\frac{dn}{dy}, \frac{dn}{dx_F}\right)$, mean transverse mass $\langle m_T \rangle$, and inverse slope parameter T dependence on y, as well as mean Λ multiplicity extrapolated to 4π for p+p at 158 GeV/c.

The data obtained with p+p, where no transition to the QGP is expected, will be used as a reference for further measurements in heavy-ion collisions.

Streszczenie

NA61/SHINE stanowi eksperyment zoptymalizowany pod kątem badań diagramu fazowego silnie oddziałującej materii, w szczególności przejścia fazowego z fazy gazu hadronowego w fazę plazmy kwarkowo-gluonowej (QGP), której główną cechą jest brak uwięzienia kwarków.

Jedną z kluczowych sygnatur uwolnienia kwarków jest wzmocnienie dziwności, którą zawiera m.in. cząstka Λ. Bezpośrednia jej obserwacja, jako cząstki nienaładowanej elektrycznie, nie jest łatwa, jednakże jej ślad może być zrekonstruowany na podstawie analizy naładowanych produktów rozpadu.

Głównym celem tej pracy jest obliczenie całkowitej i różniczkowych krotności cząstki Λ dla reakcji p(158 GeV/c)+p. W tym celu przygotowano i przetestowano procedurę służącą ekstrakcji cząstek Λ spośród danych zebranych przez NA61/SHINE w oddziaływaniach p+p w zakresie pędów akceleratora SPS.

Powyższa procedura została zastosowana przy obliczeniach spektrów $\left(\frac{d2n}{dydp_T}, \frac{d^2n}{dydm_T}, \frac{d2n}{dx_F dp_T}\right)$ oraz rozkładów $\left(\frac{dn}{dy}, \frac{dn}{dx_F}\right)$, a także zależności średniej masy transwersalnej $\langle m_T \rangle$ oraz odwrotnego parametru nachylenia T od pośpieszności y, oraz średniej krotności Λ ekstrapolowanej do 4π.

Contents

Chapter 1

Introduction

The problem of pinning down the critical point of strongly interacting matter is still a maze that puzzles the community. One of the answers suspected to emerge in the near future will surely come from NA61/SHINE- a fixed-target experiment aiming to discover the critical point as well as to study the properties of the onset of deconfinement.

This goal will be reached by obtaining precise data on hadron production in proton-proton, proton-nucleus and nucleus-nucleus interactions in a wide range of system size and collision energy.

One of the signatures of the transition to the quark-gluon plasma (QGP) is the strangeness enhancement. This can be studied only if the total strangeness production is estimated for a wide range of energies. The same may concern also individual strange particles normalised to entropy. One of the particles inevitable for such an analysis is the Λ hyperon.

The effect of strangeness enhancement is only expected for the heavy-ion interactions, as the system size has to be large enough to involve an amount of individual nucleon-nucleon interactions high enough for the produced particles to overfill the available volume. One has to bear in mind, that the enhancement has to be referred to the situation, where production of the QGP is quite improbable. This is the case for nucleon-nucleon interactions.

The need for such a reference is the main reason for developing a procedure used for analysis of Λ (incl. Σ^0) production in p+p interactions at the SPS energies, which is the main topic of the thesis.

In the following, one finds the outline of this thesis. The theoretical formulation of the studies on the QGP are found in Chapter 2. The chapter begins with a short introduction to quantum chromodynamics. Then, the next topic introduced in Section 2.2 concerns the creation and the properties of the QGP, followed by the experimental evidence for the QGP (Section 2.3). The properties of the phase transition between hadron gas and the QGP, mainly from theoretical point of view, are within

the scope of the Section 2.4. The last section of this chapter (Section 2.5) is dedicated to the research program of the NA61/SHINE experiment, aiming at thorough studies on the properties of the onset on deconfinement and the critical point.

Chapter 3 is provided with the history of research on strangeness (Section 3.1), the properties of Λ-particle (Section 3.2), as well as the experimental methods of identification of electrically neutral strange particles (Section 3.3).

The following Chapter 4 is devoted to the NA61/SHINE experimental setup used for all the analyses described in this thesis.

The main part of the thesis starts with the Chapter 5. It contains an exhausting description of the analysis procedure aiming at obtaining Λ-yields. First of all, the track and main vertex reconstruction is discussed in Section 5.1, followed by the V^0 reconstruction in Section 5.2. Then, the event cuts used for the selection of inelastic events of the best quality are introduced in Section 5.3. The V^0 quality selection and the background reduction is shown in Section 5.4. The signal extraction is the topic of Section 5.5, and the corrections for efficiency, detector effects, interactions outside of the target material etc. are presented in Section 5.6. The crown jewel of this chapter is found in Section 5.7, where the equations used for yields calculations are introduced. Finally, the method of systematic uncertainty calculation applied in this thesis is described in Section 5.8.

The results and their discussion are presented in Chapter 6, in particular double-differential spectra $\left(\frac{d2n}{dydp_T}, \frac{d^2n}{dydm_T}, \frac{d2n}{dx_F dp_T}\right)$, single-differential distributions $\left(\frac{dn}{dy}, \frac{dn}{dx_F}\right)$, the $\langle m_T \rangle$ and inverse slope parameter T dependence on y, as well as mean Λ multiplicity extrapolated to 4π. The discussion of these results contain the comparison with the world data on this topic, as well as the comparison with the MC-models, that apply to the SPS energy range.

The summary and outlook is found in Chapter 7.

It is worth mentioning, which parts of the thesis are owed to the work of the author himself.

I have been involved in activities of NA61/SHINE since 2010. During preparations of this thesis, I was active as a beam expert (see Subsection 4.1.3), and as a BPD-expert (Subsection 4.2.3). I was also taking part at the data acquisition. In addition to that I was in charge of magnetic field calibration, i.e. the check for possible accidental rescaling of the magnetic field, described in Section 5.1. But the main task I was given was the analysis, being the main aspect of this thesis. Description of the Λ-analysis begins with Section 5.3 and closes with the end of the book.

The results have been shown at various specialist conferences by numerous members of the NA61/SHINE collaboration, including myself. They are ready for publication in EPJ C.

Chapter 2

The Quark-Gluon Plasma

It has been more than 50 years since the proposition of Gell-Mann [1] and Zweig [2, 3] made the classification of particles reasonable. This was for sure a milestone in the history of particle physics, just as invention of the periodic table of elements marked a watershed in the history of atomic physics and chemistry. From then on, particle physics could not be described as merely a collection of stamps - the classification of particles became transparent, and the conception of quarks smoothed the way for prediction of the properties of particles awaiting their discovery. It's further development opened the way for quantum chromodynamics and the successful conception of the Standard Model.

This chapter depicts the current situation in the research on the Quark-Gluon Plasma, and it is focused mainly on the SPS energies.

2.1 Quantum Chromodynamics

Quantum chromodynamics (QCD) is a non-abelian gauge theory with gluons as force carriers. It describes the strong interactions - known for making the bounds between nucleons inside of nuclei stable, despite of repulsive force which electromagnetically charged protons are exposed to. The irreducible particles interacting strongly are quarks and gluons. There are 6 known types of quarks: up (u), down (d), charm (c), strange (s), top (t), bottom (b), which differ not only by electric charge (which is enough to find the difference between the two lightest quarks u, and d), but the behaviour of heavy quarks in numerous processes is described as possessing strangeness (s), charm (c), truth (t), and beauty (b).

The name of the theory comes from the naming convention for charge responsible for the strong force - Greek $X\rho\acute{\omega}\mu\alpha$ means colour. The charge occurs in 3 variants. The quarks are namely red, green, or blue (RGB), whereas colours complementary to RGB: cyan, magenta, and yellow ($\bar{R}\bar{G}\bar{B}$) are reserved for anti-quarks. Gluons carry a mixture of colour and anti-colour in eight combinations.

One fact is worth underlining here: on the contrary to all the other force bosons known today, gluons are charge carriers! This has far-reaching consequences.

Nowadays it seems obvious, there are two forms of hadrons: baryons and mesons. Baryons are built of exactly three valence quarks, an immense number of sea quarks and gluons. The sea come from the vacuum polarisation. The other form of hadron matter we know are mesons, which include only two valence partons - one quark and one anti-quark.

Kinematics of the system as a whole with the binding energy caused by the gluon field contribute to the mass of hadrons, while the mass of quarks themselves (bare mass of quarks) is quite small (2-5 MeV/c^2 for the lightest quarks).

Why there are no other types of hadrons ever observed? This is well explained using the convention of colour charge. In analogy to the additive colour mixing, only combinations, which are 'white' as a whole system are allowed to be observed.

In addition to that, an introduction of the additional quantum number of colour charge made possible to bypass the problem of a spin 3/2 baryon built of 3 seemingly identical quarks, obeying Fermi statistics. If the particles were completely identical, this would contradict with the Pauli exclusion principle, which is a direct consequence of Fermi statistics. If an additional quantum number exists, it can be used to identify individual constituent quarks and to make sure, that Fermi statistics holds. This is the case for e.g. Ω^- [4] and Δ^{++} [5, 6].

One of the evident effect that arose from the quark theory, which makes the single quarks unable to be observed is the quark containment and the asymptotic freedom.

The confinement of hadrons is well visible in the Lund string model [7]. Due to vacuum polarisation, the lines of the colour field between a pair quarks are contracted compared to the electric field. The field behaves like a string ended by a pair of quarks. Any addition of energy to the system (moving the quarks apart) is saved in similar way as by increasing tension of a string. If the energy needed for quark-antiquark pair production is reached, the string breaks into two, leaving an additional $q\bar{q}$ pair in the middle.

This description is possible due to charge anti-screening, which is responsible for squeezing the colour field lines into tubes. This of course contradict to the behaviour of the electromagnetic fields [8]. Anti-screening comes from the gluon loops, which are vital elements in the description of strong interactions. It is derived from the running coupling constant (Fig. 2.1).

The renormalisation group equation shows the dependence of the coupling constant on the energy scale.

$$\frac{1}{\alpha(\mu^2)} = \frac{1}{\alpha(q^2)} + \beta_0 \ln \frac{q^2}{\mu^2}, \tag{2.1}$$

where the coupling constant α for a given momentum transfer μ is expressed in

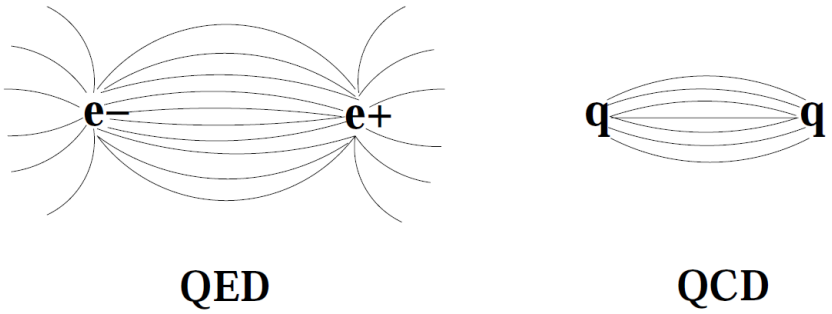

Figure 2.1. A comparison of the field lines between electromagnetic charge dipole (QED) and colour charge dipole (QCD).

the means of the known value of the coupling constant α for another momentum transfer q, and

$$\beta_0 = \frac{1}{12\pi}\left(4n_f - 11n_b\right) \tag{2.2}$$

depends on the number of particle generations, that can occur in the loop Feynman-diagrams, describing vacuum polarisation, n_f stands for the number of fermion types, and n_b for boson types [9].

Let us start with the behaviour of the coupling constant in electromagnetic interactions. In quantum electrodynamics (QED) there are no loop-diagrams containing photons $n_b = 0$, and there are 3 known generations of fermions, what implies $\beta_0 = 1/\pi$. This results in screening of the charge - the higher the momentum transfer, the higher the coupling constant.

For QCD the situation looks much different. From the properties of the SU(3) group one finds $m_b = 3$, and there are 3 generations of quarks $n_f = 3$. That results in $\beta_0 = -7/4$. Anti-screening is evident now, as the strength of the interaction increases with the distance between a probe charge and the field.

This leads not only to quark confinement within the hadrons, but also to asymptotic freedom - at small distances the quarks behave as quasi-free objects [10].

One of the most successful simplified descriptions of this effect is given by the MIT-bag model. This is a phenomenological model that assumes, all the constituent quarks move freely within the volume of hadron, just like they were put into a bag they can not leave. Their mass is very small and they are subject to weak forces only [11]. Size of the bag is dependent on the pressure exerted on the bag by vacuum, which is a constant universal for all the hadrons. It is called the bag-constant, usually assumed to be $B \approx$234 MeV/fm^{-3}. Estimation of B comes from e.g. proton radius.

Another consequence of the running coupling-constant is the division of the field of QCD into two domains. For high momentum transfers the coupling-constant is small

enough to apply perturbative expansion and get analytical results. This approach is called perturbative-QCD (pQCD). For low momentum transfers the coupling-constant starts to exceed unity, thus the pQCD does not apply to the colour charges at large distance. The problem can be bypassed by introducing discrete space-time by using a formulation of QCD on a lattice of points in space and time. This method is called lattice-QCD (lQCD).

While most of the problems are well described by QCD, there are some effects that have not been proved very well. Let us mention these peculiarities now. Although the theory still allows for existence of bound states made of 5 quarks (so-called pentaquarks) [12], it seems the smallest possible white-coloured state is realised by nature, as the experimental evidence of pentaquark states is not convincing. As the carriers of the strong force, gluons carry colour. Therefore, it is theoretically possible to observe a glue-ball - a system made of gluons only. There were a number of experiments conducted to find some of those composite particles, but any definitive evidence has not been found yet [13].

This history shows the importance of the experimental approach to physics. Even though the most important breakthroughs in physics are prepared in the field of theory, every idea needs to be attested or disproved by an experiment.

One of the problem awaiting thorough research is the existence and the properties of a new state of matter, called quark-gluon plasma.

2.2 What is the Quark-Gluon Plasma?

The quark-gluon plasma (QGP) is a system of quarks and gluons that are not confined within hadrons, but have an ability to propagate within the volume of the whole system. Also the chiral symmetry is restored, which enables to produce a higher amount of heavy quarks in gluon fusion compared to the hadron matter, that is not only confined, but also for which the chiral symmetry remains broken.

How is it possible in the spotlight of confinement previously discussed here? As the distance between two hadrons smaller than their diameter, they start to overlap. As a consequence, the colour potential inside one of them starts to be exposed on screening due to proximity of another hadron. The quarks start to interact with the quarks of another hadron, so that the confinement expands over the whole volume of both of them, as they flow into each other. The dynamical picture of this process shows that the 'white' substructures in such system are quite unstable and they do not last long enough to hadronise, as long as the energy density is high enough not to let them fall apart.

The name QGP comes from the analogy to plasma, as a state of macroscopic matter. The quarks inside of the QGP are not confined within hadrons they come with, in a way analogous to electrons in a plasma, which are deconfined from their

mother-atoms. Another similarity found in both plasma and the QGP is charge screening. The colour charge of the quarks is screened by the charge of another hadron. An analogous situation is observed in plasma, where a collective behaviour of charged particles is seen as the number of particles within the Debye sphere is higher than one [14].

The history of the QGP starts with the theoretical works on physics of neutron stars, which found out there is a limit on density of a stellar object, where even hyperons are to light to be main constituents. It was presumed, those dense objects are build of quarks as they knew them [15]. The same idea was reflected by Collins and Perry in 1975 [16].

The idea of quark-gluon plasma was conceived by Shuryak in 1978 [17, 18]. Analysing the properties of matter inside a neutron star, he noticed, that given the density of a neutron star the hadrons need to overlap, as the baryon number has to be constant. He suggested, as they overlap they build up a quark soup. Further development of those theories lead to modern concept of the QGP.

The QGP matter described in all the papers mentioned above is not possible to be brought to life in a laboratory. They concern one of the methods of the QGP creation, that is still not possible outside of astrophysical objects - the method of cold compression.

Another one method is available for experiment. The matter can be heat up (and compressed a bit, too) so much, that the newly created quarks are packed up densely enough for the number of quarks inside the Debye sphere to exceed one. This is done by colliding relativistic nuclei.

Deconfinement in this sense was proposed in 70's as pQCD solution for asymptotically high momentum transfers. In this description the QGP has a form of diluted gas of weakly interacting partons (wQCD). The description could be applied to the energies of order of GeV or TeV.

In the early 80's, Bjorken conjectured a scenario of the QGP formation in heavy-ion collisions, in particular he found the initial energy density and its evolution with time [19]. The most interesting prediction was an existence of a lower limit on energy in the centre of mass per nucleon $\sqrt{s_{NN}}$, found it to be 25A GeV. Also the baryochemical potential μ_B should be close to zero to reach the QGP.

These predictions concern the range where meson degrees of freedom are dominant and no phase transition in standard sense is foreseen. Instead of that, a smooth change from hadron gas to the QGP should be seen. This is so-called cross-over transition.

On the other hand, it is well established that hadrons produced in the collisions never reach temperatures higher that about 160 MeV (Hagedorn temperature) [20]. It was a clue, that the critical temperature to reach the QGP for low baryon densities should be a little higher than 160 MeV. This temperature is rather low, what points

further to a possible existence of the QGP also in the non-perturbative domain of QCD (npQCD). Mainly bag models or statistical models are used for the npQCD, as for high colour density the region where lattice-QCD can be applied is very narrow.

The QGP obtained in the collisions of heavy ions lasts for very short. Let us describe the conditions and changes in the state of matter when the transition to the QGP occurs (Fig. 2.2). The time-scale used further was calculated for beams of 160A GeV/c in fixed-target experiments ($\sqrt{s_{NN}}$=17.27 GeV).

The very first phase takes 1-2 fm/c. That is the time needed for the reacting nuclei to go through each other. The nucleons interact with the nucleons from the other nucleus. For a central Pb+Pb collision one nucleon interacts 4-5 times on average (geometric model).

Then the newly produced hadrons cause secondary interactions. This phases lasts for further 10-20 fm/c. If a big number of nucleons takes part at interactions (central collisions, big systems), higher and higher number of the reaction products scatter on each other, which process makes impossible for the reaction products to leave the interaction area easily. During this stage the density might reach a value big enough to induce the QGP.

As the QGP phase is reached the number of degrees of freedom increases rapidly and the bare quark mass is restored. The main characteristics of this stage is the formation time of 1 fm/c, temperature T over 230 MeV and energy density ε of 3 GeV/fm^3, which makes 20 times the value of usual nuclear matter.

The immediate effect of this stage is an expanding fireball of the QGP-matter which exists for about 5-7 fm/c. Then the hadrons start to form and there it comes the chemical freeze-out at the temperature of 150-175 MeV ($\varepsilon \leq$1 GeV/fm^3) - the matter does still interact elastically, but it is neither possible to exchange the quark content between hadrons, nor to create some new $q\bar{q}$ pairs in inelastic interactions. The chemical equilibrium for hadron gas is reached not until about 100 fm/c, what makes 10 times the value for the QGP.

The next step is the end of the elastic processes, which marks the kinetic freeze-out (T =110$\div$130 MeV, $\varepsilon \approx$0.05 GeV/fm^3).

For comparison the properties of non-excited nuclear mater are $T \approx$=0, and $\varepsilon \approx$0.15 GeV/fm^3.

2.3 Experimental Evidence of the QGP

It is worth noticing, that the most successful theories often predict some constituents that can not be easily observed, just like neutrinos produced in week decays and quarks, that never occur as free particles. But their application would not become so widespread, if they had not have greater predictive power, than the earlier theories. It is of great importance, that quite simple assumptions can lead to

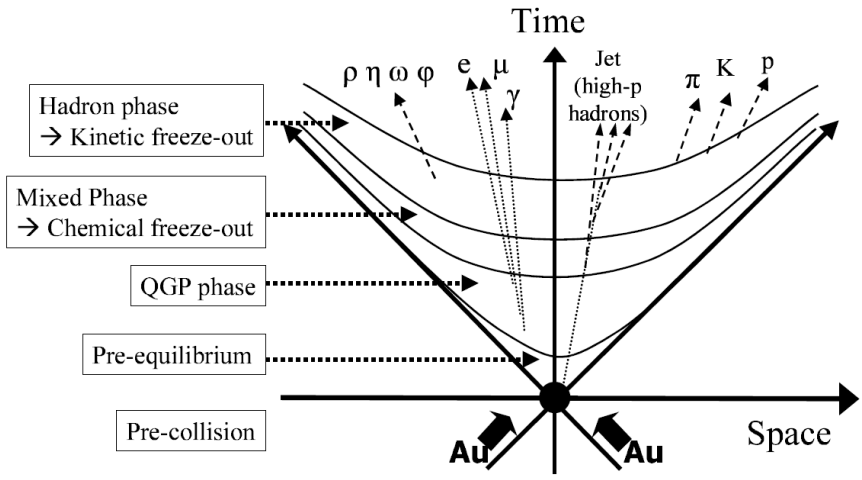

Figure 2.2. A schematic diagram of space-time evolution of a relativistic heavy-ion collision [21]. The particle types showed in the picture point at a phase of evolution when the respective type decouple from the system.

conclusions, which surpass everything one could have predicted ever since.

The situation with the QGP is quite similar. It can not be observed in a direct way, as the QGP in the accelerator experiments does exist just for a short moment, which does not make possible to send some probes from the outside. The QGP is also confined within the limits of a system as a whole, which does not enable us to see it in a direct way.

A number of signatures of the QGP have been predicted by the theory. Many of them are based on restoration of the chiral symmetry in the QGP, making the quark mass equal to its bare mass, what makes possible to produce many more heavy quarks, as in the case of matter in typical states. Let us mention some of them:

- Collective motion due to anomalous increase in pressure. This can be measured by means of the elliptic and directed flow by studying correlations [22].

- Photons and dileptons are decoupled from the system on early stage of the QGP development, as they do not interact strongly. Hence, they are good candidates for the messengers from inside of the QGP. For the QGP the production of direct protons is enhanced [23]. Restoration of the chiral symmetry causes a change in the mass of vector mesons [24, 25], which is responsible for a change in the shape of e^+e^- spectrum.

- For hard interactions, partons start to form jets on the stage of pre-equilibrium, just before creation of the QGP. Thus, the properties of the deconfined matter can be probed by a developing jet. The QGP is a dense medium, therefore

the energy of the partons is damped and the jet undergoes widening due to deflection from the initial direction of the strings. Some effects of dense medium are seen already at RHIC, but the jet quenching itself is seen at LHC [26].

- Charmonium suppression is caused by screening effects in the QGP [27].
- As the number of degrees of freedom for the QGP is higher than for hadron gas, creation of deconfined matter results in higher entropy. This translates to higher pion multiplicity [28].
- In the vicinity of critical point there is expected a rapid increase in fluctuations [29].
- Enhancement in the production of heavy quark-antiquark pairs increases the total number of particles bearing strangeness [30–32]. As the chiral symmetry is restored, and the mass of quarks rapidly decreases to their bare mass, the energy limit for the creation of $s\bar{s}$ is much lower than for hadron gas, although it is still $m_s/m_{u,d}$ =15÷35 times higher than for the light quarks. This factor still suppress creation of strangeness, but not as much as for hadron gas. As the baryon number is conserved, baryochemical potential μ_B for the light quarks is different to zero, what suppress $u\bar{u}$ and $d\bar{d}$ creation. As the projectile and target do not include strange quarks, μ_s equals zero. Hence, the strangeness production can be enhanced if u and d energy levels are occupied, and the Fermi energy exceeds $2m_s$ ≈300 MeV. The effect occurs only if the system reaches equilibrium. For the QGP it takes just 10 fm/c, while for hadron gas it is higher by an order of magnitude. Thus, it is quite improbable to see strangeness enhancement in hadron gas.

Strangeness enhancement has been observed by NA35 for S+S interactions [33], but the question if it is possible to reach the state of the QGP for such low system size is still under investigation.

This research program on sulphur and oxygen collisions at $\sqrt{s_{NN}}$ ≈20 GeV at CERN was extended by lead at $\sqrt{s_{NN}}$ ≈17 GeV. A number of experiments, which had taken a part at the program, found an unusual behaviour in the early stage of collisions, assigned to creation of the QGP. Although there were many models describing the data, the signatures they used were not all unique to the QGP creation.

For the first experimental evidence of the QGP one had to wait until late 90. The discovery of the QGP was by no means a work of a single experiment: many collaborations involved in lead beam program at CERN observed some effects, which might be easily attributed to the creation of the QGP [34].

What raised doubts, was that the signatures of the QGP can be explained using some effects different to the creation of the QGP. But no other theory has ever existed, which could explain all the observed peculiarities at once.

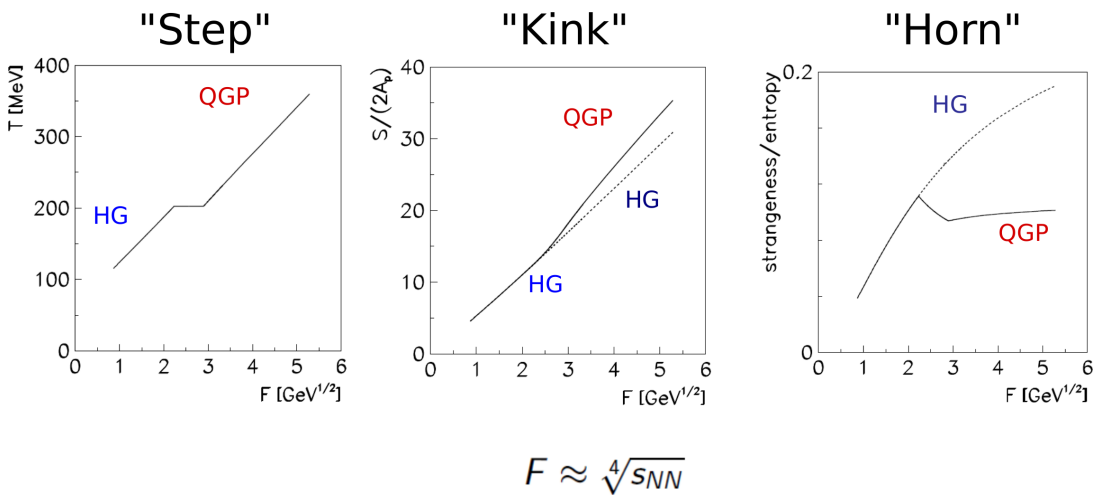

Figure 2.3. The predictions concerning the properties of the onset of deconfinement, as predicted by the Statistical Model of the Early Stage (SMES) [35]. The solid line shows the prediction in the case when the phase transition exists, while the dotted line corresponds to the hadron gas. The observables are plotted against the Fermi variable $F = \frac{(\sqrt{s}-2m_p)^{3/4}}{\sqrt{s}^{1/4}}$ [36], a measure of energy widely used in Landau hydrodynamics. S stands for entropy, directly linked to the pion mean multiplicity $\langle\pi\rangle$, $2A_p$ is the number of baryons which take part in the collision, and the measure of strangeness are mean multiplicities of the particles containing strange quark. The greatest breakthrough of the model was the prediction of the horn structure, which the other theories were failing to reproduce.

That was the next step in the research on the QGP, where the experimental programs at CERN were confirmed by the experiments at AGS, and BNL (max. $\sqrt{s_{NN}}$=5.5 GeV). The results made sure another state of matter is created but the theories failed to reproduce all the observed facts. An unprecedentedly successful model created as a direct consequence of those experiments was the Statistical Model of the Early Stage (SMES) [35], which predicted characteristic structures near to $\sqrt{s_{NN}}$ ≈10 GeV (Fig. 2.3), a point corresponding to a minimum of system volume. The most important prediction was a sharp maximum in the production rate of strange hadrons relative to pions, which no other model was able to reproduce. The SMES assumes an equation of state (EoS) with first-order phase transition, and predicts a second order critical point between the cross-over and first order transition.

Then the CERN program at the SPS was extended by central collisions of Pb+Pb, where the NA49 experiment performed an energy scan, sometimes accompanied by some other CERN experiments. The results showed, that the most rapid changes in properties of hadron production are observed for $\sqrt{s_{NN}}$ between 7 and 12 GeV, and gave a clear signal, that the deconfinement starts already in the SPS energy range.

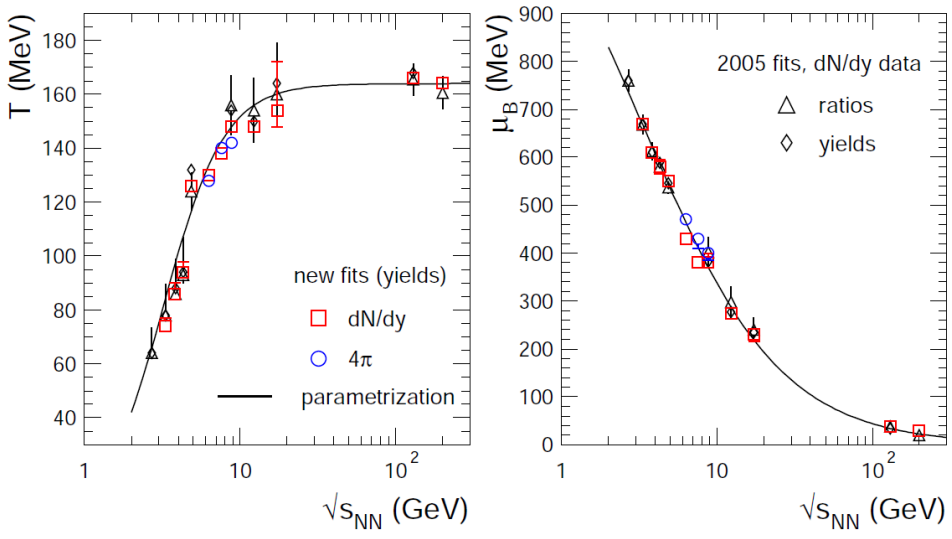

Figure 2.4. The dependence of the temperature and baryochemical potentials on centre-of-mass energy are obtained from Statistical Model providing the experimental values for hadro-chemical abundances as an input [38].

2.4 Phase Diagram of Strongly Interacting Matter

The phase diagram for strongly interacting matter is built in strict analogy to the phase diagram for molecular substances. Thermodynamical properties of a non-relativistic system can be described in dependence on temperature T, particle number density n and pressure p. The relation between those state variables is given by the equation of state. As for the relativistic physics the number of particles is not conserved, the baryon number density n_B or baryochemical potential μ_B start to play a role of particle number density in non-relativistic physics [37].

The only parameters of interest one can set in accelerator experiments are the centre-of-mass energy $\sqrt{s_{NN}}$, and the system size (using different ions). How to get T and μ_B, which are the state variables needed to study the phase diagram then? Some work is still needed to obtain the result. The usual procedure to get the dependence of T and μ_B on energy is based upon the calculations of the hadron abundances using resonance gas models. It is assumed, the observed particle yields are generated at a common surface at which all particles decouple. Values of μ_B and T on this surface are extracted. Fitting those parameters together with the volume parameter gives values for the particle abundances in close agreement with the experiment (Fig. 2.4) [38, 39]. Independently on the procedure applied, finding the equation of state is always an interplay between theory and experiment.

Except of the aforementioned SMES model (Sec. 2.3, Fig 2.3), there is a number of recent theoretical developments, which predict so diverse and contradicting effects, that our lack of knowledge concerning field of the deconfinement becomes clear. A

systematic research program concerning the phase diagram is therefore inevitable. Lattice QCD calculations can be performed for non-zero temperatures and vanishing or small mu_B [40]. For $\mu_B = 0$ there is no true phase transition between hadron gas and the QGP, just a rapid increase of the energy density at critical temperature T_c at about 160÷190 MeV. Increasing μ_B the T_c drops just a little. Between two aforementioned phases there is a 'semi'-QGP, as the transition is not discontinuous.

A quite interesting theory is that of quarkyonic matter [38]. It predicts an intermediate region between hadron gas and the QGP for which the number of degrees of freedom is much higher compared to hadron gas, but still does not reach the value for the QGP. Quarkyonic matter is approximately confined, but has a large baryon number and energy density. The restoration of chiral symmetry is not crucial for the existence of this theoretical state of matter. If chiral symmetry is not restored, number of degrees of freedom is half of that for the QGP. The model gives qualitative and semi-quantitative explanation of the features observed in relativistic nuclear collisions, like non-monotonic behaviour of strange particle multiplicity ratios at $\sqrt{S_{NN}} \approx 10$ GeV, like the SMES.

The starting point is the remark, that the temperature dependence on centre-of-mass energy increases fast linearly up to $\sqrt{s_{NN}}$ ≈10 GeV, where the temperature saturates reaching asymptotically a value of about 160 MeV, while μ_B decreases in a smooth manner. Combining μ_B and T, one finds two domains: one of constant temperature of about 160 MeV for μ_B <400 MeV, and another for higher μ_B, where the temperature drops linearly.

The division of the freeze-out parameters into two regimes is argued to be due to existence of another one phase, called quarkyonic matter, and the existence of a triple point in between - in the region, where the structures predicted by the SMES occur. The unusual non-linear dependence of some observables on energy, found by the SMES to be signatures of the onset of deconfinement (Fig. 2.3), are predicted to be caused just due to vicinity of the triple point. The theory does not make any predictions concerning the critical point. It is possible, that it exists for lower μ_B, than for the triple point. In the case the critical point also exists, the triple point would hold together three different phases connected by the first order transitions.

The calculations have been made for infinite number of colours, which allows to expect an approximate triple point for large number of colours [38]

Another theory uses a hybrid MIT-bag model to predict the properties of phase coexistence. The model is based on a two-EoS model with the Gibbs equations to link the two phases, which method was successfully used for the predictions on the phase transition inside of neutron stars. For the quark matter the MIT-bag model is used. They found, that for high T and low μ_B the T_c does not depend on the EoS for hadron gas and the isospin effects are negligible, while for high μ_B the T_c is very sensitive to the EoS. The authors applied δ-meson field, which is relevant for high

densities. Relevant isospin effects as seen in the asymmetric matter are very sensitive to different symmetry terms in the hadron EoS. This is quite important to point the way for the research of asymmetric high density systems [41].

Another interesting possibility is the existence of an intermediate state of matter, called glasma [42], which is a colour glass condensate [43], in analogy to amorphous macroscopic matter.

Some lattice calculations with 2+1 and 3 flavours staggered fermions suggest, there might be no critical point at finite chemical potential. This was found in studies of the curvature of the critical surface [44, 45] who used 2+1 and 3 flavors staggered fermions and a Taylor expansion in q/T to study the curvature of the critical surface at very light quark masses close to quark chemical potential $\mu_q = 0$ surface. They found the critical surface to be bent so that if the quarks are given non-zero mass, the first order transition region shrinks. The conclusion is that there is no critical point at finite chemical potential. However, it is possible that the critical surface bends back at larger μ_q what might induce a reappearance of the critical point.

There is also a theory predicting a second critical point at low μ_B [46], and a theory that predicts, that the lower μ_B the higher the order of phase transition between hadron matter and the QGP. The latter conclusion is found from the statistical model of quark-gluon bags [47].

The results of experiments was a breeding ground for the forthcoming theories and experiments. Quarkyonic matter, mixed-state, two critical-points, no critical point at all - as long as an exhausting description of the region near to the critical point is missing, the imagination of the theoretical physicists knows no limits. Therefore the NA61/SHINE experiment has proposed a wide phase-space scan program to check the real properties of onset of deconfinement as well as the position of the critical point of strongly interacting matter.

2.5 NA61/SHINE Phase-Space Scan

The unknown position of the critical point was the most important factor, that lead to a consequent research program of system-size and energy scan in the NA61/SHINE proposal. The more data points, that is, the more energies and reactions analysed, the better our understanding of the phase-space of strongly interacting matter. The program was widely supported by the community of theoretical physicists. For example, in the letter of Rajagopal, Shuryak, Stephanov and Wilczek addressed to the SPS Community one reads: *... Recent theoretical developments suggest that a key qualitative feature, namely a critical point (of strongly interacting matter) which in a sense defines the landscape to be mapped, may be within reach of discovery and analysis by the SPS, if data is taken at several different energies. The discovery of the critical point would in a stroke transform the map of the QCD phase diagram*

which we sketch below from one based only on reasonable inference from universality, lattice gauge theory and models into one with a solid experimental basis [48].

As the hadron content is established on the stage of chemical freeze-out, thus the experiments for the research aimed at obtaining the T and μ_B for the critical point have to be conducted at a little higher energies than those to study the properties of the onset of deconfinement.

The onset of deconfinement refers to the beginning of the creation of a deconfined state of strongly interacting matter at the early stage of nucleus-nucleus collisions when increasing the collision energy. The signals of the onset of deconfinement are not sensitive to the structure of the transition region, they are just based on the difference in properties between confined and deconfined matter. The studies of the onset of deconfinement result in better understanding of the structure of the transition region between two phases, and confirm the existence of the QGP. The signatures of the critical point are only observable if the freeze-out is reached for T and μ_T in the vicinity of the critical point [37].

The energy density at the early stage of the collision, which is required for the onset of deconfinement is higher than the energy density at freeze-out, that is relevant for the search for the critical point [48]. Thus in order to reach the energy density characteristic to the phase transition exactly on the stage of chemical freeze-out, one has to reach even higher energy densities before (Fig. 2.5).

In addition to the results for different heavy-ion interactions, where an emergence of the QGP is expected, there is a need for $p+p$ and $p+A$ reference data of good quality, in order to compare the results for heavy systems with the data for the smallest hadron-hadron system, for which the creation of the QGP is unexpected. Even thought there is a rich set of heavy-ion results from a number of experiments, the correct interpretation of the data relies on a comparison to p+p and p+A interactions. The data for fluctuations, correlations and particle production for higher p_T in the SPS energy range are sparse. In particular the data from many experiments are not measured for the same energies in the p+p or p+A interactions, as for the A+A collisions. The statistical errors are quite big for numerous data sets and the data are scattered so much, that it makes hard or almost impossible to conduct any reasoning concerning the comparison with some model predictions or to find some new facts having such data as a reference, not to mention pinning down the critical point and studies on onset of deconfinement.

In the light of these facts, it is not enough to use a system and energy, where the onset of deconfinement is reached, but one needs to perform research on a set of systems of smaller size, to reach the critical point on the stage of freeze-out. In addition to that, reference data for $p+p$ have to be taken. Thus, the final research program makes use of following systems: p+p, Be+Be, Ar+Sc, Xe+La, as well as Pb+Pb for beam momenta for protons (heavy ions) of 13, 20, 31, 40, 80 (75), 158

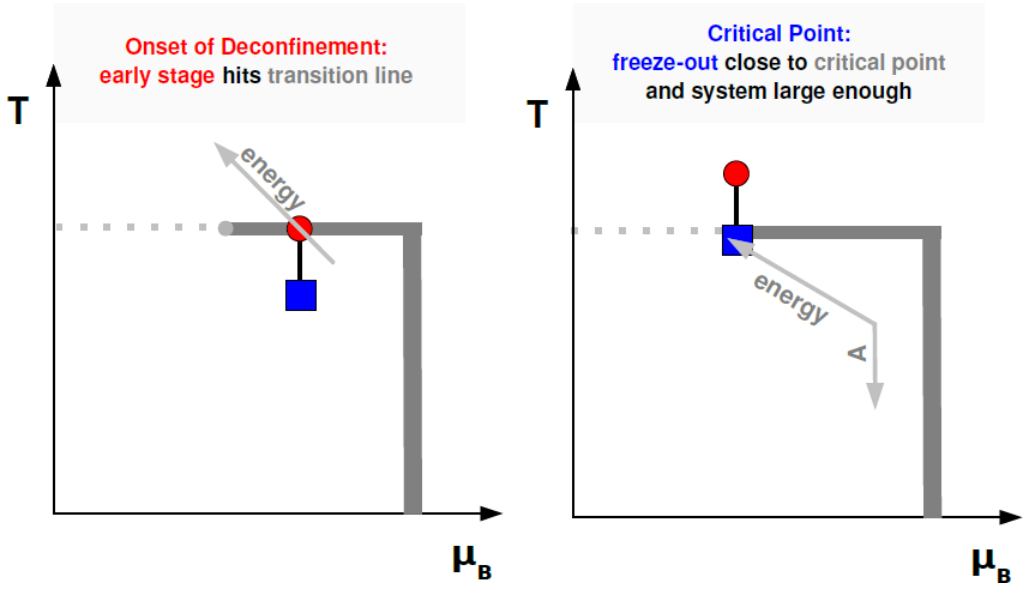

Figure 2.5. The difference between the studies of the onset of deconfinement (left) and the critical point (right). In the first case the early stage of the system development has to reach the phase transition (circle), while the chemical freeze-out in the region of hadron gas (square). For the latter, the critical point has to be reached at the point of the freeze-out, and the early stage of the development is situated within the region of the QGP. The position of the early stage is only approximate as the system is not in equilibrium before freeze-out [37].

(150) GeV/c. The program is already running, and the data for the first three systems are taken and being analysed (Fig. 2.6).

The research program aims at measuring not only some of the traditionally used signatures of the QGP, like strangeness enhancement, but it is mainly concentrated on the behaviour predicted by SMES (Fig. 2.3) [35] to study the properties of the onset of deconfinement. For the research on the position of a possible critical point the experiment utilises fluctuation observables, as there is predicted, that a maximum of event-by-event fluctuations should be reached in the vicinity of the critical point [29], so-called the hill of fluctuations (Fig. 2.7).

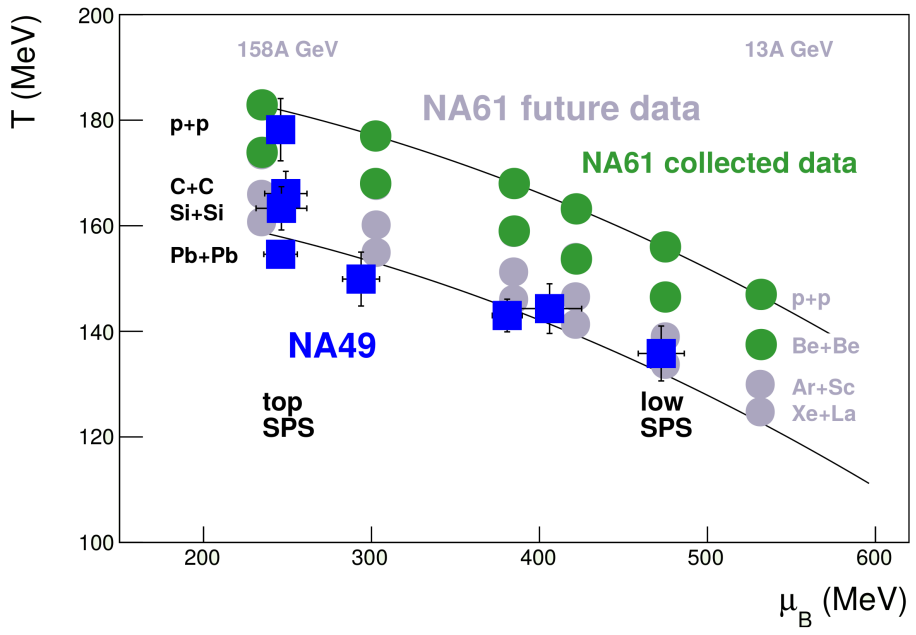

Figure 2.6. The reactions and beam momenta used for the phase diagram scan by NA61/SHINE.

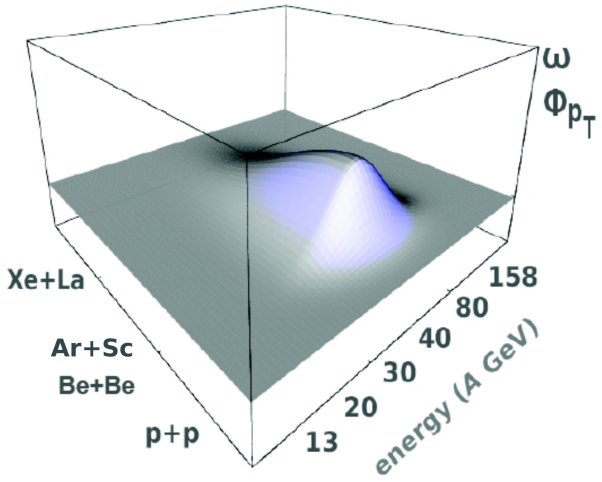

Figure 2.7. The expected picture of the hill of fluctuations with the maximum at the critical point.

Chapter 3

Identification of Λ-Hyperons

The work presented in this dissertation concerns the development of the method of analysis aiming at obtaining the Λ-hyperon multiplicities in p+p interactions for the further use as a reference for the studies on production of strangeness in heavy-ion interactions.

Therefore, this chapter is entitled to Λ-particle and the identification methods used in Λ analysis.

3.1 History of Strangeness

Λ-hyperon was discovered as a constituent of cosmic-ray background in 1951, just 5 years after the very first evidence for existence of K^0-meson was found. Both particles are easily recognised by their specific decay topology. As electrically neutral particles they stay invisible until they decay. The main decay channel of Λ and K^0 produce a pair of oppositely charged particles. Hence, a characteristic V- or Λ-shaped structure is left over as energy deposition in a detector (Fig. 3.1). This kind of decay is referred to as V^0, where V stands for the decay topology, and the superscript 0 for charge of the parent particle.

Then, there it came a time for accelerator experiments. An interesting feature was found at the Cosmotron in BNL. The large MIT multiplate cloud chamber was used to measure the lifetime of Λ [51]. There was found, that the lifetime of Λ and K^0 exceeds all the previously discovered particles but neutron. While e.g. Δ-hyperon decays fast immediately after it is produced (10^{-24} s), mean lifetime of Λ-hyperon is by about 14 orders of magnitude longer. In addition to that, it was found that particles of this strange kind are produced always pairwise.

The explanation of this effect came from Pais and Nishijima [52]. They found, that while the strong force accounts for the production of strange particles, the weak force underlies their decay.

Also the associated production of these weakly decaying particles was explained

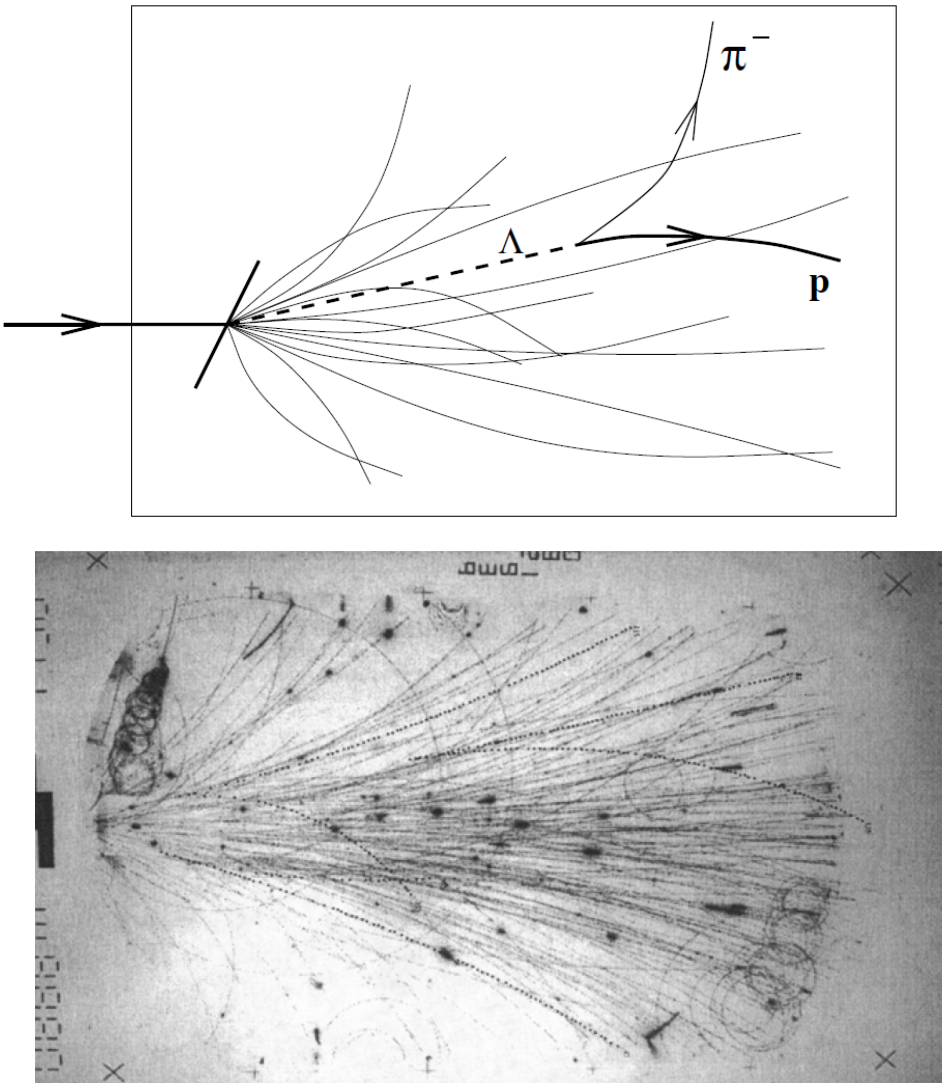

Figure 3.1. *TOP:* A scheme [49] of the most probable decay channel of Λ. A track of Λ-particle, invisible to the detectors, is shown as a dashed line. The decay products form a characteristic V-like shaped structure, which is the main reason for calling this kind of decay-vertex V^0. *BOTTOM:* Experimental picture as seen by NA35 streamer chamber with V^0 decays marked as dotted lines [33].

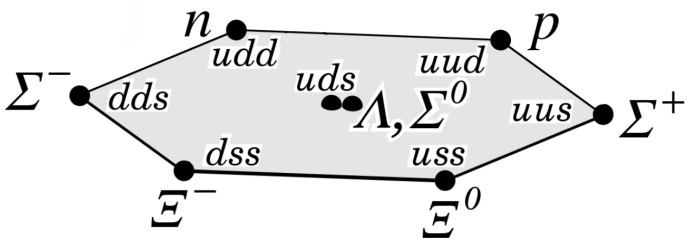

Figure 3.2. SU(3) spin $\frac{1}{2}$-octet containing Λ [50].

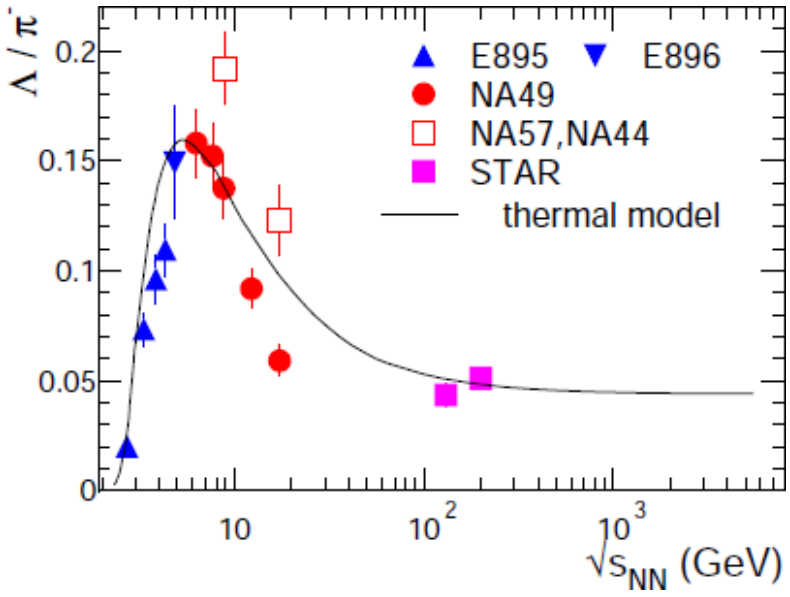

Figure 3.3. A peak in Λ to π^- ratio [38].

by Nishijima and Nakano [53, 54]. They introduced an additional quantum number, called strangeness (S). For Λ, K^-, and $\overline{K^0}$ strangeness S=-1, while for their antiparticles S=1. They assumed, strangeness is conserved in strong interactions, whereas the processes involving weak force change the strangeness content by one.

A better complementary explanation to the associated production of strangeness was proposed within the quark model (Fig. 3.2). It introduces a strange quark (s), with strangeness content of -1 and its antiparticle ($\bar{s}$ with S=1) as the only carrier of strangeness. As the strong interactions enforce the conservation of strangeness, it is produced as a particle-antiparticle pair. Except of $s\bar{s}$-quarkonium production, that has relative small cross-section, the quarks are included into two different hadrons, one of which comprises s-quark, and the other $\bar{s}$.

Then, the regular research programs systematised our knowledge of the properties of strange particles.

The renaissance of the strangeness exploration came with the theories of the QGP (Chapter 2), where a significant change in production of strangeness is predicted, and observed. Λ-hyperons might be used as one of the particles carrying strangeness, which should be used to estimate total strangeness, e.g. to obtain Wróblewski factor [55], or as an individual signature (Fig. 3.3).

3.2 Properties of Λ-Hyperon

Λ baryon is a particle build of *uds* quarks. The strangeness content is S=-1, and its isospin I=0. The ground state of Λ is of positive parity and spin J=$\frac{1}{2}$ ($I(J^P) =$

Decay mode	Branching ratio (Γ_i/Γ)	p(MeV/c)
$p\pi^-$	(63.9 $\pm$ 0.5)%	101
$n\pi^0$	(35.8 $\pm$ 0.5)%	104
$n\gamma$	(1.75 $\pm$ 0.15)$\times 10^{-3}$	162
$p\pi^-\gamma$	(8.4 $\pm$ 1.4)$\times 10^{-4}$	101
$pe^-\bar{\nu}_e$	(8.32 $\pm$ 0.14)$\times 10^{-4}$	163
$p\mu^-\bar{\nu}_\mu$	(1.57 $\pm$ 0.35)$\times 10^{-4}$	131

Table 3.1. Λ decay modes [50].

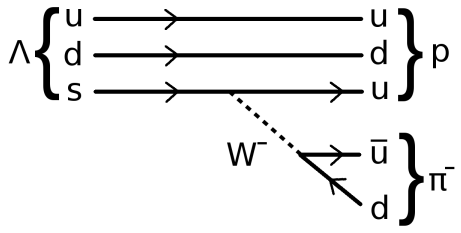

Figure 3.4. A Feynman-diagram depicting the most probable Λ-decay.

$0\left(\frac{1}{2}^+\right)$. Mass of the particle is $m_\Lambda = 1.115683(6)$ GeV/c^2. The mass difference between Λ and its antiparticle is consistent with zero. Mean lifetime $\tau = (2.632 \pm 0.020) \times 10^{-10}$ s, what results in mean proper length of $c\tau = 7.89$ cm [50]. Decay modes are presented in Tab. 3.1.

The dominant decay is of V^0 type - over half of the Λ decays lead to final-state proton and π^-. This channel is a weak decay channel, where s-quark decays to u, $\bar{u}$, and d via W^- boson (Fig. 3.4).

Most common production channels for nucleon-nucleon interactions which result in Λ and Σ production, and their energy thresholds are the following [56]:

$$
\begin{aligned}
N + N &\rightarrow N + \Lambda + K \quad (\sqrt{s_{NN}} > 2.55\,GeV)\\
N + N &\rightarrow N + \Sigma + K \quad (\sqrt{s_{NN}} > 2.63\,GeV)\\
N + N &\rightarrow \Lambda + K + \Delta \quad (\sqrt{s_{NN}} > 2.88\,GeV)\\
N + N &\rightarrow N + N + \Lambda + \bar{\Lambda} \quad (\sqrt{s_{NN}} > 4.11\,GeV)
\end{aligned}
$$

3.3 Identification

In order to observe neutral strange particles, one has to find characteristic V^0 pattern among myriads of particle tracks. This is usually done by combining each positively-charged track with all negatively-charged tracks. If the tracks approach to each other at some point, they probably are daughter tracks emerging from one decay vertex. If one of them is negative and the other positive, and the total momentum

of their combination points to the main interaction vertex, they are very likely to be either pions produced in K^0_S decay, or $p\pi^-$ resulting from Λ decay. In addition to that, lifetime of the analysed particles should be consistent with the value for Λ [49].

It is not easy to ascertain if the unseen mother particle was one or the other. Decays of Σ^0 are even more problematic, for it is virtually impossible to distinguish this particle from Λ. It decays electromagnetically to Λ and γ immediately after it is created. Hence, it is a widespread convention in experimental particle physics to treat Λ and Σ^0 as indistinguishable particles and to include the yield of Σ^0 and its excited states into the yield of Λ, without correcting it using some models [49]. This method was applied in this dissertation.

All the methods described below are used in the analysis presented in this dissertation. Lifetime and the Armenteros-Podolanski plot are used to ensure the analysed particle is Λ, dE/dx method is used to reduce background due to K^0_S and some other decays, and background subtraction is used in order to extract the signal from Λ-decays from the background that could not be reduced because of cross-over regions in the dE/dx and Armenteros-Podolanski analyses.

3.3.1 Armenteros-Podolanski Plot

The most common method of strange particles identification makes use of the asymmetry in angular distribution of the decay products. Due to momentum conservation, both particles created in a V^0 decay are described by transverse momenta ($\boldsymbol{p_T^+}$ for positive-charged particle, $\boldsymbol{p_T^-}$ for negative), which are the same in magnitude ($\sqrt{\left(\boldsymbol{p_T^-}\right)^2} = \sqrt{\left(\boldsymbol{p_T^+}\right)^2}$), but of opposite direction, if measured with reference to the momentum of the mother-particle.

Longitudinal momenta of these are different ($p_L^+ \neq p_L^-$), as the angular distribution in the centre-of-mass system is totally random. The relative p_L asymmetry of the decay products is given by Armenteros-α [57]:

$$\alpha^{Arm} = \frac{p_L^+ - p_L^-}{p_L^+ + p_L^-}. \tag{3.1}$$

If the system is symmetric, α^{Arm} can take any value in the range $-1 < \alpha^{Arm} < 1$, as in the case of K^0_S, which decay mainly to π^+ and π^-, both of the same mass. For asymmetric systems, the higher the mass difference between the decay products, the more populated is the region near to $\alpha = +1$ if the positive particle is more massive like for the products of Λ-decay, and $\alpha = -1$ for the other case. But this is still not enough to separate different types of strange particles. To find the difference in phase-space distribution for the oppositely-charged pair of particles, one needs to add another dimension to the plot and combine α^{Arm} with

$$p_T^{Arm} = p_L^+ = p_L^- = \sqrt{(\boldsymbol{p^+})^2 - (p_L^+)^2}, \tag{3.2}$$

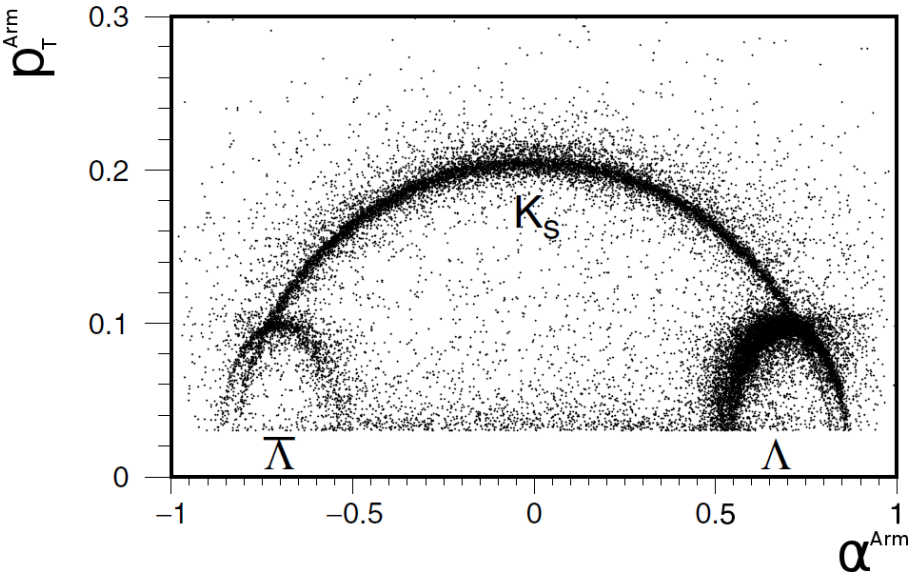

Figure 3.5. Armenteros-Podolanski plot is mainly used in analysis of strange decays to separate contributions from different particle types [49]-modified. A region with K_S^0/Λ ambiguity is very narrow.

where $\boldsymbol{p}^+$ is total momentum of the positive daughter track. Now the separation is quite straightforward (Fig. 3.5).

3.3.2 Specific Energy Loss (dE/dx)

A widely used method of particle identification is based on specific energy loss in the active volume of a detector. Energy loss depends not only on material which interact with a particle transversing it, but also on charge and velocity of that particle. Ionisation is responsible for major part of the losses. Energy loss due to ionisation is described well by Bethe formula:

$$-\frac{dE}{dx} = \kappa \frac{z^2}{\beta^2}\frac{Z}{A}\left[\frac{1}{2}\ln\frac{2m_e c^2\gamma^2\beta^2 E_{kin}^{max}}{I^2} - \beta^2 - \frac{\delta(\beta)}{2}\right], \tag{3.3}$$

where $\kappa = 4\pi N_A r_e^2 m_e c^2$, N_A is the Avogadro constant, r_e is the classical electron radius, m_e the electron rest mass, I stands for the mean excitation energy of the target material (for elements heavier than sulphur it can be approximated with $I \approx 10$ eV$\cdot Z$), γ and β are the Lorentz variables, δ is the density correction, Z stands for the atomic number, and A for the mass number of the element the interacting material is made of [58].

This formula applies to particles massive enough to neglect recoil effects (about 1 GeV/c). This does not apply to electrons also for other reasons: electrons are identical and indistinguishable with the shell-electrons of the material they interact with, and the bremsstrahlung is not negligible for electrons.

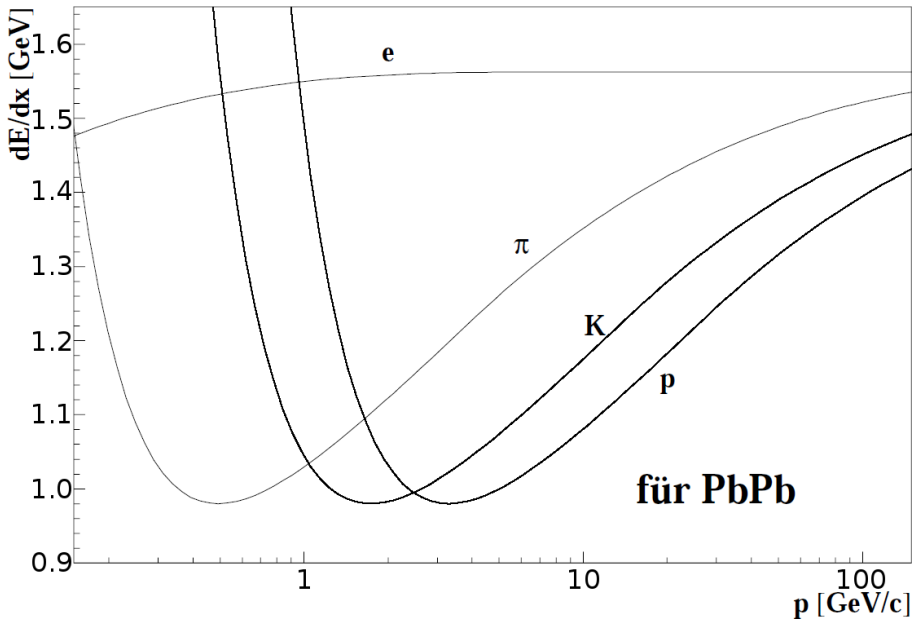

Figure 3.6. Parametrisation of the Bethe formula for different kinds of particles as function of momentum [56]. For electrons this approximation is not reliable (see: text).

The behaviour of such a function in dependence on β reveals a region where the energy loss decreases with increasing energy. Then, for higher energies there is a clear minimum. The particles with energies about the value for which the minimum is reached are called the minimum-ionising particles (MIPs). Increasing the energy, one finds the Fermi plateaux, for which the ionisation is about 160% of that for a MIP.

This method is specific to many kinds of particles, and allows to identify its type. In fact, there are some cross-over regions, where particles of different kind show the same energy loss and it is not possible to identify them without ambiguity (Fig. 3.6). But even these region could be used to reduce background significantly by setting a cut wide enough not to lose much signal from the particle important for the actual analysis.

This method could be combined with some other methods of identification to suppress the background even more.

3.3.3 Background Subtraction

Probably the best method to disentangle the K^0_S/Λ ambiguity is to extract the signal from the currently analysed particle using invariant mass spectrum created under assumption the most prominent decay mode of that particle was realised.

Invariant mass is defined in a standard way:

$$m = \sqrt{E^2 - \boldsymbol{p}^2}. \tag{3.4}$$

As the energy and momentum are conserved, mass of a parent V^0 particle can be calculated using momentum and mass of its decay products:

$$E_{parent} = E_1 + E_2 \tag{3.5}$$

$$\boldsymbol{p}_{parent} = \boldsymbol{p}_1 + \boldsymbol{p}_2, \tag{3.6}$$

what makes eq. (3.4) equivalent to

$$m_{parent} = \sqrt{m_1^2 + m_2^2 + 2(E_1E_2 - \boldsymbol{p}_1\boldsymbol{p}_2)}, \tag{3.7}$$

where indices 1, and 2 denote daughter particles.

Let us take Λ analysis as an example. As some kinematic configurations of K^0_S decay resemble that of Λ decay, signal from K^0_S can be seen in the same region of $m_{p\pi^-}$ - invariant mass, calculated from the Eq. (3.7) under assumption the decay products are proton and π^-:

$$m_{p\pi^-} = \sqrt{m_p^2 + m_{\pi^-}^2 + 2\,(E_pE_{\pi^-} - \boldsymbol{p_p}\cdot\boldsymbol{p_{\pi^-}})}, \tag{3.8}$$

where E_p /E_{π^-} stands for total energy of positively/negatively charged track calculated under assumption it is a proton/π^-. The PDG-value for proton mass is m_p =0.938272046(21) GeV/c^2 and for charged pion mass $m_{\pi^\pm}$ =0.13957018(35) GeV/c^2 [50]. Using this method one finds a clear signal from Λ, positioned at its rest mass, on top of combinatorial background. The background comes mainly from the other particle decays, most of them due to K^0_S-decays. The rest of the background result from some other two-particle decays, or some three-body decays where one track is out of the acceptance of the detector. Random combinations (false V^0) might also contribute there.

The background is characterised by smooth behaviour and it should not contain any peaks in the region of Λ mass, regardless of a phase-space region analysed. The analysis can be performed for the total acceptance of the detector system, or for arbitrarily chosen kinematic bins.

Then, both background and peak are fitted, which make it possible to extract an uncorrected yield of Λ.

As the background due to K^0_S decays does not exhibit peaks near to Λ mass, the K^0_S/Λ ambiguity can be reliably removed by subtracting background from the total mass spectrum.

In order to get rid of $\bar{\Lambda}/\Lambda$ ambiguity it is enough to apply a cut on invariant mass, since the systems are very asymmetric, and using proton mass for π^+ track, and π^- mass for $\bar{p}$ track results in invariant mass in a totally different range.

Chapter 4

Experimental Setup

This dissertation was prepared using the NA61/SHINE detector system. NA61/SHINE is a multi-purpose facility to study hadron production in hadron-proton, hadron-nucleus, and nucleus-nucleus collisions. It is placed at the CERN Super Proton Synchrotron (SPS) in the North Area. It is based upon a large acceptance hadron spectrometer, enabling to measure charged particle momentum with an outstanding resolution by an array of 6 Time Projection Chambers (TPCs), even in the case of high flux. In addition to this, the TPCs are used for particle identification by the means of specific energy loss (dE/dx). The charge deposited in the TPCs might be combined with the mass-squared measured by 3 time-of-flight walls. This results in excellent identification properties of the detector. A schematic layout of the NA61/SHINE experiment is shown in Fig. 4.1.

The trigger makes use of the signal from a number of scintillator beam detectors, some of which are used as veto (with a hole in the middle) in order to get rid of the events resulting from the interactions with the beam halo.

Additionally to the trigger detectors, 3 Beam Position Detectors (BPDs) are placed upstream of the target. They are proportional chambers with outer cathode planes divided into strips. They are used mainly to reconstruct the position of the main interaction vertex.

In order to measure the centrality of events in heavy-ion interactions, a high resolution modular zero-degree calorimeter is used. Accordingly to its function, it is named Projectile Spectator Detector (PSD). The tof-wall and the PSD were not used in the analyses presented in this thesis and they will not be discussed in this dissertation.

The settings of the detectors as well as the system monitoring are managed by a slow-control Detector Control System (DCS) written in EPICS.

In the following sections of this chapter a short description of each system of the experiment is provided. For details see thorough descriptions in Ref. [59], upon which this chapter is based.

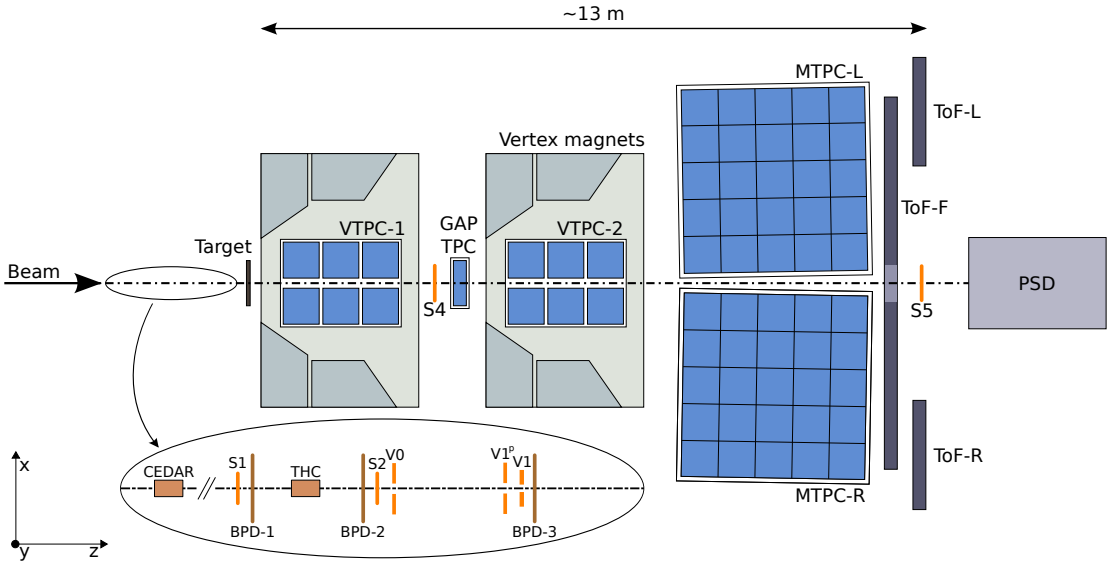

Figure 4.1. Layout of the NA61/SHINE detector system [59].

4.1 Beam

In this section we concentrate on secondary proton beams, describing the accelerator chain and the beamlines from the source till the NA61/SHINE target. Although the NA61/SHINE beamline allows the experiment to be operated with primary and secondary heavy ion beams, they were not used in preparation of this thesis.

4.1.1 Accelerator Chain

A duo-plasmatron ion source is used to ionise hydrogen gas and form the proton beam. The maximal current of protons generated using the source equals to 300 mA. As a preparation for injection into LINAC2, the Radio-Frequency Quadrupole RFQ2 is used to focus, bunch, and accelerate the beam to 750 keV. LINAC2 is an Alvarez drift tube linear accelerator, consisting of 3 tanks, which total length equals to 33.3 m. The beam energy at the output of each tank is 10.3, 30.5, and 50 MeV, respectively. The maximal current at the output of LINAC2 is 170 mA within 90% transverse emittance of 15π mm mrad, if operated with a repetition rate of 0.8 Hz and a pulse length of 120 μs.

The beam is accumulated then in the 4 rings of the PS Booster (PSB). The accumulation continues for up to 13 turns, which gives over 10^{13} protons per ring. Then, the beam is accelerated to 1.4 GeV, extracted and recombined in the extraction line just to be transported to the Proton Synchrotron (PS). At this stage, the beam consists of a train of 8 bunches (2 per ring), a typical structure in the case of a standard proton cycle for the fixed-target experiments. They are injected as 8 consecutive

buckets of the RF of the PS, operating at harmonic eight.

The PS is the oldest CERN accelerator in operation. Its circumference equals to 628 m. The synchrotron allows for acceleration of proton beams to 14 GeV/c for injection into the Super Proton Synchrotron (SPS). At the time of acceleration, an intermediate flat top is reached, where the bunches are split into two using the RF and the operation is switched to harmonic sixteen. As the top momentum is reached, the beam is de-bunched and re-captured at harmonic 420. This is needed to match the RF structure of the following acceleration stage, the Super Proton Synchrotron (SPS).

The extraction from the PS makes use of the unique method of the 'continuous transfer' multi-turn extraction. A staircase-shaped kicker pulse is used to extract the beam over 5 turns. Due to 6.8 km circumference of the SPS (11 times that of the PS), 2 cycles (5 turns each) of the PS are needed in order to fill it. Two half-turn gaps remain. They are used for the rising and falling edge of the SPS injection kicker.

The SPS is used to accelerate the 14 GeV/c beam to 400 GeV/c. Fixed harmonic 4620 is used (200 MHz). As the top momentum is reached, the beam is de-bunched and a slow extraction using third-integer resonance follows. The spill length for the fixed-target experiments can be set between 4.5 s and 10 s and is optimised for the users.

A scheme of the accelerator complex at CERN, containing the accelerator chain described above, is presented in Fig. 4.2.

4.1.2 Production of the Secondary Beam

The beam of 400 GeV/c protons extracted from the SPS reaches the TCC2 target cavern in the North Area, after being transported over 1 km with the use of bending and focusing magnets. Before reaching the cavern, the beam is split into 3, each part of which is directed towards a primary target. One of the targets is the T2 target, used to produce the secondary beam for the NA61/SHINE experiment. The cavern is placed about 11 m underground in order to dump the radiation produced in the collisions of a high intensity beam with the target material. While about 40% of 10^{13} beam protons per cycle interact with the target, the rest is dumped in a controlled way in the TCC2 cavern.

The T2 target consists of several beryllium plates of different length, so that the target thickness might be optimised according to the requested yield of secondary particle and its momentum. The target thickness used to prepare secondary proton beams for the NA61/SHINE experiment is either 100 or 180 mm.

An optimisation of the beam composition is done using a set of upstream dipole magnets. They allow for using a single target to feed 2 adjacent beamlines with particles produced at 2 different production angles by setting up so-called wobbling angle [60].

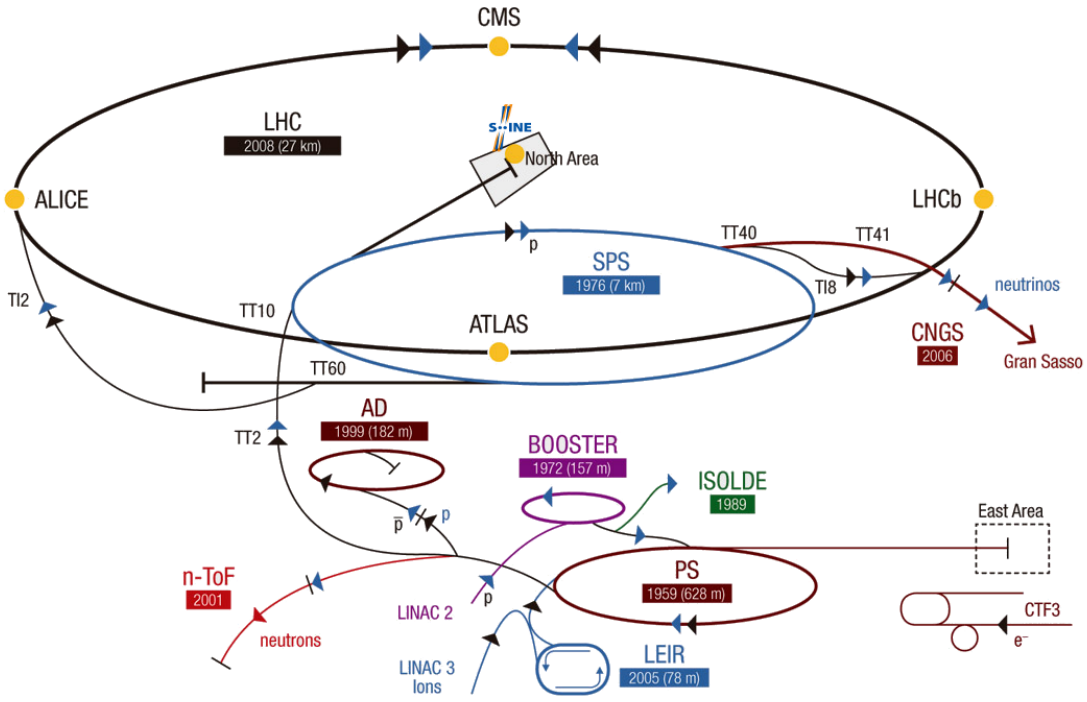

Figure 4.2. The accelerator complex at CERN. NA61/SHINE is placed in the North Area at a point marked with the SHINE logo.

The beam consists of different hadrons, mainly protons, pions and kaons, as well as of other particles (electrons, muons) created mainly in the interactions with the collimators or the beam aperture limits.

4.1.3 The H2 Beamline

The secondary beam produced in the interactions with the T2 target is transported using the H2 beamline (Fig. 4.3. The beamline makes possible to transport charged particles of momentum ranging from about 9 GeV/c up to the SPS top momentum of 400 GeV/c. The distance between the T2 target and the NA61/SHINE production target equals to 535 m. The beamline is also prepared to transport a low intensity primary beam of protons or ions.

The beam line is basically build of 2 large spectrometers. The momentum selection is done in the vertical plane, where the particles are filtered out according to their rigidity.

As the beam consists of a manifold of particles, selection of the beam particle is done using Cherenkov counters: CEDAR [61] differential Cherenkov counter and a threshold Cherenkov counter, described further in Section 4.2.

The beam is focused at the NA61/SHINE target. Width of the beam spot at

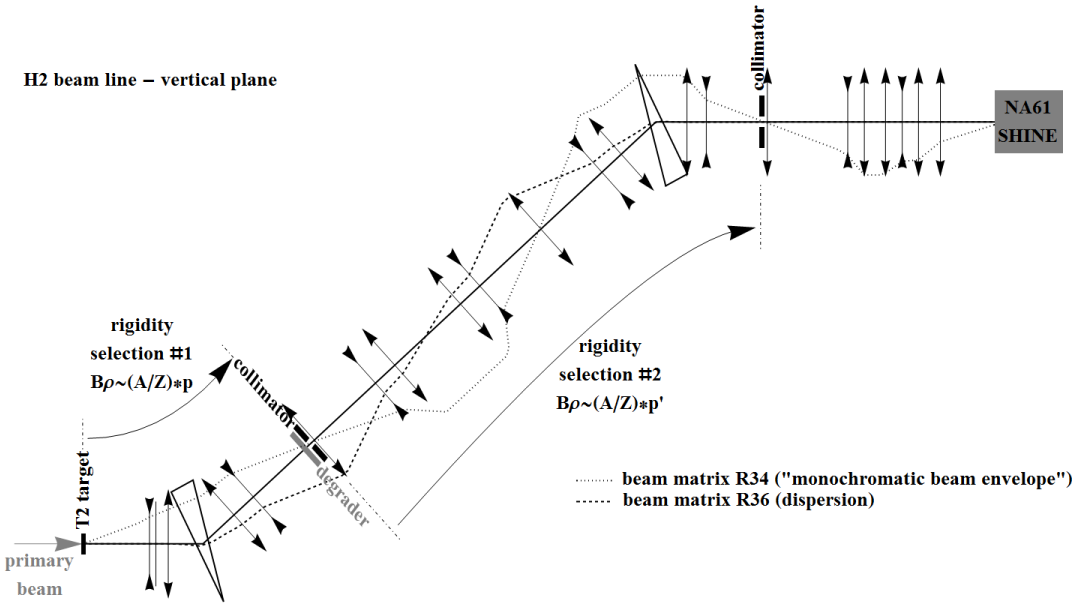

Figure 4.3. Layout of the H2 beamline [59].

the target is described by RMS slightly larger than 2 mm for the momenta about 20 GeV/c and 1.2 mm at 158 GeV/c. The momentum spread is lower than 1% and the divergence is less than 0.2 mrad.

4.2 Beam Detectors and Trigger

4.2.1 Cherenkov Counters

Gas-filled Cherenkov counters are used to select the beam particles of given type. Two such detectors are used in the H2 beamline: the Cherenkov Differential Counter with Achromatic Ring Focus (CEDAR [61]) as well as a threshold Cherenkov counter (THC),

The CEDAR is placed in a location, where the beam shows almost no divergence. The CEDAR is equipped with a special optical system allowing to focus the Cherenkov light onto the plane of the diaphragm. The opening of the diaphragm is tunable in order to optimise the light intensity and the width of the peak for given particle in the pressure domain. Each type of particle might give signal only within the narrow limits about the pressure characteristic to that type of particle. The position of the peak depends on the gas composition and the temperature, as the Cherenkov angle depends on the density of medium. There are two types of CEDAR detector: CEDAR-N is operated with helium and it is used for beam mo-

menta higher than 60 GeV/c, whereas CEDAR-W is nitrogen-filled and operated for lower momenta. There are basically no differences in the principle of work between those two types of CEDAR.

The light from the diaphragm is registered by 8 photomultiplier tubes (PMTs), positioned symmetrically around the beam axis. Because of that, it needs for a careful adjustment in order to centre its optic with respect to the position of the beam. A coincidence logic is used to form 6-, 7-, and 8-fold coincidence signal. The trigger logic makes use of the 6-fold coincidence as a particle identification tag.

In addition to the CEDAR, for beam momenta in the range of 20-40 GeV/c the THC detector is used. It is mainly operated with nitrogen. After tuning the pressure to the beam composition and the given particle type to be measured, the signal is visible for all the particles of mass below that of the given particle. Thus, this signal is used by the trigger logic in anti-coincidence.

Not more than 0.8% of the particles are misidentified.

4.2.2 Trigger Counters and Definition

A number of scintillator detectors is used to define the beam position and its interactions. First of them is placed about 30 m upstreams the target, the last one just between the VTPC-1 and VTPC-2. All of them are made of BC-408 plastic.

The S1 scintillator detector is a 5 mm thick square-shaped block, that measures 60 mm in length. 4 PMTs are attached directly to the side of the active volume, as the detector provides with signal for time-of-flight measurements. In addition to that, it defines the number of beam particles coming to the NA61/SHINE experiment.

The V0 counter is a 5 mm thick detector, shaped as a circle, measuring 80 mm in diameter. There is a hole in the centre of the plastic measuring 10 mm in diameter. This detector acts as a veto scintillator, used in order to remove the interactions with the beam halo.

The S2 counter is a lollipop-shaped detector with the active volume of 2 mm thick scintillator, measuring 28 mm in diameter. It is mainly used to define the central part of the beam.

The V1 counter is paddle-shaped detector with a 10×10 cm wide square-shaped active area. A hole of 8 mm in diameter is drilled in the middle of the area. The thickness equals to 5 mm. This detector is used in a similar way as the V0 detector, as a veto detector to reduce the halo contribution to the main interactions.

The active area of the S4 counter is 5 mm thick cylinder with 20 mm in diameter. This is the only counter used in this analysis, that is placed downstream of the target. This counter defines the number of beam particles that did not interact with the target. It is used in veto in the definition of interaction trigger.

In addition to the V0 and the V1 veto-scintillators, a paddle with a hole of 20 mm in diameter is used to increase the efficiency of those detectors. In dependence on

the position, it is dubbed V0' if it is placed near to the V0 counter, or V1' if it is used to double the V1 counter.

The trigger definition for inelastic interactions with identified beam proton is the following: $S1 \cdot S2 \cdot \overline{V0} \cdot \overline{V1} \cdot \overline{V1^p} \cdot \overline{S4} \cdot CEDAR$

4.2.3 Beam Position Detectors

The Beam Position Detectors (BPDs) are responsible for tracking the beam particles for the reconstruction of the main interaction vertex. The BPDs are proportional chambers filled with the mixture of 85% Ar and 15% CO_2. The active area of the detectors is 48×48 mm^2. Each detector consists of three cathode planes made of aluminised 25 μm Mylar separated by two orthogonal anode wire planes (15 μm tungsten wires with 2 mm pitch). The outer cathode planes are divided into strips of 2 mm pitch.

A particle crossing the active area induces charge deposition in about 5 strips. The position of particle transversing the detector is found by calculating the mean position of the charge cluster on each plane using the so-called centroid method. An extrapolation to the interaction plane is made using least-square fitting.

4.3 Time Projection Chambers

The NA61/SHINE experiment utilises 5 high-resolution Time Projection Chambers (TPCs), two of which (Vertex TPCs: VTPC-1 and VTPC-2) are placed in the magnetic field of the superconducting magnets (VTX-1 and VTX-2). Between them, there is placed the GAP-TPC, which is used to track the particles produced at very small angle. Additionally, two big Main TPCs (MTPC-L MTPC-R) are placed in the downstream direction.

The maximum bending power achievable for the combination of both magnets equals to 9 Tm. The standard configuration of the magnetic field is 1.5 T in VTX-1 and 1.1 T in VTX-2. It is used for the beam momentum of 150 GeV/c and more. For the lower beam momenta used in the experiment, the magnetic flux density is scaled by the same factor in both of the magnets.

The VTPCs were optimised in order to measure pions about mid-rapidity in the VTPC-1, and the V^0 particles in the VTPC-2 [56]. Each of them consists of 2×3 sectors, placed symmetrically about the beamline. The measurement is taken using 24 rows per sector, each row consisting of 192 pads. The dimensions of a single VTPC are 250×200×98 cm^3.

Between VTPC-1 and VTPC-2, in the volume with negligible magnetic field, there is placed a special detector the GAP-TPC. It is installed directly on the beamline, therefore its material budget has been reduced to an inevitable minimum. The main

purpose of installing the detector was to improve the accuracy of backward extrapolation in the case of high energy tracks. Additionally it made easier to distinguish high momentum tracks from conversion electrons for the configurations where no signal is registered in the VTPCs. The GAP-TPC consists of only one sector, containing 7 padrows of 96 pads each. Its dimensions are following $30\times81.5\times70$ cm^3.

The MTPCs were designed mainly to perform excellent specific charge loss measurements due to high number of charge clusters (dE/dx resolution better than 4%) [56]. Right this fact is crucial for particle identification used mainly for fluctuation analysis. Each MTPC consist of 5×5 sectors. Each sector is built of 18 padrows. As the charge density is higher near to the beamline, the sectors adjacent to the beamline are equipped with 192 pads a row, whereas the remaining 20 sectors have only 128 pads a row.

This gives a total of over 180 000 pads. Each pad provides with signal, which is projected against arrival time to get 3-dimensional particle trajectories used for tracking.

4.4 Target

In order to measure interactions with protons, a 20.29 cm long liquid hydrogen target (LHT) was used. The target length corresponds to 2.8% interaction length for p+p interactions. The target is cylindrical in form and the diameter equals to 3 cm. It was placed in the beamline 88.4 upstreams from the VTPC-1. The target was filled with para-hydrogen (ρ_{LH} =0.07 g/cm^3 at the atmospheric pressure of 965 mbar). Alas, since the boiling rate of the hydrogen was not monitored during the experiment, the density is know only approximately. The density of the gaseous hydrogen left over after removal of liquid hydrogen relative to the liquid hydrogen was estimated using ratio of high multiplicity events to vary between ρ_{GH}/ρ_{LH} =0.4% and 0.6%. Thus, the operational conditions were not stable during data taking period. This does not allow to estimate total/total inelastic cross section for p+p in this experiment.

4.5 Data Acquisition System (DAQ)

The readout electronics consists of three main parts: readout of the TPC front-end electronics (FEE), FASTBUS-based tof-system, and CAMAC-based beam detectors (Fig. 4.4).

For the TPC, the FEE contain preamplifiers, shapers, time-sampling arrays, and ADCs, whereas the readout motherboards steer the time sampling, ADC conversion and data transmission. The data stream is governed by low-level electronics, which works in push-data mode.

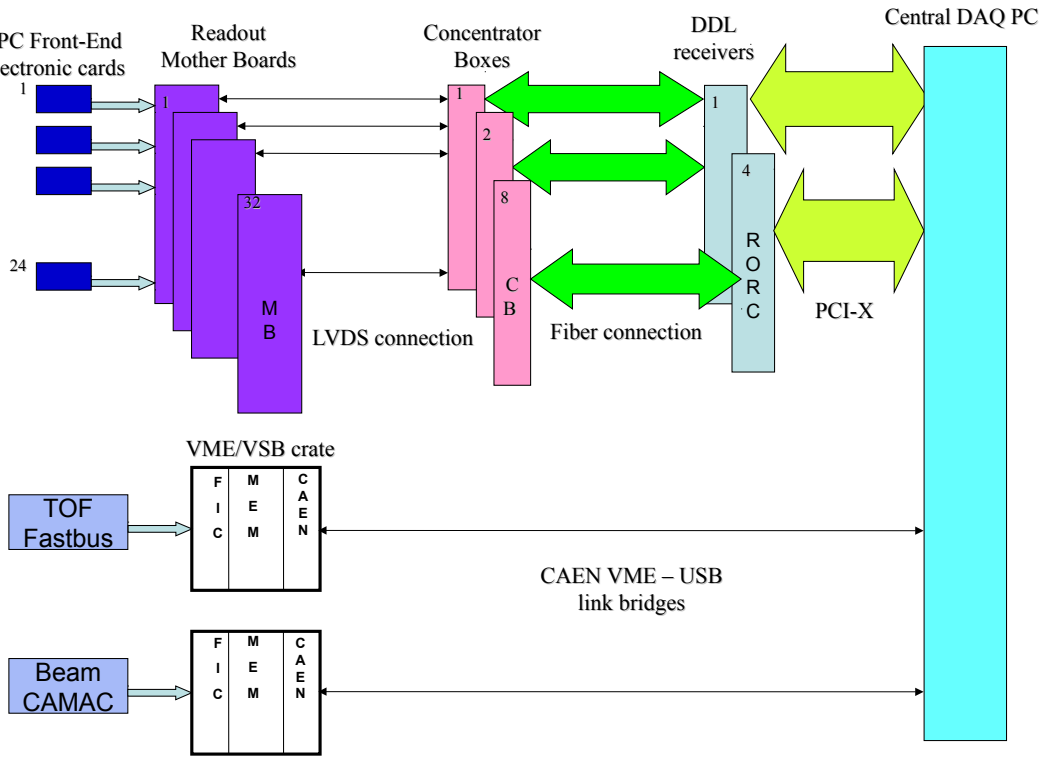

Figure 4.4. Block diagram of the three main parts of the NA61/SHINE readout system [59].

The tof- and CAMAC-systems are connected to VME crates via respective bridges. The crates contain a controller running a low-level DAQ. External interrupt signals are used to initiate data-taking. The accurate pre-trigger signal initiate the measurement, but the data are read out only if the main trigger is received within a time limit. As the trigger works asynchronously, the synchronisation follows via trigger counters. The synchronisation is verified each minute.

Chapter 5

Analysis

Aim of the analysis is the calculation of the dependence of Λ-yields on rapidity and transverse momentum (y,p_T), rapidity and transverse mass (y,m_T), as well as Feynman-x and transverse momentum (x_F,p_T). As a neutral particle, Λ is identified after the charged products of its main decay channel, registered in the TPCs (Section 3.3).

The data set used for the analysis was acquired by the NA61/SHINE experiment in 2009. The reaction, for which the analysis has been applied is p(158 GeV/c)+p.

This chapter starts with a brief introduction to the reconstruction chain, followed by a thorough description of the V^0 analysis, i.e. the quality cuts used in order to define inelastic events of good quality and to decrease the level of the combinatorial background, the procedure aiming at extraction of Λ-particles from the combinatorial background, the normalisation, and the corrections for feed-down, geometrical acceptance and reconstruction efficiency.

5.1 Track and Main Vertex Reconstruction

Raw data contain the detector response as the signal recorded on event-on-event basis. The data are stored on tape within the CERN Advanced STORage manager (CASTOR) system.

The data are used first for the reconstruction of particle tracks and the main interaction vertex, inevitable for the momentum calculation.

The reconstruction chain is a collection of procedures, called clients, which are run serially one-by-one, i.e. the results of each step are used as an input for another step. Some of these procedures are not only responsible for track and vertex reconstruction, but also implement corrections. corrections. The clients are written in FORTRAN and C. They have to be wrapped in order to use them within the NA61 native software environment (SHINE) in a direct way.

The reconstruction chain start with the track reconstruction. Before the first client

could be run, a calibration of the TPC-pulse height might be performed. This is done by allowing some radioactive ^{83}Kr to diffuse into the standard gas mixture used in the chambers. ^{83}Kr is used mainly due to a well localised energy deposition of its decay products. The signal from ^{83}Kr is used to equalise the signal of the VTPC and MTPC pads in all the channels of TPC-electronics [62]. In fact, this kind of calibration has never been applied to the NA61/SHINE reconstruction chain.

Another kind of information needed as an input for the reconstruction is the geometry calibration. This is done by undertaking geometrical measurements of the position of specially chosen characteristic points of the detector system with the use of laser. This makes possible to find position and orientation of the detectors.

The magnetic field in the region of the VTPCs was measured for the configuration with maximal bending power, that can be obtained using the vertex magnets. This configuration, denoted as 160 GeV/c-configuration, is used for data-taking with all beam particles of momentum at least 150A GeV/c, i.a. the 158 GeV/c protons. The field map for this configuration, obtained using Hall-probes, is an inevitable input for the reconstruction. If beam particles of lower momenta p_{beam} are used, this map is rescaled by $p_{beam}/160$.

The magnetic field was checked for an accidental rescaling (e.g. due to some changes in the electronic modules controlling the current, hysteresis etc.) using a subset of fully-reconstructed data. The invariant mass distribution of K^0_S and Λ were used for this check. For this analysis, two invariant mass distributions are prepared for each V^0-particle, under the condition that both daughter tracks are registered within the volume of only one VTPC detector: one histogram is prepared to check the field in the VTPC-1, where all the tracks crossing the VTPC-2 are discarded, and another histogram used to check the field in the VTPC-2, where the tracks with at least one cluster in the VTPC-1 are rejected. For this analysis, it is of no meaning if the track was registered in the MTPCs or not.

The invariant mass of K^0_S is calculated from the Eq. (3.7) under assumption both products are of equal mass of charged pion ($m_{\pi^\pm}$). K^0_S has priority over the mass of Λ, as it is more sensitive to the changes in the field, due to its lower mass. The signal (Lorentz function) and the background (Chebyshev polynomial) are fitted. The position of the signal peak m_0 is read and saved. In addition to that, the same procedure is repeated for momenta p of the decay products rescaled by a factor w within the range from 0.95 to 1.05. Then, a plot of the centre of the signal peak as a function of the scaling factor $m_0(w)$ is prepared The value of w for which the function reach the PDG value of the particle chosen for the analysis is read as a scaling factor for which the mass is properly reconstructed in given detector w_0. If $w_0 \neq 1$ a correction to the magnetic field is introduced by scaling it by a factor of $1/w_0$.

This method will be replaced in the near future by another one, fitting the V^0s

using their local (single VTPC detector) tracks. The currently used method gives good result only if the field is rescaled by the same value in a whole detector. If the magnetic field disturbance is not uniform, this method does not help, as it averages the effect using just a part of a VTPC detector, for which the tracks are not possible to be registered in the other VTPC detector. The corrections introduced using the currently used method are in no wise wrong, and they are always checked for the impact on the invariant mass distribution of all the tracks (including those registered in more than one detector), but any possible improvement and generalisation of the method has to be considered and applied if possible.

In addition to aforementioned corrections, the further corrections concerning distortions due to local inhomogeneity of the electric drift fields as well as the $E \times B$-effects are included. The latter correction is caused by non-parallel orientation of E- and B-fields. Also the temperature, atmospheric pressure, and the drift velocity are measured in a continuous way all the time during measurement to be used for corrections. As the signal processing time of each channel of the electronics is different, this effect is also corrected for.

The first client run in the very beginning of the reconstruction chain is the cluster finder. It looks for coincidences between the ADC values on the pad-time basis, for each padrow separately. The points for which the ADC value exceeds a constant limit of 5 are treated as signal forming a part of a cluster. The limit on ADC is set mainly to cut off the noise. If the signal is found also in the neighbouring points on the pad-time plane, it is added to the same cluster. This is done for each point that is separated from the cluster by not more than 3 units in either dimension. All the points forming a cluster are used to calculate its position as a weighted mean, which is calculated using the physical position of the pad's centre and it is weighed by the ADC value registered by the pad. In addition to that, the total charge registered by each pad is added up to find the mean energy deposition per cluster [56].

Even if all the aforementioned corrections are applied, some systematic effects are still observed. They are corrected for by applying a phenomenological method called residual correction. Residua are calculated from a reconstructed test-subset of data. Residuum is a term for a measured difference in position between the reconstructed tracks and the corresponding cluster centres. This is done with the use of all the possible corrections except of the residual correction. The deviations are written to a file. This mapping is used to adjust the cluster positions before the reconstruction to reduce the systematic effects of unknown origin.

The next step is the reconstruction of tracks. For that, let us introduce the coordinate system used in the experiment (Fig. 4.1). It is a right-handed coordinate system with z-axis pointing in the beam direction. Therefore, y is a vertical axis and x is a horizontal axis pointing to the left if observed in the positive z-direction. As the MTPCs are placed outside of the magnetic field, the tracks found there are

expected to be straight. For the VTPCs the situation is different. Magnetic field is applied in y-direction. Thus, the tracks are straight only in the projection on the zy-plane, whereas for the zx-plane they should form an arc. In fact the tracks differ a bit from a circular shape, as the field is not totally homogeneous and the particle lose on energy while transversing the gas volume.

The very first part of the track reconstruction takes into account only the straight tracks in the MTPCs. Their momenta are estimated under assumption they are produced in a main vertex with position fixed to the middle of the target.

Then, those tracks are extrapolated in backward direction and the tracks in the VTPC-2 are searched for. If no clusters forming tracks are found in the VTPC-2, although the prediction from the MTPC-extrapolation placed them there, the MTPC points used for this prediction are freed from the track for a possible use in the future.

Afterwards, local tracks in the VTPC-2 are looked for, i.e. the tracks, which were not predicted using the data from the MTPCs. If found, they are extrapolated forwards and the clusters from the MTPCs are carefully looked into in order to find if there are some previously unrecognised tracks, which correspond to the local tracks found in the VTPC-2.

The following step is the search for the track clusters in the VTPC-1 in regions neighbouring to the backward-extrapolated tracks found in the VTPC-2 and the MTPCs. Not finding a predicted track in the MTPCs, results in removing the MTPC clusters from the track for further use.

After this, a search for local tracks in the VTPC-1 follows. If found, a forward extrapolation is done, and if a cluster in the MTPCs is not assigned to any track, it is examined for being a part of a forward-extrapolated VTPC-1 track [56].

Up to now, all the tracks coming from the main interaction vertex are reconstructed. Now, all the other (inclusive freed) MTPC tracks are reconstructed without assumption they come from the main interaction vertex.

The momenta are calculated using the global tracks found in the procedure described above. using a backward extrapolation applying

Position of the main interaction vertex in x and y is reconstructed using the beam tracks registered in the BPDs. The z-component of the main vertex is calculated from a backward extrapolation of all the reconstructed tracks in the target direction with the use of a Runge-Kutta approximation of 4^{th} order [63]. The z-component of the point, where most of the tracks cross each other, is assigned to the z-coordinate of the main vertex. The position is calculated with precision of 40 μm. The main vertex is used as a reference point to recalculate the momenta.

Then, the maximal number of clusters, that could be registered for a reconstructed track, is calculated from the geometry of the track. Such number of potential points is greater than or equal to the actual number of clusters, for a physical track can e.g.

cross the regions where there are some noisy or dead channels. The number can be used for some further cuts to restrict the analysis to the tracks of the best quality. It is also used by a client merging the split tracks.

5.2 V^0-Reconstruction

It is possible to reconstruct V^0 decay vertices by their decay topology (see Chapter 3). If a track contains at least 10 clusters in VTPC-1 or VTPC-2, it is backwards extrapolated with the use of Runge-Kutta method [63]. Each approximation step is 2 cm long. All the positively-charged tracks are combined with all the negatively-charged tracks in pairs. The distance of the closest approach l_{DCA} is calculated for each track combination as a length of a shortest line segment bounded by any point in one of the tracks and another point in the other track. If $|l_{DCA}|$ <2.5 cm in both x- and y-direction the pair is accepted as a V^0-candidate – these particles possibly come from a V^0 decay.

A number of cuts are used in order to optimise the procedure in such way, that the lowest possible number of true V^0-vertices gets lost, and as many false V^0s as possible are removed. First of all the secondary vertex should be positioned not further than 78 cm upstream to the centre of the NA61 liquid-hydrogen target to reduce background from the interactions with the beam instrumentation.

Another cut makes sure the V^0 track comes from the main interaction vertex. The difference between the main vertex position and a crossing point defined by an intersection of the V^0 track and the plane spanned by vectors parallel to x- and y-axis with a common start point in the main interaction vertex has to be below 25 cm in both x- and y-direction. Direction of a V^0 track is defined as the direction of the total momentum of the V^0 decay products. This cut helps in particular to reduce background due to off-time particles, but a value for the reconstruction is quite loose, so it has to be refined in the further analysis.

The only kinematic cut applied is the p_T^{Arm} <0.5 GeV/c, where p_T^{Arm} is defined in Eq. (3.2). This cut is used mainly to reduce the accidental combinations.

The efficiency of the full reconstruction of V^0-vertices is consistent with 1.

For each V^0-candidate which passed the cuts, the momentum of both daughter tracks is recalculated together with the position of the secondary vertex. This is done by applying a Levenberg-Marquard procedure [64,65]. The daughter tracks are treated as a pair coming from the same vertex and both 3 vertex coordinates and 2×3 momentum coordinates are fitted altogether.

5.3 Event Selection

In the scope of this thesis are the results for p(158 GeV/c)+p interactions acquired by the NA61/SHINE in the year 2009. A total of $3\,549 \times 10^3$ events acquired with the liquid hydrogen (LH) inserted configuration of the target and 427×10^3 with the hydrogen removed were used for the analysis. The number of events after the quality check described in this section ($N^I = 1\,655 \times 10^3$ for the target inserted, $N^R = 43 \times 10^3$ for the target removed) is treated as raw number of inelastic events. The events for the LH removed configuration were measured for corrections (Sections 5.6 and 5.7).

Also a simulation was made with the use of EPOS model [66] as a generator. All the generated particles were processed in Geant3, where the transportation is performed and interactions with the detector material were simulated. The output from Geant3 was further processed using the same reconstruction chain, as in the case of experimental data. The total number of generated MC-events is $N_{MC}^{gen} = 19\,961 \times 10^3$ ($N_{MC}^{acc} = 15\,607 \times 10^3$ after application of the event selection procedure). MC-simulation is used to correct for detection inefficiencies (Subsection 5.6.2), due to kinematic and quality cuts used in the analysis.

The selection of properly reconstructed inelastic events was made using the following cuts:

- A maximal number of triggers running at once equals to 4. Each of them can be downscaled by letting exactly each n^{th} trigger of one type start recording the data (the main trigger). This is done with a 12 bit prescaler. In order to enable event-by-event offline selection, the triggers as well as the responses of the beam detectors are recorded in a pattern unit. In the analysed period of data-taking, all 4 triggers were run.

  Only the inelastic interactions with the beam proton $T2 = S1 \cdot S2 \cdot \overline{V0} \cdot \overline{V1} \cdot \overline{V1^p} \cdot \overline{S4} \cdot CEDAR$ were selected for the analysis, where $T2$ denotes the trigger definition, and the other symbols stand for signals from the respective beam detectors described in Chapter 4. This trigger was not downscaled for it is the trigger of the highest priority, i.e. each occurrence of the T2-pattern was recorded. The other triggers were recorded mainly for diagnostics.

  Only the inelastic events were simulated in the MC, what makes quite important to use a good definition of inelastic events in order to take an analogous subset of data for analysis in the case of both experimental data and the MC. This is mainly done by using vetoed S4-signal in the trigger definition.

  For the MC-simulation uses only a well-defined proton beam, it does not need a full trigger running. The only part of the trigger, which might cause some problems is S4 due to its inefficiency. It is possible, that even in the case of

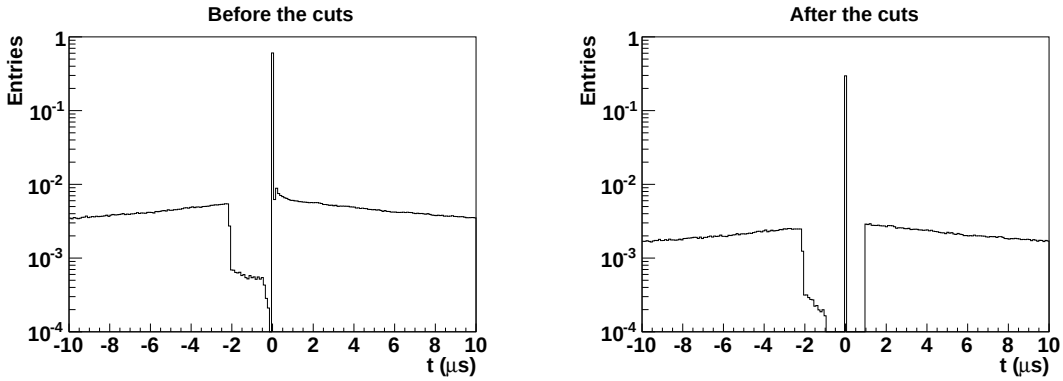

Figure 5.1. Timing of the beam particles with reference to the main trigger for the LH inserted configuration of the target. In the case the event contain some off-time beam particles, only the timing of the nearest one with respect to $t = 0$ is shown. *Left:* Before the event cuts there are some off-time particles in a region, for which it is impossible to discard the interaction caused by them with the use of some other cuts. *Right:* A 1 μm-wide off-time particle-free window is visible after the event cuts.

an inelastic event some charged particles are registered within the volume of S4, what reduces the phase-space of the true inelastic events. The most important thing now is to reduce the phase-space in the MC simulation in the same way, as it is the case for the experimental data. The response of S4 was simulated and it was found that about 10% of true inelastic interactions are discarded due to a particle transversing the active volume of S4. The correction for that effect is made by discarding all MC-inelastic events, where S4 is hit by a charged particle. This condition is equivalent to the T2 trigger in case of the MC-data.

- The timing of the interacting particle and of another particles incoming within a ± 25 μs-wide window centred at the time of the main trigger is stored using a waveform analyser (WFA). The probing frequency of this device equals to 10MHz.

  Timing for two signals is recorded. The first is the signal from the S1-detector, which corresponds to the beam particle, the second is the T4-trigger, which corresponds to an inelastic interaction with any beam particle. Timing is made with reference to the signal of the main trigger. The signal from a beam particle coincident with the interaction gives either of the two values: -100 or 0 ns. The presence of 2 values for an event of constant timing results mainly from the probing frequency.

  In order to get rid of the off-time beam particles, possibly interacting within the detector material, the events where another beam particle is registered within 1 μs window were discarded using the WFA (Fig. 5.1).

  This value was optimised not to discard a high number of events, and to prevent the interactions with an unknown beam particle from being assigned to an in-

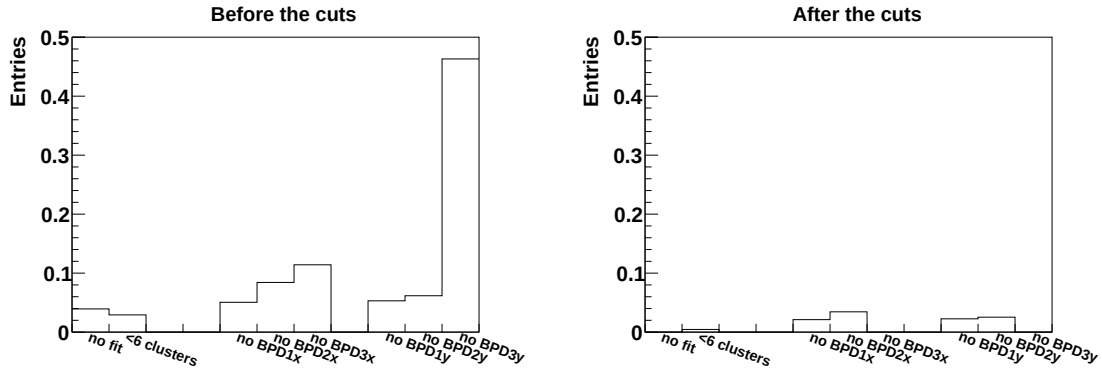

Figure 5.2. The flags showing the problems with the BPD-fit. Each plot is divided into 3 sectors. The first shows a serious problems like no fit or a cluster totally missing. The second shows problems with the position calculation in x-direction, and the third in y-direction. Both latter sectors indicate missing data-points, mainly due to double-hits or distorted shape of the signal for respective plane and detector. *Left:* Before the event cuts. *Right:* After the event cuts: Only one BPD-1 or BPD-2 position coordinate might be missing from fit. BPD-3 is used to make sure a beam particle did not rescatter before the target.

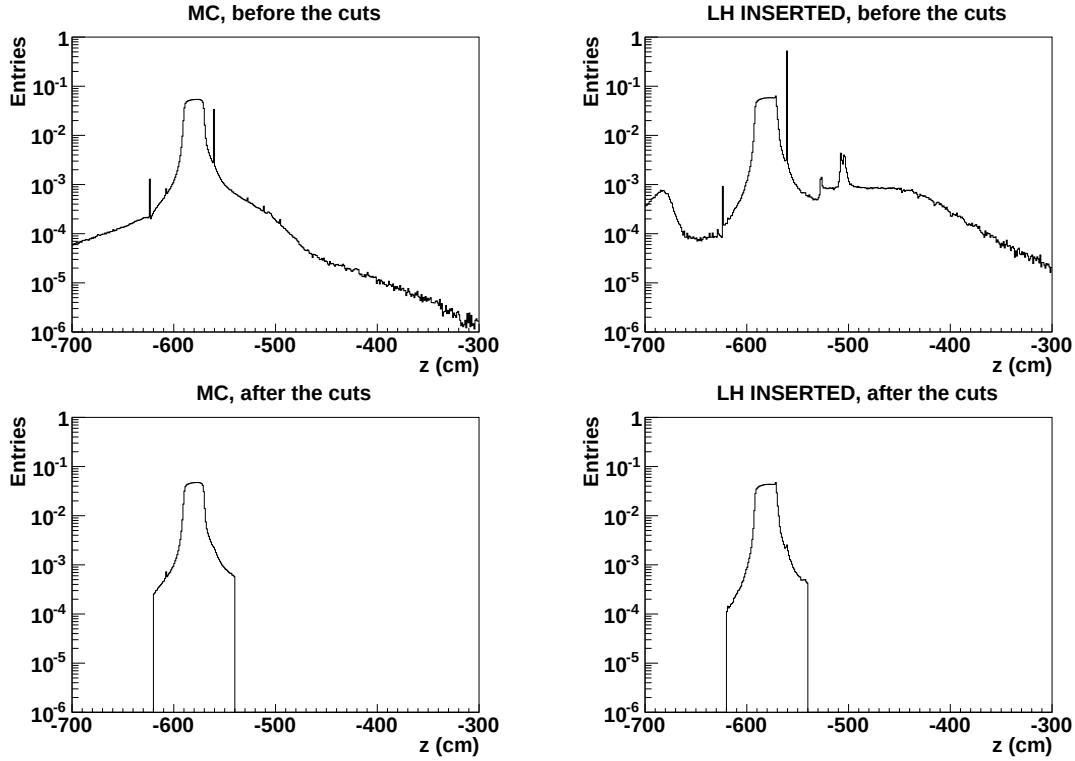

Figure 5.3. Main vertex z-coordinate. *Top:* Before the cuts. A peak for the experimental data (*right*) at z=-560 cm is of artificial origin and comes from the events with an ill-fitted main vertex. The other peaks are due to windows of the detectors. These structures are not well reproduced in the simulation (*left*). *Bottom:* After the cuts. Only the target region is used for the analysis. The main difference between the simulation and the experiment is an asymmetry on the level below 1%.

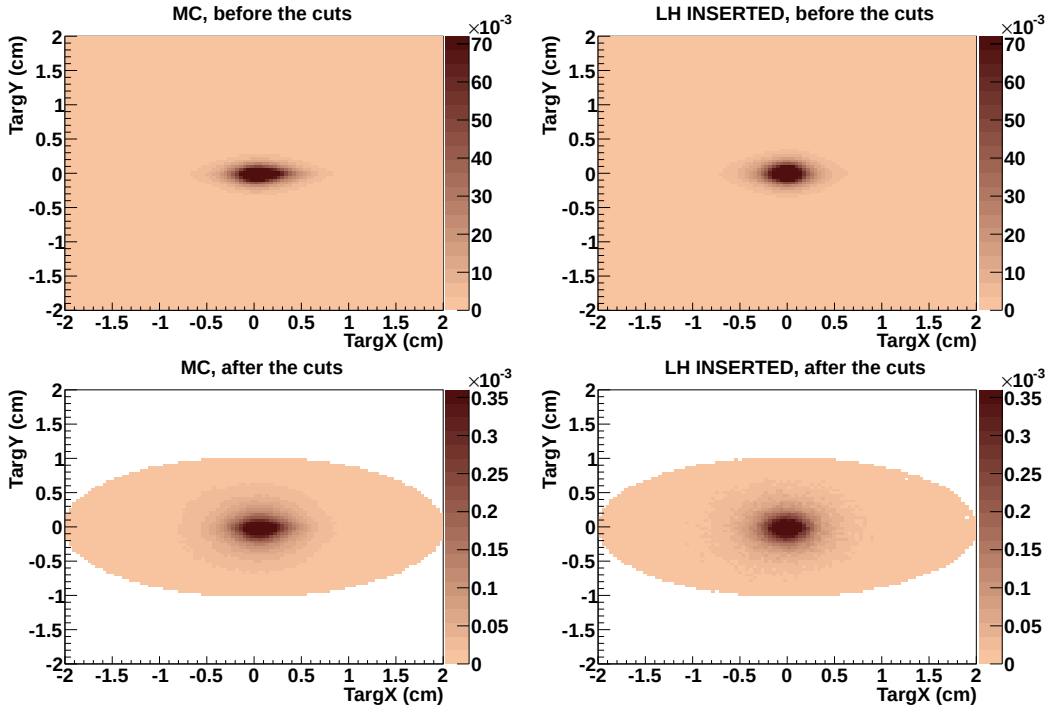

Figure 5.4. Position of the extrapolated V^0 track on the target plane calculated with respect to the main vertex. *Left:* Simulation. *Right:* Experiment (LH inserted configuration of the target). *Top:* Before the V^0 cuts. *Bottom:* After all the cuts, except of dE/dx and matching.

elastic p+p event. The width of the off-time particle-free window suffices, as the charge drift in the TPCs makes asynchronous events be translated vertically from each other, and therefore the momenta of the off-time particles are clearly visible not to come from the main interaction vertex, if the time difference is higher than 1 μs. This cut is of high importance, as the simulation included only the interactions with a single beam particle. An application of the cut is the easiest way to correct for double-particle hits, the rate of which increase significantly with the beam intensity.

- As a good quality fit of the beam particle position in the BPDs is required to assure a right calculation of the x- and y-position of the primary interaction vertex, events containing double hits and the events where information on more than one coordinate is not properly measured or one coordinate is missing from either of the downstream BPDs are not processed in the further analysis (Fig. 5.2).

- Z-position of each primary interaction vertex is fitted well. Only the converged fits for which the z-coordinate differs by not more than 40 cm compared to the position of the target centre (-620 cm) are taken into account (Fig. 5.3).

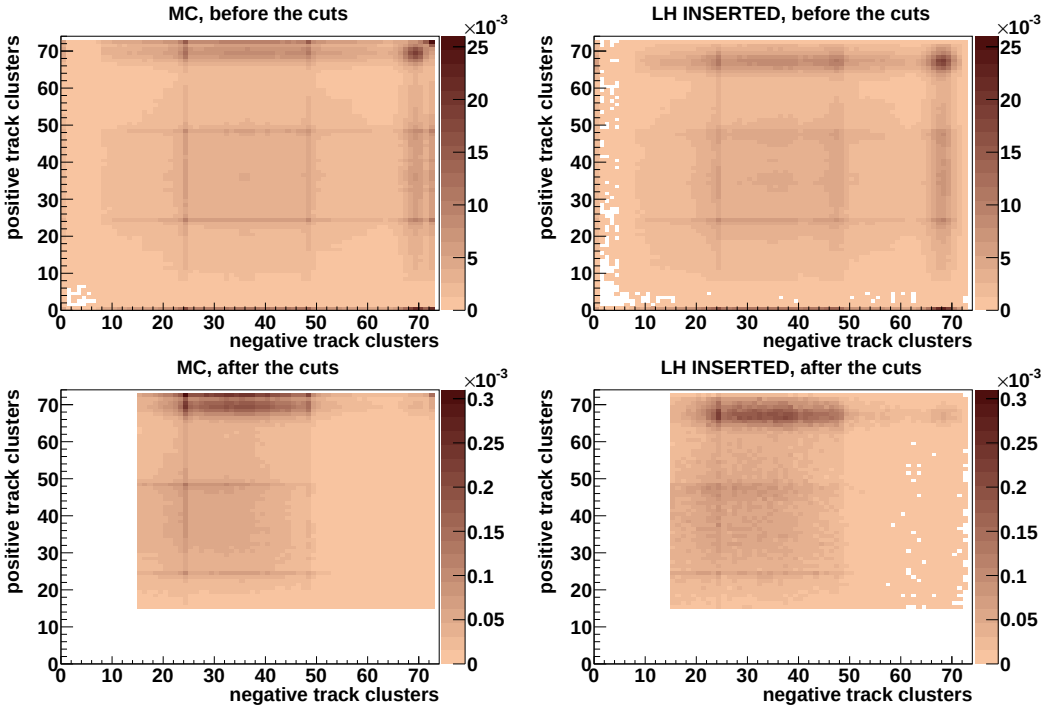

Figure 5.5. Maximum of two values: clusters count in VTPC-1 and VTPC-2 in dependence on V^0-track charge is shown. The same structures are visible in both simulation and the experimental data. *Left:* Simulation. *Right:* Experiment (LH inserted configuration of the target). *Top:* Before the V^0 cuts. *Bottom:* After all the cuts, except of dE/dx and matching. The V^0-pairs, for which at least one track is of poor quality (less than 16 charge clusters measured), are discarded.

5.4 V^0 – Quality Cuts and Background Reduction

A number of V^0 cuts are applied in order to reduce background and make its shape easier to fit. Λ-candidates are selected following the same procedure for both experimental data and the simulation:

- In order to get rid of a significant part of interactions outside of the target material, the distance in xy-plane between the main interaction vertex and the intersection of the backward-extrapolated V^0-line with the target plane (a plane perpendicular to beam momentum containing the main vertex) should lie within an ellipse described by half-axes of 2 cm (horizontally) and 1 cm (vertically), as in Fig. 5.4.

- Number of charge clusters recorded in either VTPC has to be not less than 15 for each track (Fig. 5.5).

- In addition to those cuts, another cut is used in order to limit the analysis to the case, where only one decay vertex can be fitted to a pair of tracks. If a decay occurs in a magnetic field perpendicular to the decay plane, two topologies are possible, for the daughter tracks are of opposite charge (Fig. 5.6). One topology

is named sailor, where the magnetic field bends the particle on the left hand side to the left, and the particle on the right hand side to the right. They particles diverge from the beginning on, and only one vertex can be fitted in this case. The other is called cowboy, and the particle on the left hand side bend to the right and the other particle vice versa. Before the particles eventually diverge, they approach each other for a while until they meet in one point. This point might be interpreted by the reconstruction procedure as another decay vertex, thus any kinematic configuration which enables such a ambiguity is to be avoided.

If the decay plane is tilted, the tracks move in a spiral path, thus even the configuration similar to cowboy topology results in only one vertex found, as the vertical distance between the tracks increases with distance from the main interaction vertex.

The selection of the region where only one V^0 decay can be fitted is done by the means of $\cos\phi$, where ϕ is defined as an azimuthal angle between the vectors y', and n, where y' is a vector perpendicular to the momentum of a V^0-particle on the plane spanned by y-axis and V^0-momentum vector, and n is a vector normal to the decay plane (Fig. 5.7). This cut is rapidity depended. If all double-fits are discarded, the distribution should be approximately flat. A V^0-candidate is accepted if $|\cos\phi| < 0.95$ for $y < -0.25$, $|\cos\phi| < 0.9$ for $y \in [-0.25, 0.75)$, $|\cos\phi| < 0.8$ for higher rapidities (Fig. 5.8).

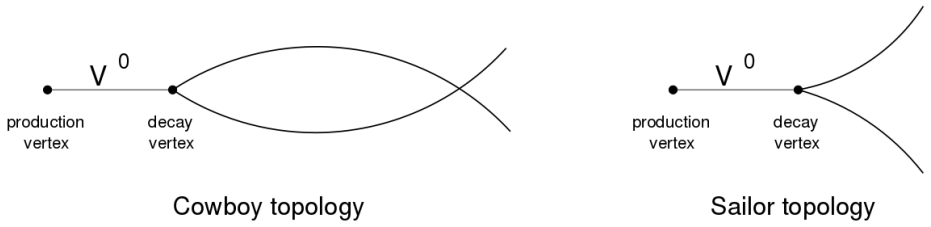

Figure 5.6. Two possible topologies of a V^0 decay [67].

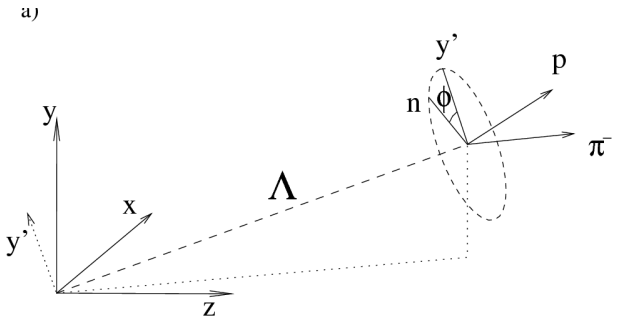

Figure 5.7. Definition of ϕ-variable.

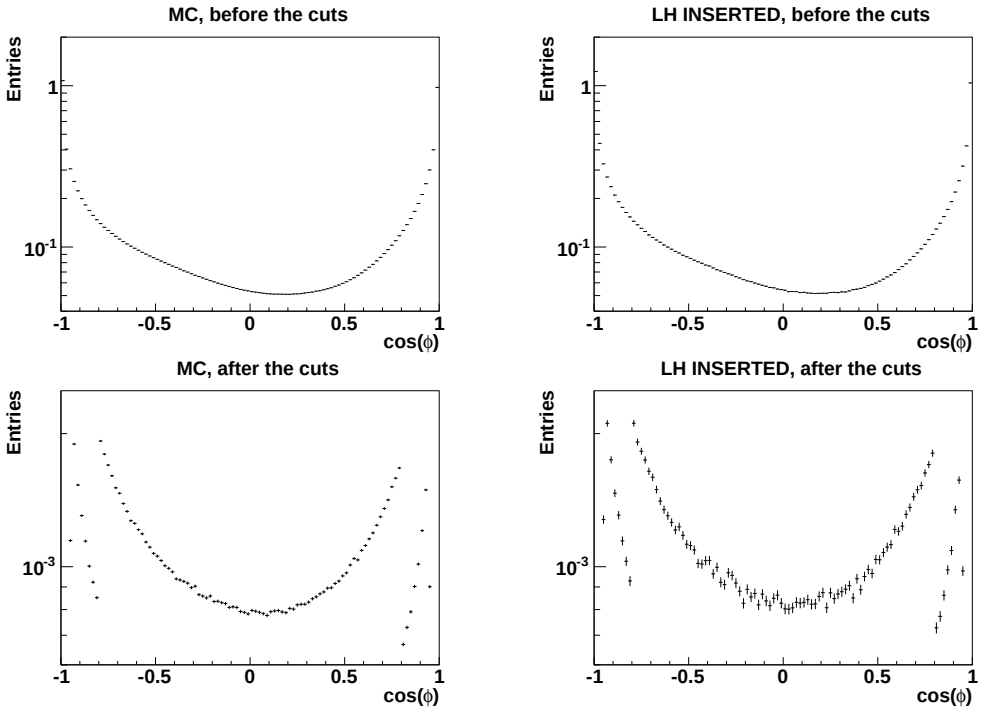

Figure 5.8. Cosine of ϕ. *Left:* Simulation. *Right:* Experiment. *Top:* Before the V^0 cuts. *Bottom:* After all the cuts, except of dE/dx and matching.

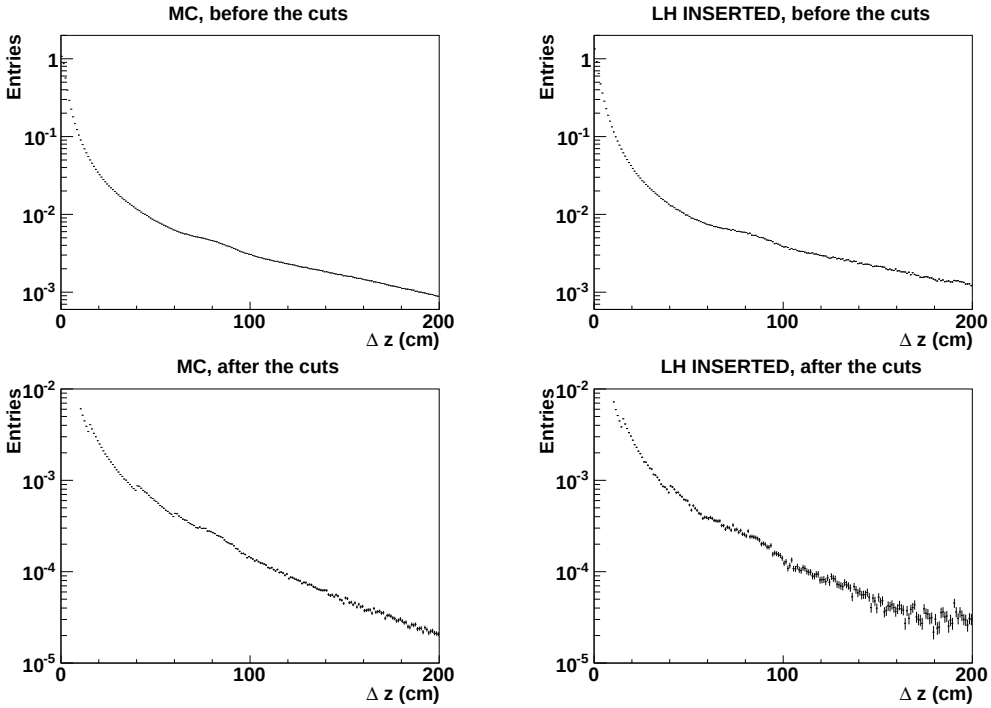

Figure 5.9. Distance between the V^0 decay vertex and the main vertex. The peak on the left hand side is due to some short-lived particles. *Left:* Simulation. *Right:* Experiment. *Top:* Before the V^0 cuts. *Bottom:* After all the cuts, except of dE/dx and matching.

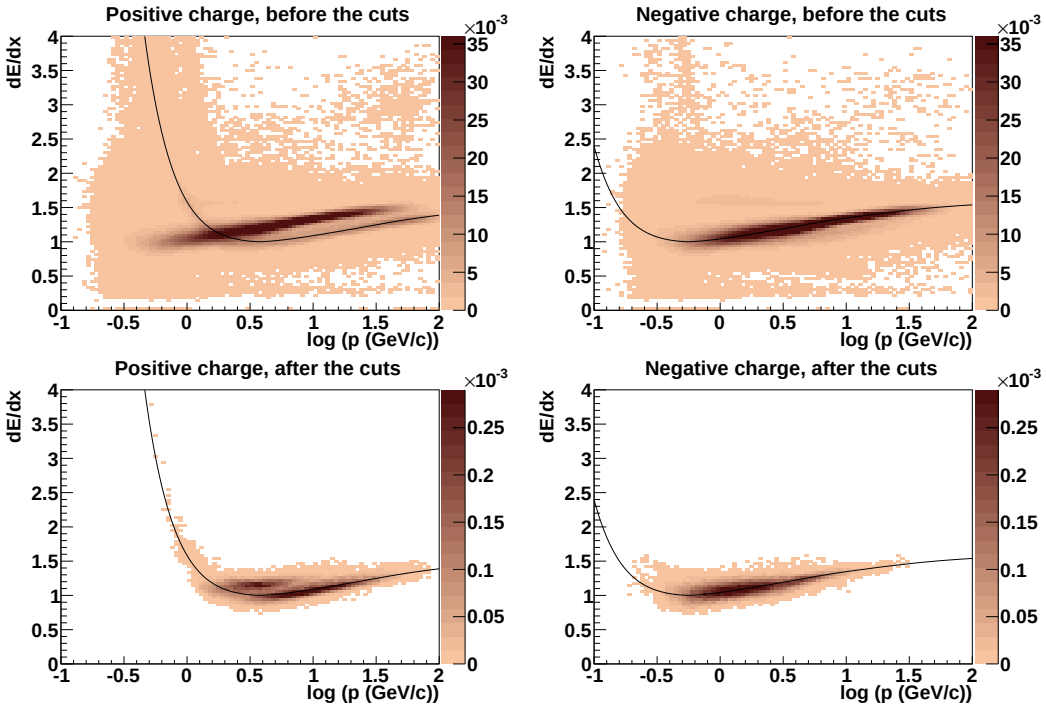

Figure 5.10. Specific energy loss in TPCs for the LH inserted configuration of the target, plotted for positively- (*left*) and negatively-charged (*right*) particles separately. *Top:* before the V^0-candidate cuts. *Bottom:* after the cuts a $\pm 3\sigma$-broad band around the Bethe-Bloch parametrisation is left over.

- Suppression of the combinatorial background is done on the basis of the distance between the secondary and the primary vertex (Δz). A V^0-candidate has to fulfil the following conditions: $z > 10$ for $y < 0.25$, $z > 15$ for $y \in [0.25, 0.75)$, $z > 40$ for $y \in [0.75, 1.25)$, and $z > 60$ for higher rapidities (Fig. 5.9).

- Identification of the decay products is made by means of specific energy loss within the active volume of the TPC-detectors (Subsection 5.6.3). As the $\Lambda \to p\pi^-$ decay is assumed, the difference in the specific energy loss for a positive/negative decay product can not differ from the Bethe-Bloch parametrisation for proton/π^- by more than 3σ (Fig. 5.10). This cut is applicable only to the experimental data, as no reliable dE/dx simulation for the NA61/SHINE setup exists. This cut increases the stability of results.

- For the simulated data the background was totally discarded by matching, i.e. checking the reconstructed tracks for maximal number of charge clusters common with the simulated tracks and taking for analysis only those, which correspond to the Λ-decay, regardless of the history of the parent particle. This cut is an analogue of the dE/dx cut, but of much better identification efficiency, consistent with 1 for the region within the detector acceptance.

These cuts enabled a very high reduction of background, which is visible in Armenteros-Podolanski plot (Fig. 5.11).

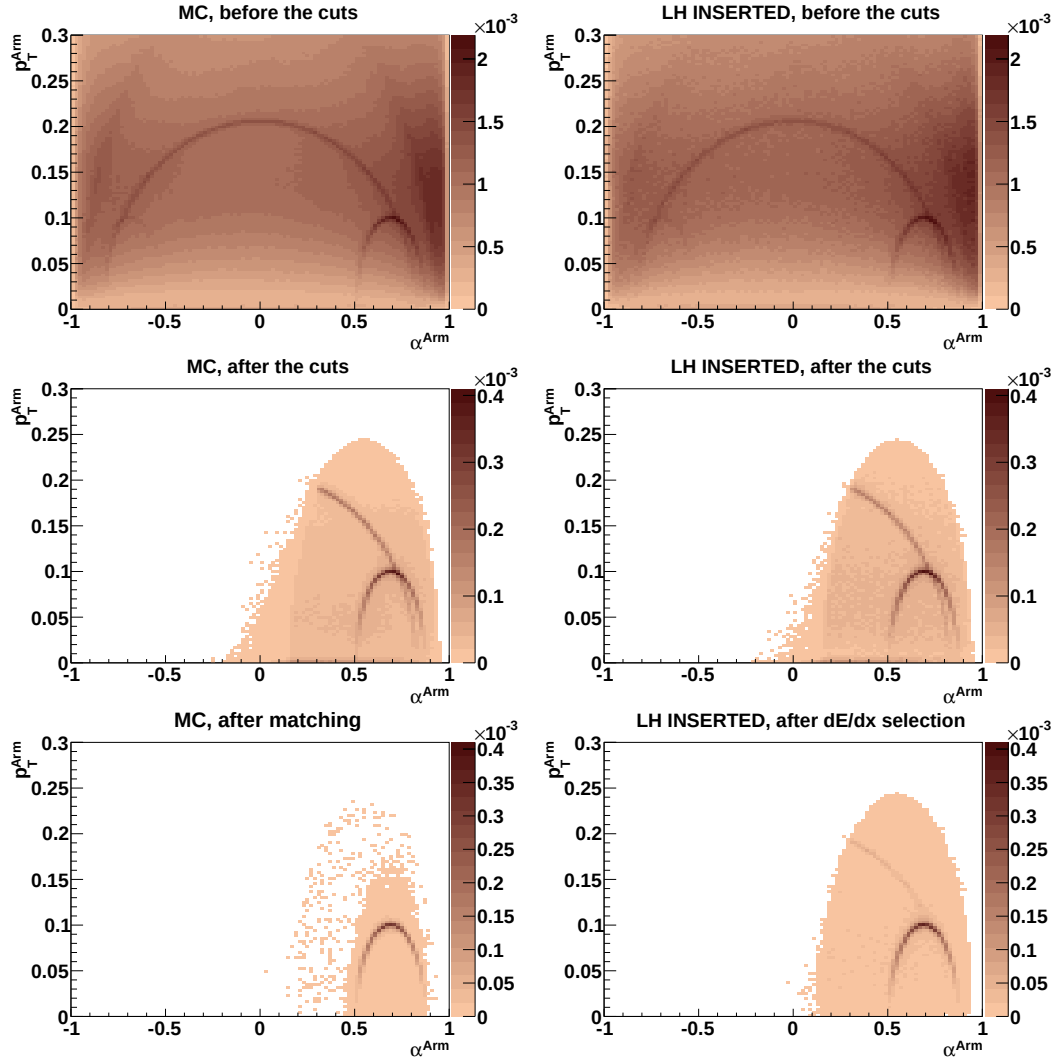

Figure 5.11. Armenteros-Podolanski plot (Subsection 3.3.1). *Left:* Simulation. *Right:* Experiment. *Top:* Before the V^0 cuts. *Middle:* After all the cuts, except of dE/dx and matching. *Bottom:* After all the cuts including matching for the MC simulation and dE/dx for experimental data. Matching discards the background from the K^0_S decay totally, while dE/dx reduces the background significantly, but it does not help to reduce it totally.

5.5 Fitting and Signal Extraction

5.5.1 Binning

The analysis aims at extracting the raw number of Λ from combinatorial background found in the invariant mass distribution. The data are binned in both rapidity (y) (from -1.5 to +1, step 0.5) or Feynman-x (x_F) [68] (from -0.4 to +0.4, step 0.1),

and transverse momentum (p_T) (from 0 to +2, step 0.2) or transverse mass ($m_T - m_\Lambda$) (from 0 to +1, step 0.1) – see Figs. 5.12 and 5.13.

For each binning a separate analysis was done. For the definition and meaning of the kinematic variables used there, see Appendix A.

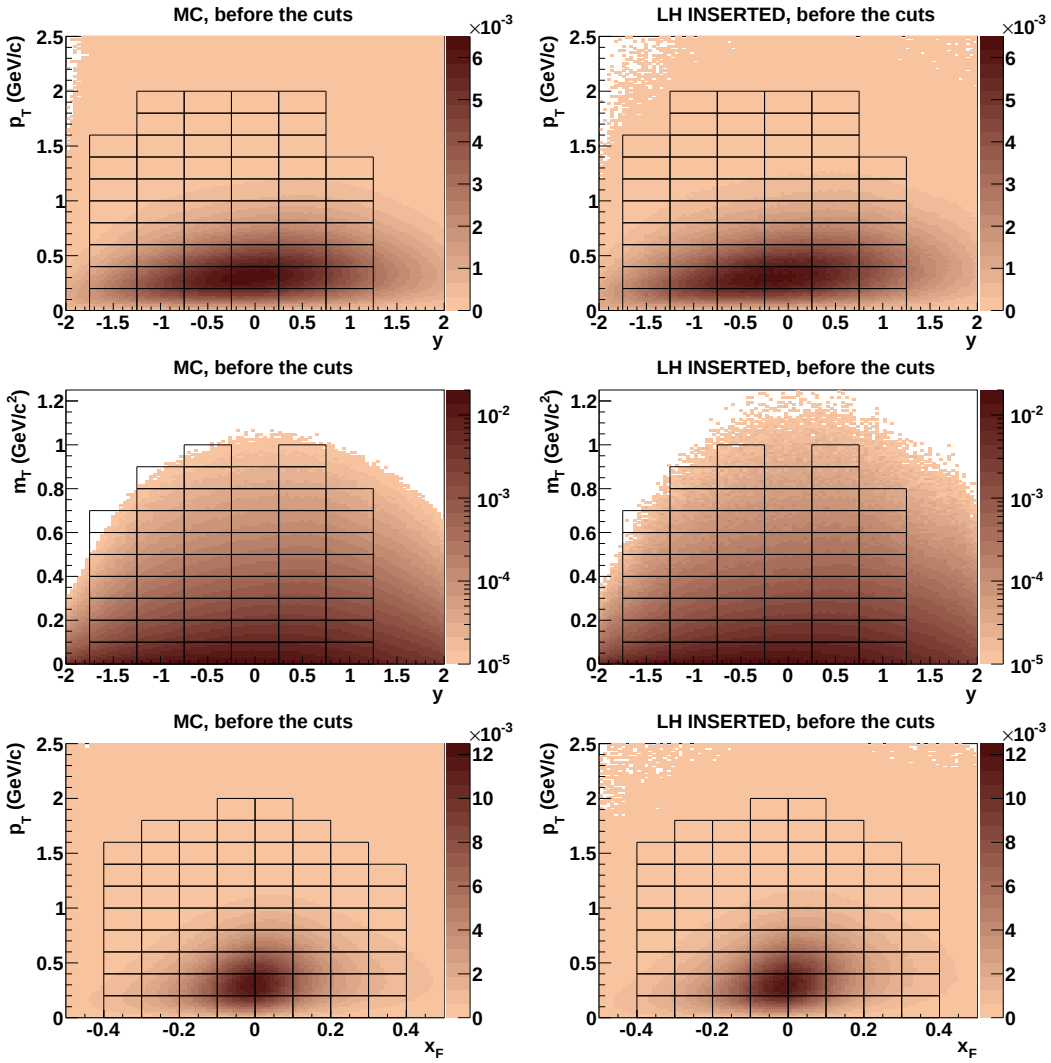

Figure 5.12. Binning for V^0-candidates before the cuts. *Left:* Simulation. *Right:* Experimental data. *Top:* Binning in rapidity y and transverse momentum p_T. *Middle:* Binning in rapidity y and transverse mass $m_T - m_\Lambda$. *Bottom:* Binning in Feynman-x x_F and transverse momentum p_T.

5.5.2 Fitting

A basis for the signal extraction are the invariant mass distributions of Λ hyperon. The way how it is calculated was presented in Subsection 3.3.3.

The invariant mass histograms are prepared using those V^0-candidates that passed the cuts described in previous sections. Then, the daughter track momentum is read

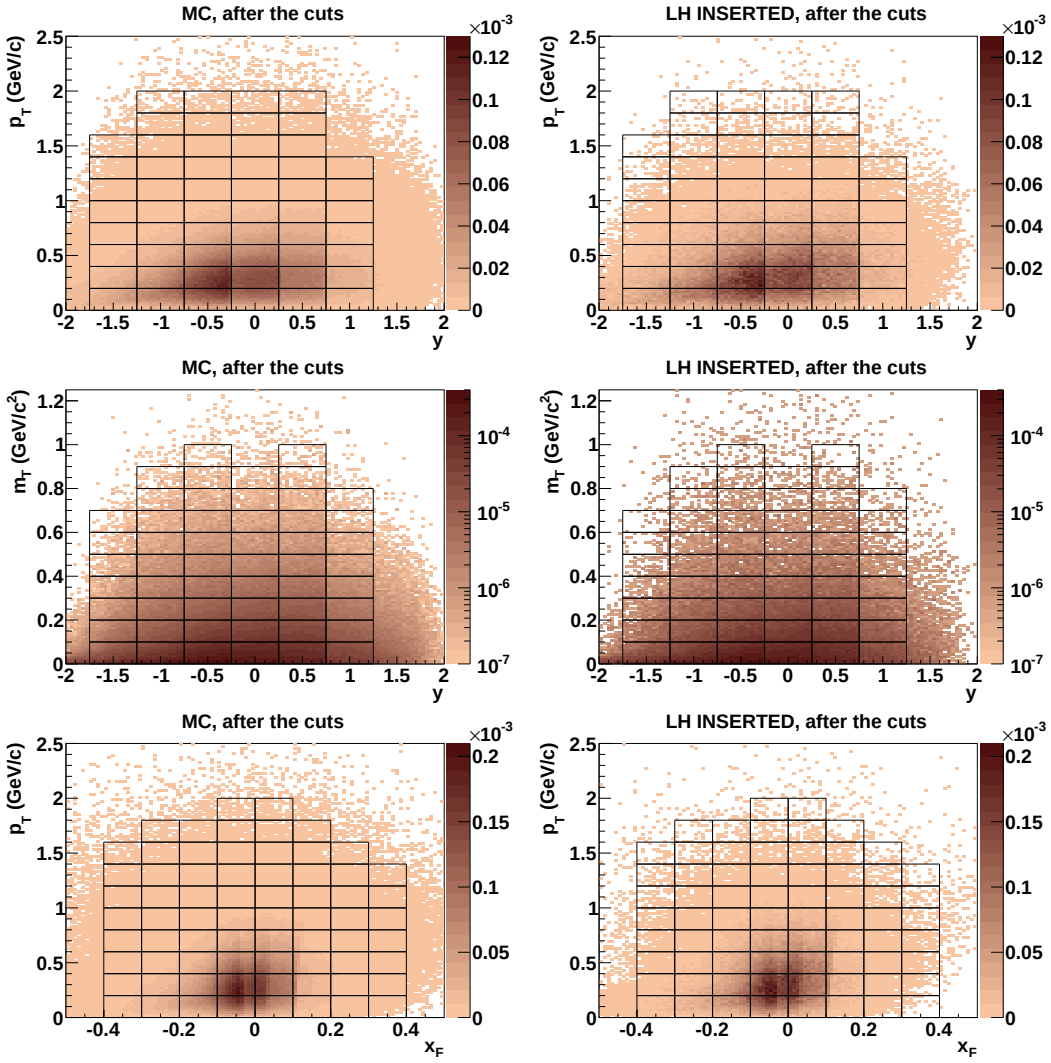

Figure 5.13. Binning for V^0-candidates after the cuts, except of dE/dx and matching. *Left:* Simulation. *Right:* Experimental data. *Top:* Binning in rapidity y and transverse momentum p_T. *Middle:* Binning in rapidity y and transverse mass $m_T - m_\Lambda$. *Bottom:* Binning in Feynman-x x_F and transverse momentum p_T.

and used for the calculation of invariant mass. As only a part of the remaining V^0-candidates are real Λ decay vertices, an assumption is made, the mass of the decay products is that of proton (for the positive charged track) and π^- (negative charge). This is the most probable charged decay channel of Λ (Section 3.2). The vertices corresponding to some other particles (e.g. many-particle decays with a part of tracks unregistered due to acceptance) or accidental coincidences (ghost V^0-vertices) build up combinatorial background. It is reduced by means of the cuts used for the analysis, but it is still of high significance.

Separate invariant mass histograms are prepared for each bin in (k, l), where k stands for centre-of-mass rapidity y or Feynman-x x_F, and l is either transverse

momentum p_T, or transverse mass m_T.

In order to separate Λ from the combinatorial background, a fitting procedure is applied. Each invariant mass histogram is fitted to the function (F) defined as a sum of background (U) and signal (S) function, where signal stands for the reconstructed Λ decays:

$$F(m) = S(m) + U(m). \tag{5.1}$$

As the shape of background depends strongly on the region of the phase-space, and the data are analysed in a wide range of k and l, the background has to be described by a function, which is flexible enough to fit to the changing shape. This is fulfilled by a Chebyshev polynomial of 2^{nd} order.

Λ peak is found to be shaped like the Lorentzian function. The Lorentzian function is defined as follows:

$$L(m) = A\frac{\frac{1}{2}\Gamma}{(m-m_0)^2 + \left(\frac{1}{2}\Gamma\right)^2}, \tag{5.2}$$

where A is a normalisation factor, m_0 is the mean value of invariant mass, and Γ is the FWHM of the peak. The widening of the peak is caused mainly by detector response, as the natural width of Λ decay is negligible. In the standard approach, the background is represented by a Chebyshev polynomial of 2^{nd} order. For the MC-data, where matching was applied to, the background is totally discarded and the corresponding function is equal to zero. The effects caused by a change of the background function were studied in details in Section 5.8.

A sum of Lorentzian function and the background was fitted in the range from 1.08 (1.076 for $y = 0.5$, 1.073 for $y = 1.0$) to 1.25 GeV/c^2. First of all, a pre-fit was done in order to estimate the initial parameters of the background function. For this, the region within the limits from 1.100 to 1.135 GeV/c^2 was removed from the analysis, as a significant contribution from the Λ peak was found there.

As a second step a fit with the full fitting function (Eq. (5.1)) is done. The initial values for the parameters of the background function are taken from the first step. Mean position of the Λ-peek (m_0) is fixed to the $m_\Lambda = 1.115683$ GeV/c^2, the value published by the PDG [50], and the width is set to 3 MeV. The resulting parameters are used as initial parameters for the third step, where no parameter is fixed.

This procedure has been developed to assure stability of the results, even in the case of low statistics. All the fits are prepared using MIGRAD run by ROOT 5.34/03.

An exemplatory final fit is shown in Fig. 5.14.

5.5.3 Signal Extraction

After the fitting procedure was done, the fitted background was subtracted and uncorrected number of Λ was found by adding up all the bin contents within the limits

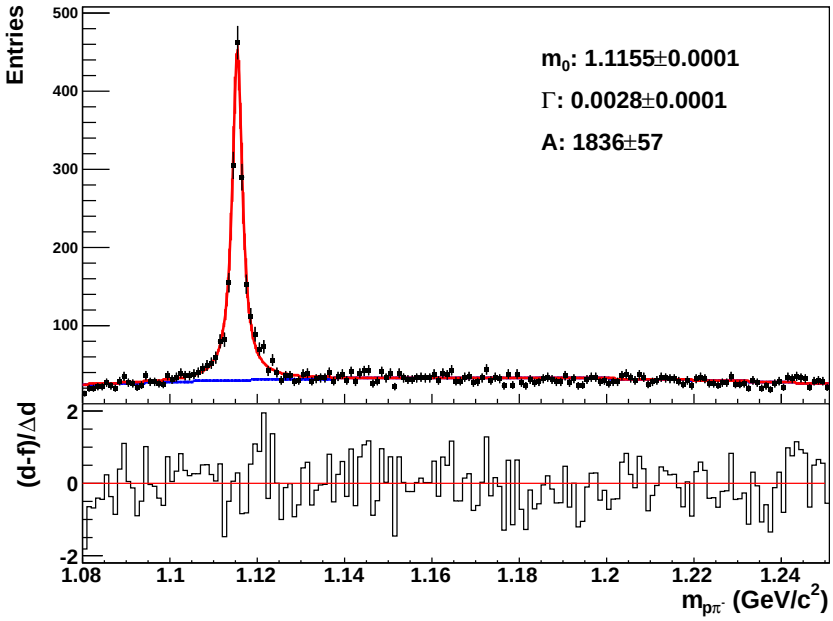

Figure 5.14. An example for a result of the standard fitting procedure. Invariant mass distribution obtained under assumption of the most prominent Λ decay channel for $y \in (-0.75, -0.25]$ and $p_T \in (0.2, 0.4]$ shown as data points. The background fit (Chebyshev polynomial of 2^{nd} order) is represented by a dashed line. The fit full signal and background function (Eq. (5.1))is plotted as a solid line. The histogram below shows the difference between the data points and the fit, normalised to statistical error of the data points.

$m_0 \pm 3\Gamma$ (Fig. 5.15). In this way the uncorrected number of Λ for the LH inserted target configuration ($n^I(k,l)$) was calculated, where k stands for rapidity y or Feynman-x x_F, and l stands for transverse momentum p_T or transverse mass $m_T - m_\Lambda$).

To obtain number of Λ hyperons produced with the hydrogen removed configuration ($n^R(k,l)$), the fit was performed for the data binned in k only, resulting in $n^R(k)$. As the inverse slope parameter T responsible for the shape of l distributions is independent of the target type in the case of interactions with nucleons [69], an assumption has been made, that l distribution of the uncorrected target removed data for a given k bin follows the shape of the uncorrected spectrum for the LH inserted configuration: $n^R(k,l) = n^R(k)\frac{n^I(k,l)}{\sum\limits_l n^I(k,l)}$. This assumption is correct as long as a strong collective flow is absent, which is the case for p+p and p+A interactions.

As for the interactions induced by protons parameter the shape of p_T distributions is independent of the target type [69] and the efficiencies are the same, we assume the p_T distribution of the uncorrected target removed data for a given y bin follows the shape of the uncorrected target inserted data: $n^R(k,l) = n^R(k)\frac{n^I(k,l)}{\sum\limits_l n^I(k,l)}$

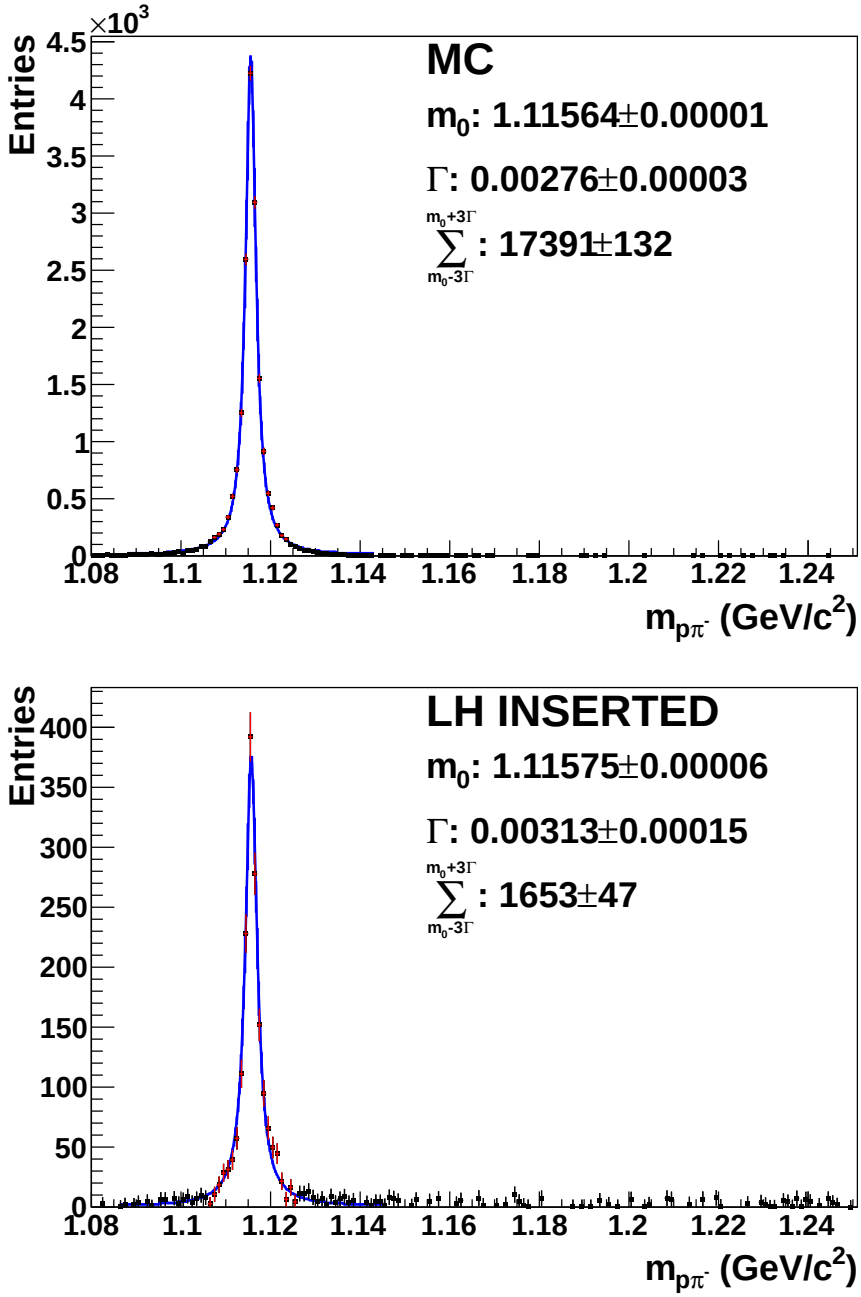

Figure 5.15. An example for invariant mass distribution calculated with the use of proton and π^- mass for $y \in (-0.25, 0.25]$ and $p_T \in (0.2, 0.4]$ after the background subtraction. The simulated data (*left*) are well reflecting the structure of the experimental data (*right*), only the simulated width of Λ-peak is higher. The sum of bin contents within the range $m_0 \pm 3\Gamma$ is calculated and shown in the picture. The bins used for the calculation are shown in red.

5.6 Corrections

Three different correction procedures were performed in order to take into account all the most important factors, that influence the final results.

5.6.1 Interactions Outside of the LH-Chamber of the Target

In order to subtract the contribution to the Λ-production from the interactions with material outside of LH-volume of the target, a number of runs with the LH-removed configuration of the target were acquired following a regular pattern. Such runs were started each 8 hours and the number of events collected during them is approximately equal to 10% of the total statistics collected with the target inserted.

In order to normalise the target removed data to the full target statistics, the distribution of z-position of the main interaction vertex was analysed. As the only expected difference in the shape and number of interactions should be visible only in the region near to the target, we assume that the distributions should be identical for the region between 1 m and 2.8 m downstream of the target. For the vertices more downstream the statistics is very small. This way we obtain a normalisation factor [70]:

$$B = \frac{N^I_{far\ z}}{N^R_{far\ z}}, \tag{5.3}$$

which is defined as a ratio of the events within the aforementioned range for the LH-inserted to the LH-removed (Fig. 5.16). The value was found to be $B = 3.9265$.

5.6.2 MC-Correction

In addition to that, a MC correction factor for efficiency was calculated. For that purpose a total of $19\,961 \times 10^3$ ($15\,607 \times 10^3$ after application of the event cuts) inelastic events were generated using the EPOS model [66], and transported using Geant3. Then, response of the detectors was simulated and reconstruction of the data was performed using the same reconstruction chain as for the experimental data. The correction on efficiency makes possible to correct the Λ-multiplicities for geometric acceptance, detector effects, reconstruction efficiency, cuts, branching, and feed-down effects. It takes into account the loss in number of the MC-generated Λ particles due to transportation and reconstruction, as well as the loss in the number of inelastic events, caused by an application of the event cuts. The correction is independent of the model used for the particle generation, except of feed-down correction. The uncertainty due to feed-down has been taken into account in the calculation of the systematic uncertainty (Subsection 5.8.4).

$$E_{_{MC}}(k,l) = \frac{n^{acc}_{MC}(k,l)}{N^{acc}_{MC}} \Bigg/ \frac{n^{gen}_{MC}(k,l)}{N^{gen}_{MC}}, \tag{5.4}$$

where

- $n_{MC}^{acc}(k,l)$ is the number of Λ-particles (including Σ^0) in a given (k,l) bin after transportation and reconstruction, following the same procedure as in the case of experimental data,
- $n_{MC}^{gen}(k,l)$ - all Λ generated in the primary interactions, regardless of the decay channel; Λ produced in Σ^0 decays are used as well,
- N_{MC}^{gen} - the number of inelastic interactions (events) generated by the model,
- N_{MC}^{acc} - the number of MC inelastic interactions (events) accepted (after the event cuts),
- $k = y$ or x_F, and $l = p_T$ or m_T (dependent on binning).

Statistical error of the correction factor is calculated using the following approach: The correction factor $(1/E_{MC})$ consists of two parts:

$$\begin{aligned} \frac{1}{E_{MC}}(k,l) &= \frac{n_{MC}^{gen}(k,l)}{N_{MC}^{gen}} \Big/ \frac{n_{MC}^{acc}(k,l)}{N_{MC}^{acc}} \\ &= \frac{N_{MC}^{acc}}{N_{MC}^{gen}} \Big/ \frac{n_{MC}^{acc}(k,l)}{n_{MC}^{gen}(k,l)} = \frac{\alpha}{\beta(k,l)}, \end{aligned} \tag{5.5}$$

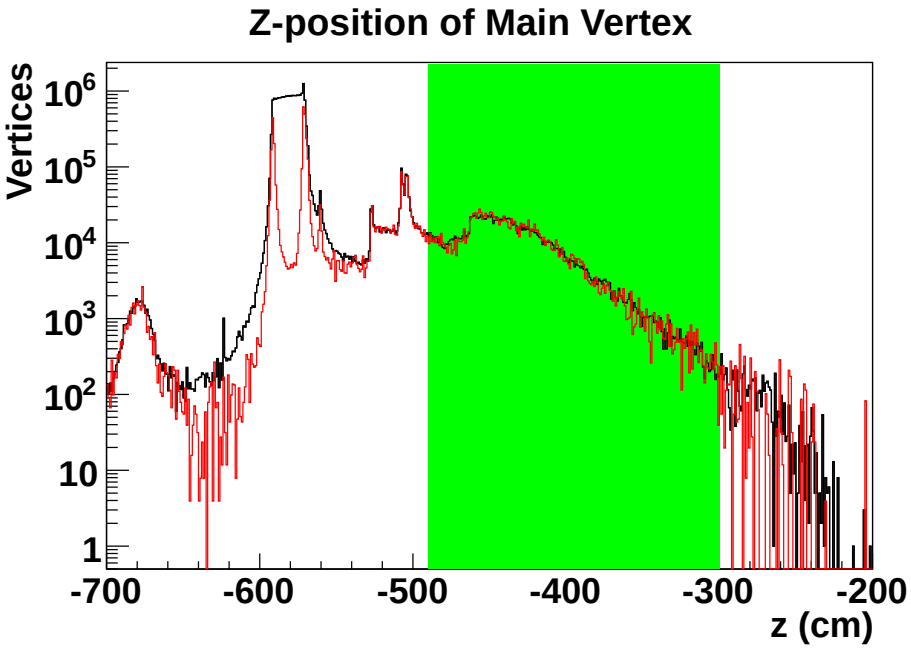

Figure 5.16. Z-component of the main vertex position. Calculation of the correction factor B was done within the range highlighted in green. Black line corresponds to the interactions with the LH inserted configuration of the target, while the red line corresponds to the LH removed configuration multiplied by B (Eq. (5.3)).

where α describes the loss of inelastic events due to the event selection, and β takes into account the loss of extracted Λ particles due to the V^0-cuts, efficiency, and the other aforementioned effects.

The error of α is calculated used binomial distribution, while the part invoking the fitting procedure (β) takes into account error of the fit:

$$\Delta\alpha = \sqrt{\frac{\alpha(1-\alpha)}{N_{MC}^{gen}}}, \tag{5.6}$$

$$\Delta\beta(k,l) = \sqrt{\left(\frac{\Delta n_{MC}^{acc}(k,l)}{n_{MC}^{gen}(k,l)}\right)^2 + \left(\frac{n_{MC}^{acc}(k,l)\Delta n_{MC}^{gen}(k,l)}{(n_{MC}^{gen}(k,l))^2}\right)^2}, \tag{5.7}$$

where $\Delta n_{MC}^{acc}(k,l)$ is the uncertainty of the fit from MIGRAD, and $\Delta n_{MC}^{gen}(k,l) = \sqrt{n_{MC}^{gen}(k,l)}$ the total statistical error of $1/E_{MC}$ is calculated using total differential by the equation below:

$$\Delta\left(\frac{1}{E_{MC}}\right) = \sqrt{\left(\frac{\Delta\beta}{\alpha}\right)^2 + \left(-\frac{\beta\Delta\alpha}{\alpha^2}\right)^2}. \tag{5.8}$$

The MC-efficiencies are presented in Appendix C in Sections C.2-C.6.

5.6.3 Losses Due to dE/dx Cut

In addition to that, a correction for the number of Λ loss due to dE/dx cut was performed, since it was not possible to perform the same procedure in the MC-simulation. The cut extracts only these V^0 vertices, for which specific energy loss differs from the Bethe-Bloch parametrisation for both proton and pion by not more than 3σ. Thus, the number of uncorrected Λ had to be increased by 0.542% by applying a constant correction factor $\left(\frac{1}{E_{\frac{dE}{dx}}} = 1.00542\right)$. This equals to $1/\epsilon^2$, where $\epsilon = 0.99730$ is the probability of finding a particle to lie within $\pm 3\sigma$ of the normal distribution.

5.7 Yields

In order to obtain spectra of Λ-baryons the equation for the corrected multiplicity of Λ per inelastic event was used for each bin with the centre in (k,l):

$$\frac{n}{N}(k,l) = \frac{1}{E_{\frac{dE}{dx}}E_{MC}(k,l)}\frac{n^I(k,l) - Bn^R(k,l)}{N^I - BN^R}, \tag{5.9}$$

where

- $\frac{n}{N}(k,l)$ - final estimation of the true value of Λ-multiplicity per event for a bin centred in (k,l),

- $n^{I/R}(k,l)$ - uncorrected number of Λ-particles per bin for the LH inserted/removed configuration of the target,
- $N^{I/R}$ - number of events left after the event cuts for the LH inserted/removed configuration of the target,
- $E_{\frac{dE}{dx}}$, E_{MC}, and B - correction factors; detailed description in Section 5.6.

This equation is applicable independent of the binning used.

Statistical error of this observable is calculated given the equation for the statistical error of $1/E_{MC}$ (5.8) and assuming $\Delta B = 0$ and $\Delta E_{dE/dx} = 0$, which result in the following equation:

$$\Delta\left(\frac{n}{N}\right) = \tag{5.10}$$

$$\sqrt{\left(\Delta\left(\frac{1}{E_{MC}}\right)\frac{n^I(k,l)-Bn^R(k,l)}{N^I-BN^R}\right)^2+\left(\frac{1}{E_{MC}}\frac{\sqrt{(\Delta n^I(k,l))^2+(B\Delta n^R(k,l))^2}}{N^I-BN^R}\right)^2+\left(\frac{1}{E_{MC}}\frac{(n^I(k,l)-Bn^R(k,l))\sqrt{N^I+B^2N^R}}{(N^I-BN^R)^2}\right)^2},$$

where $\Delta(1/E_{MC})$ is calculated via Eq. (5.8), $\Delta n^{I/R}$ come from respective fits and $\Delta N^{I/R} = \sqrt{N^{I/R}}$.

Then, the double-differential spectra are computed via

$$\frac{d^2n}{dkdl} = \frac{1}{\Delta k \Delta l}\frac{n}{N}(k,l)\,, \tag{5.11}$$

where Δk and Δl stand for the bin width.

Yields for the single-differential distributions $\frac{dn}{dk}$ for given k are calculated by adding together the measured data points from the double-differential spectrum $dn/dk = \sum_l \frac{d^2n}{dkdl}$, and multiplying them by bin width Δl. For the acceptance of the detector does not cover 4π, an extrapolation to the full phase-space with the use of a continuous function $u(l)$ fitted to the data points was done.

We expect the data exhibits $m_T = \sqrt{p_T^2 + m_\Lambda^2}$ scaling, given by the thermal ansatz

$$\frac{d^2n}{dkp_Tdp_T} = \frac{d^2n}{dkm_Tdm_T} = Ae^{-\frac{m_T}{T}}, \tag{5.12}$$

where the scaling factor is described by the inverse slope parameter T, attributed to the temperature of a system during an adiabatic expansion [71], and normalisation factor A is characteristic to the particle species.

Thus, the extrapolation is done by fitting the exponential function to the data. For the binning in (k, p_T), the function reads as follows:

$$u(p_T) = \frac{Sp_T}{T^2 + m_\Lambda T}\ \exp\left(-\frac{\sqrt{p_T^2+m_\Lambda^2}-m_\Lambda}{T}\right), \tag{5.13}$$

which can be easily obtained from Eq. (5.12) by defining $S = \int_0^{+\infty}\frac{d^2n}{dkdp_T}$. For derivation see Appendix B. The results calculated with this form of thermal ansatz were slightly more stable, and the parameter S was useful for diagnostics.

For binning in m_T the function is directly copied from the Eq. (5.12).

$$u(m_T) = Am_T e^{-\frac{m_T}{T}}, \tag{5.14}$$

and for the transverse mass can not be lower than the proper mass of a particle, it is used in dependence on $m_T - m_\Lambda$.

Mean transverse mass $\langle m_T \rangle$ was calculated using the m_T distribution found by fitting $u(m_T)$ from the Eq. (5.14) to the data:

$$\langle m_T \rangle = \frac{\int_0^{+\infty} (m_T - m_\Lambda) u(m_T - m_\Lambda) dm_T}{\int_0^{+\infty} u(m_T - m_\Lambda) dm_T}. \tag{5.15}$$

The invariant spectra binned in x_F and p_T are calculated following the equation [72]:

$$\begin{aligned} f_n(x_F, p_T) &= \frac{d^3n}{d\mathbf{p}/E} = \frac{1}{\pi} \frac{d^2n}{dy dp_T^2} \\ &= \frac{2E^*}{\pi\sqrt{s}} \frac{d^2n}{dx_F dp_T^2} = \frac{1}{\pi\sqrt{s}} \frac{E^*}{p_T} \frac{d^2n}{dx_F dp_T}. \end{aligned} \tag{5.16}$$

For the purpose of preparing the invariant spectra, each entry to the invariant mass histogram was scaled by E^*/p_T before the standard procedure was performed, and a separate analysis was done.

Single-differential invariant yield $F_n(x_F)$ is defined as a result of integration of Eq. (5.16) with respect to p_T^2:

$$F_n(x_F) = \frac{2}{\pi\sqrt{s}} \int E^* \frac{d^2n}{dx_F dp_T} dp_T. \tag{5.17}$$

For calculation of $F(x_F)$ the entries in the invariant mass histograms were scaled by E^* each and a separate analysis followed. For the extrapolation, Eq. (5.13) was used.

In total 5 independent separate analyses were performed. One to obtain $d^2n/(dydp_T)$ spectra as well as the inverse slope parameter, and dn/dy distribution. Another one is used to calculate $d^2n/(dydm_T)$ spectra and the mean transverse mass $\langle m_T \rangle$. One analysis is performed to find $d^2n/(dx_F dp_T)$ and dn/dx_F. Additional 2 analyses are made to obtain invariant yields f_n and F_n, for 2 different scaling factors had to be applied on the stage of the preparation of invariant mass histograms.

5.8 Systematic Uncertainties

The systematic uncertainties are calculated taking into account 4 main sources of the error. Each source contains a number of modifications to the standard procedure concerning one special subject of analysis. Deviation from the standard procedure is calculated for each modification. As the modifications within one source of uncertainty are dependent on each other, the maximal positive and negative deviation

from the standard procedure is found among all the modifications for each bin and source separately. Then, the positive/negative systematic uncertainties are calculated separately by adding in quadrature the positive/negative contribution from each source.

The systematic uncertainties are presented in the plots as rectangles in background of the NA61/SHINE data points.

5.8.1 Extraction Procedure

Uncertainty due to the extraction procedure is found by performing modifications to the standard extraction procedure:

- The function describing shape of the background was changed from a Chebyshev polynomial of 2^{nd} order for a Chebyshev polynomial of $3rd$ order. The average effect of this modification is 3.2%. A change for a polynomial of 2^{nd} order was also made (average effect 1.7%).
- The range within which the raw number of Λ particles is added up was changed from 3Γ for 2.5Γ (average effect 1.8%), and for 3.5Γ (average effect 1.2%).
- The lower limit of the fitting range was increased by 3 MeV from 1.08 (1.076 for $y = 0.5$, 1.073 for $y = 1.0$). Average effect is 2.6%.
- Initial Γ of the fitting function was changed by $\pm 8\%$ (average effect 1.2%) and the initial position by ± 0.3 MeV (average effect 0.7%).

5.8.2 Event and Quality Cuts

Effects of the event and quality cuts modification was checked for by performing analysis with following cuts changed compared to the values presented in Sections 5.3 and 5.4.

- The cut on z-position of the main interaction vertex changed from ± 40 cm from the centre of the target to ± 30 cm, and to ± 50 cm. Average effect 1.6%.
- The window where no off-time beam particle occurs was widened from 1μs to 1.5μs. Average effect 1.9%.
- The distance in xy-coordinates between the main interaction vertex and an intersection of the backward-extrapolated V^0-track with the target plane was reduced by 2: (horizontal half-axe of the ellipse was made 1 cm long instead of 2 cm, and vertical half-axe 0.5 cm long instead of 1 cm). Average effect 2.4%.
- Minimal number of charge clusters in one VTPC was modified by ± 3 data points compared to the standard value of 15. Average effect 3.3%.
- The limits for the cut on $\cos\phi$ was changed for $|\cos\phi| < 0.975$ for $y < -0.25$, $|\cos\phi| < 0.95$ for $y \in [-0.25, 0.75)$, $|\cos\phi| < 0.85$ (higher rapidities). The cut

was also made more strict by applying the values 0.925, 0.85, 0.75 for respective rapidity ranges. Average effect 3.3%.

- In addition to the standard set of cuts, a cut on $\cos\theta$, where θ is the polar angle between the direction of the Λ momentum and the momentum of the positively-charged decay product in the centre-of-mass system, was checked for its influence on the results. The cut applied is $\cos\theta > -0.8$ and $\cos\theta < 0.95$. This cut is to assure, the geometrical distribution of the decay products is is flat. Although there are some small uneven regions in the distribution of the V^0-candidates, they are mainly due to the background, that is subtracted on the further stage of the analysis. The uneven regions are removed using this cut. Average effect 4.9%.
- The cut on Δz - distance between the decay and the primary interaction vertex was modified by $\pm 25\%$. Average effect 3.2%.
- The dE/dx cut was modified by taking into account the particles, for which the dE/dx is in $\pm 2.8\sigma$, and in $\pm 3.2\sigma$ instead of the standard cut of 3σ (to check the systematic effects of dE/dx calibration, which are not included in the dE/dx correction, discussed in Subsection 5.6.3). Average effect 2.8%.
- Matching procedure was turned off for MC. Average effect 5.8%.

5.8.3 Normalisation of the LH-Removed Data

For the normalisation factor for the LH removed configuration of the target B (Eq. (5.3)) was calculated using an arbitrarily chosen range from 1 m to 2.8 m upstream of the target, the procedure was taken in the scope of the systematic uncertainty calculation.

In order to find the systematic uncertainty of B, the region where this parameter is calculated was divided within the range from 0.8 m to 3.8 m downstream to the target into some subsets. For each combination of the lower limit (ranging from 0.8 to 1.8 m from the target, step 0.1 m) and upper limit in z (from 2.8 m to 3.8 from the target, step 0.1 m) the B-factor was calculated as the number of main interaction vertices, which z-coordinate is found within these limits. The smallest and the highest value obtained using this approach was used for the estimation of the systematic uncertainty. The normalisation factor used for the standard analysis equals to 3.9265, while the minimal one 3.84572, and the maximal one 4.06721. The difference between them is about 6%, but for the normalisation factor is used mainly to subtract background from the interactions with the material outside of the target chamber, the impact on the final yields in of the order of one thousandth.

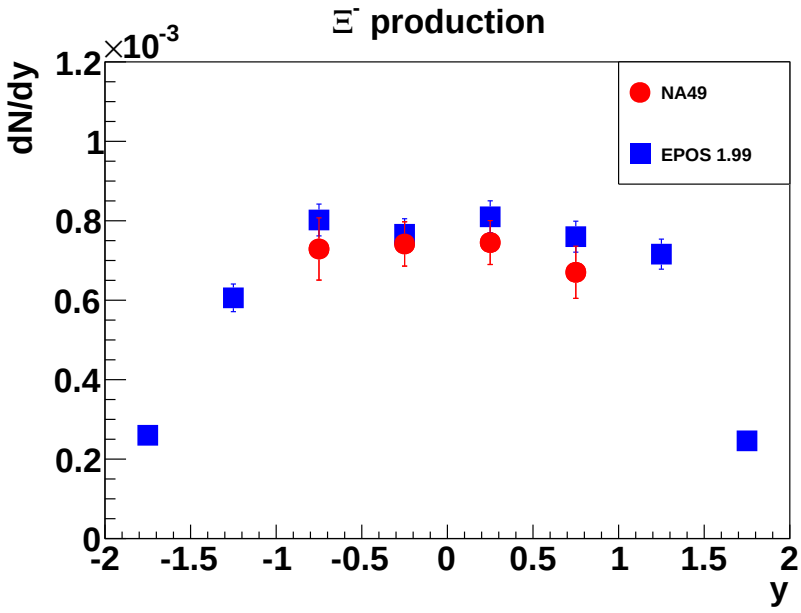

Figure 5.17. Comparison of Ξ^- rapidity distribution for the model used for the feed-down corrections (EPOS) and the experimental results from NA49 [73].

5.8.4 Feed-Down

For estimation of the uncertainty due to feed-down correction the experimental data on the production of Ξ^- from the NA49 experiment was used [73]. This data was compared to the EPOS [66] predictions (Fig. 5.17). Due to lack of experimental data on Ξ^0 production for the analysed reaction, the same relative difference between data and the model was assumed, as for Ξ^-. This estimation is constant for all the analysis and amounts to 0.8%.

The differential spectrum is calculated from Eq. (5.11) using Eq. (5.9). Let us denote the uncorrected part of Eq. (5.9) as

$$\zeta_{exp} = \frac{n(k,l)^I - Bn(k,l)^R}{N^I - BN^R}, \tag{5.18}$$

so that

$$\frac{n}{N} = \frac{1}{E_{\frac{dE}{dx}} E_{MC}} \zeta_{exp}, \tag{5.19}$$

where index *exper* denotes experimental part of the equation.

The correction factor E_{MC} is defined in Eq. (5.4). It can be rewritten as follows:

$$\frac{1}{E_{MC}} = \frac{\zeta_{MC}^{gen}}{\zeta_{MC}^{acc}}, \tag{5.20}$$

where

$$\zeta_{MC}^{gen} = \frac{n_{MC}^{gen}}{N_{MC}^{gen}}, \tag{5.21}$$

and

$$\zeta_{MC}^{acc} = \frac{n_{MC}^{acc}}{N_{MC}^{acc}}. \tag{5.22}$$

Then n/N can be rewritten as:

$$\frac{n}{N} = \frac{1}{E_{\frac{dE}{dx}} E_{MC}} \zeta_{MC}^{gen} \frac{\zeta_{exp}}{\zeta_{MC}^{acc}}. \tag{5.23}$$

This holds only in the case the feed-down correction is the same in case of both MC and experimental data. It might be rewritten by multiplying the numerator and the denominator by the feed-down correction factor c^{Ξ} due to Ξ^- and Ξ^0.

$$\frac{n}{N} = \frac{1}{E_{\frac{dE}{dx}}} \zeta_{MC}^{gen} \frac{\zeta_{exp} c_{MC}^{\Xi}}{\zeta_{MC}^{acc} c_{MC}^{\Xi}}. \tag{5.24}$$

If the correction factor from the model does not reproduce the experimental yields, the correction factor for experimental data c_{exp}^{Ξ} is not equal to the MC-factor c_{MC}^{Ξ}. In that case:

$$\frac{n}{N} = \frac{1}{E_{\frac{dE}{dx}}} \zeta_{MC}^{gen} \frac{\zeta_{exp} c_{exp}^{\Xi}}{\zeta_{MC}^{acc} c_{MC}^{\Xi}}. \tag{5.25}$$

Correction for the data of type t =MC or t =exper is the following

$$c_t^{\Xi} = \frac{\langle \Lambda \rangle_{MC}}{\langle \Lambda \rangle_{MC} + \langle \Xi \rangle_t}, \tag{5.26}$$

where

$$\langle \Xi \rangle_t = \langle \Xi^- \rangle_t + \langle \Xi^0 \rangle_t. \tag{5.27}$$

Bearing in mind the correction might be done only using the charged Ξ^-, as there are no experimental data for Ξ^0 production in p+p interactions at 158 GeV/c, and that all the mean multiplicities are calculated for the NA49 acceptance, one has to assume the same relative difference between model and the experimental data for Ξ^0 as it is the case for Ξ^-:

$$\langle \Xi^0 \rangle_{exp} = \langle \Xi^0 \rangle_{MC} \frac{\langle \Xi^- \rangle_{exp}}{\langle \Xi^- \rangle_{MC}}. \tag{5.28}$$

This method give an estimation of systematic uncertainty due to feed-down as:

$$\frac{c_{\Xi}^{exp}}{c_{\Xi}^{MC}} = \left(\frac{\langle \Lambda \rangle_{MC}}{\langle \Lambda \rangle_{MC} + \langle \Xi^- \rangle_{exp} + \langle \Xi^0 \rangle_{MC} \frac{\langle \Xi^- \rangle_{exp}}{\langle \Xi^- \rangle_{MC}}} \right) \Bigg/ \left(\frac{\langle \Lambda \rangle_{MC}}{\langle \Lambda \rangle_{MC} + \langle \Xi^- \rangle_{MC} + \langle \Xi^0 \rangle_{MC}} \right). \tag{5.29}$$

The value calculated using this modification gives 0.8% difference compared to the standard analysis procedure.

Chapter 6

Results and Discussion

6.1 Spectra of Λ

Double-differential spectra calculated with the use of Eq. (5.11) are shown in the following figures: Fig. 6.1 for $\frac{d^2n}{dydp_T}$, Fig. 6.2 for $\frac{d^2n}{dydm_T}$, Fig. 6.3 for $\frac{d^2n}{dx_F dp_T}$. Figure 6.4 shows Lorentz-invariant spectrum ($f_n(x_F, p_T)$), calculated with Eq. (5.16).

The numerical data for these plots can be found in Appendix C, in particular Tab. C.3 for $\frac{d^2n}{dydp_T}$, and Tab. C.4 for $\frac{d^2n}{dydm_T}$. The spectra dependent on x_F are divided into two tables: Tab. C.5 for $x_F < 0$ and Tab. C.6 for $x_F > 0$.

The single differential distribution $\frac{dn}{dy}$, derived from $\frac{d^2n}{dydp_T}$ via Eq. (5.12) and (5.13), is gathered in Tab. C.1. The table contains also inverse slope parameter calculated with Eq. (5.13) and mean transverse mass $\langle m_T \rangle$ given by Eq. (5.15). The single differential spectra binned in x_F are to be found in the Tab. C.2.

See Sections 6.3 and 6.4 for plots of the single-differential spectra, where they are compared to the model predictions and the experimental data. In particular $\frac{dn}{dy}$ and $\frac{dn}{dx_F}$ are to be found in Fig. 6.13, and $F(x_F) = \sigma_{inel.} F_n(x_F)$ distribution in Fig. 6.9.

For efficiencies and uncorrected yields, see 2D histograms in Appendix C.

6.2 Quality Tests

The quality of the data analysis was checked using a few methods in order to assure the conclusiveness of the results. The first method applied for the check was an analysis of particle lifetime. The cuts and the extraction procedure used for this test was the same as for the main part of the analysis (Chapter 5). The only difference to the previous analysis was the binning. The data were binned in rapidity (from -1.5 to +1.0, step 0.5) and lifetime normalised to the PDG [50] mean lifetime t/τ_{PDG} (from 0.00 to 4.75, step 0.25), therefore l in Eq. (5.11) equals to t/τ_{PDG}, where $\tau = (2.632 \pm 0.020) \times 10^{-10}$ s [50]. Lifetime was calculated using the distance r between the V^0-decay vertex and the main interaction vertex of each of the V^0-candidates

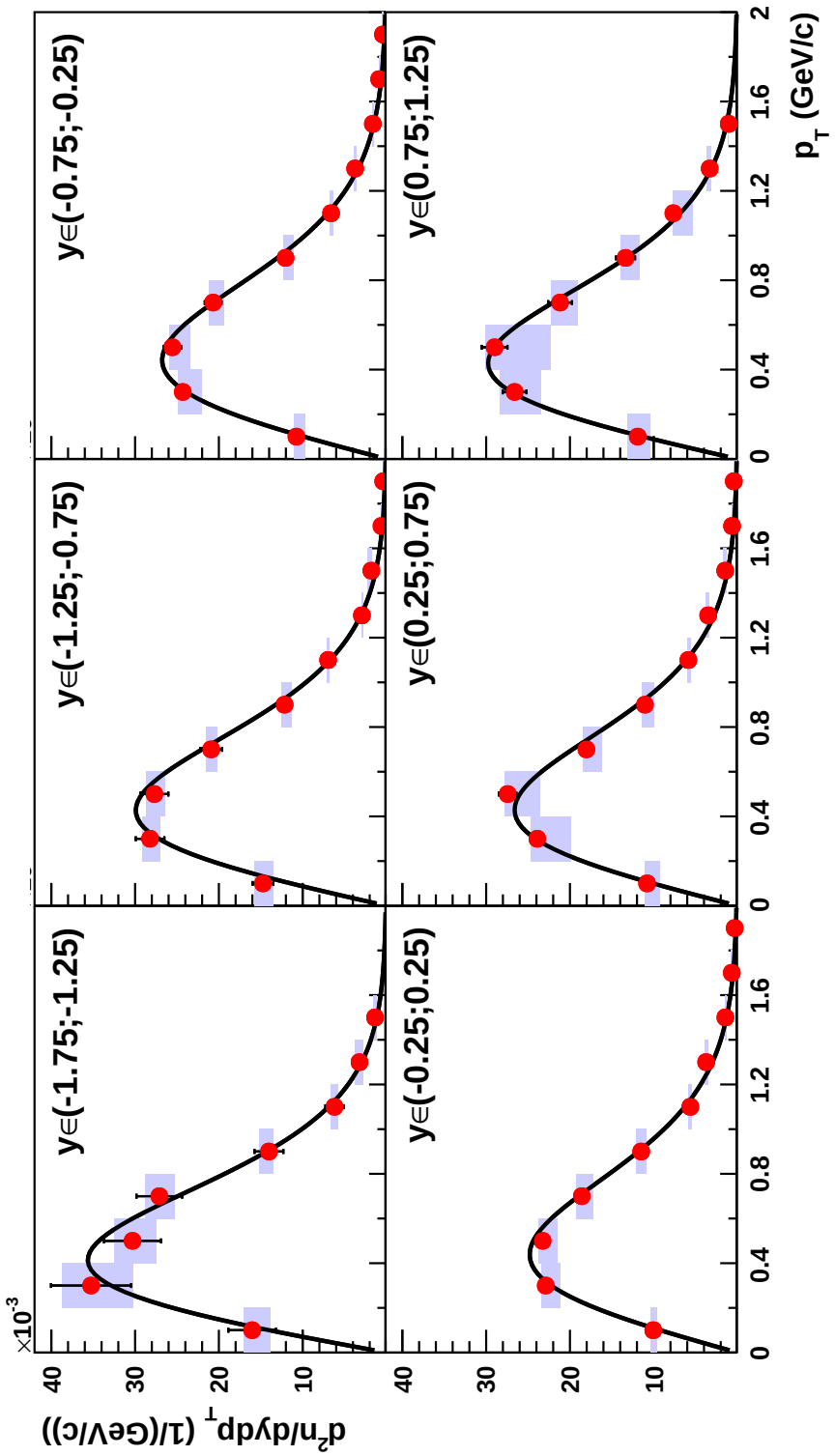

Figure 6.1. Double-differential $\frac{d^2n}{dydp_T}$ spectra for six rapidity y bins. The fitting function is given by Eq. (5.13). The numerical data are available in the Tab. C.3. Inverse slope parameter for each of the bins is contained within the Tab. C.1. The systematic uncertainties shown as rectangles in background of the data points.

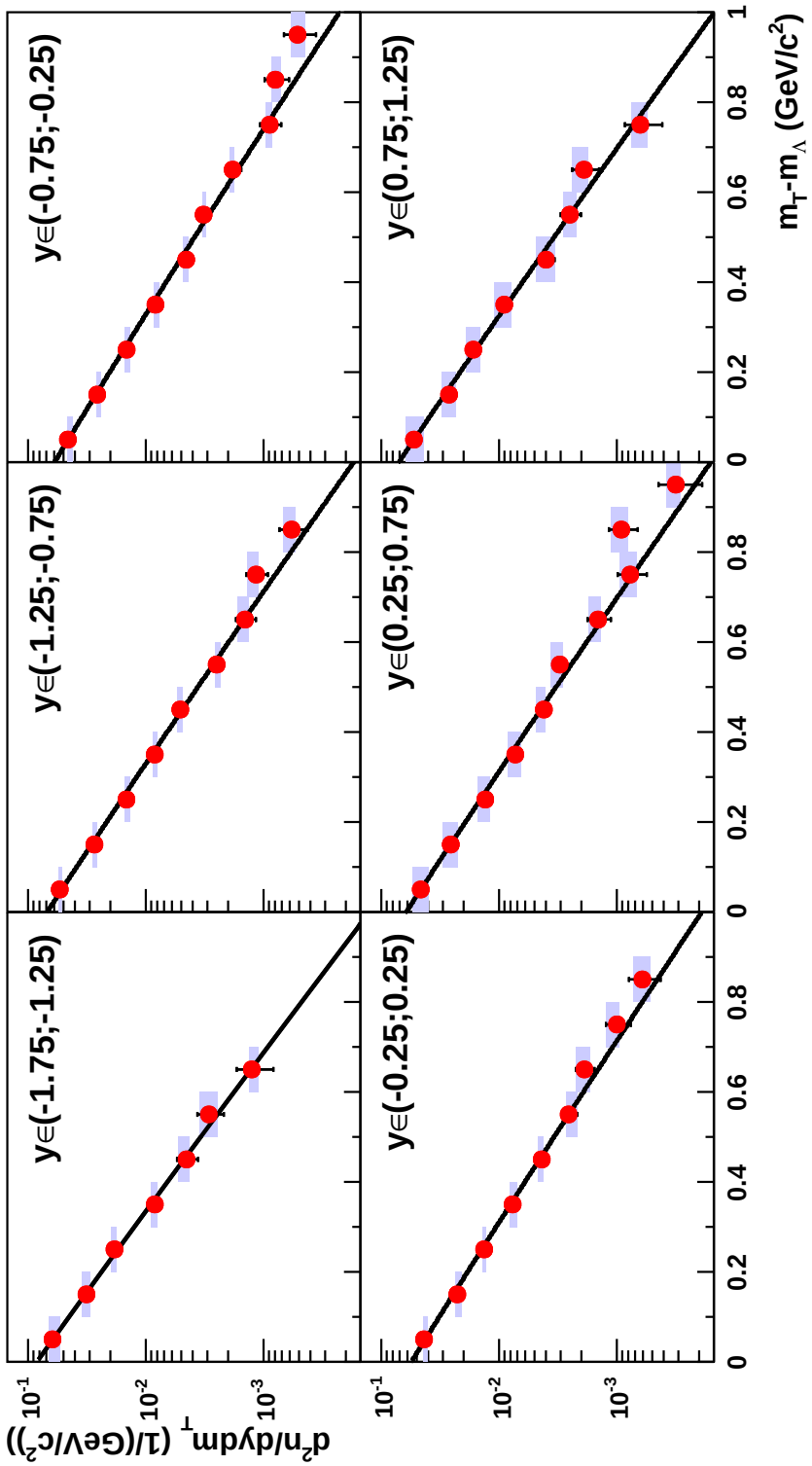

Figure 6.2. Double-differential $\frac{d^2n}{dydm_T}$ spectra for six rapidity y bins. The fitting function is given by Eq. (5.14). The numerical data are available in the Tab. C.4. Mean transverse mass $\langle m_T \rangle$ for each of the bins is shown in Tab. C.1. The systematic uncertainties shown as rectangles in background of the data points.

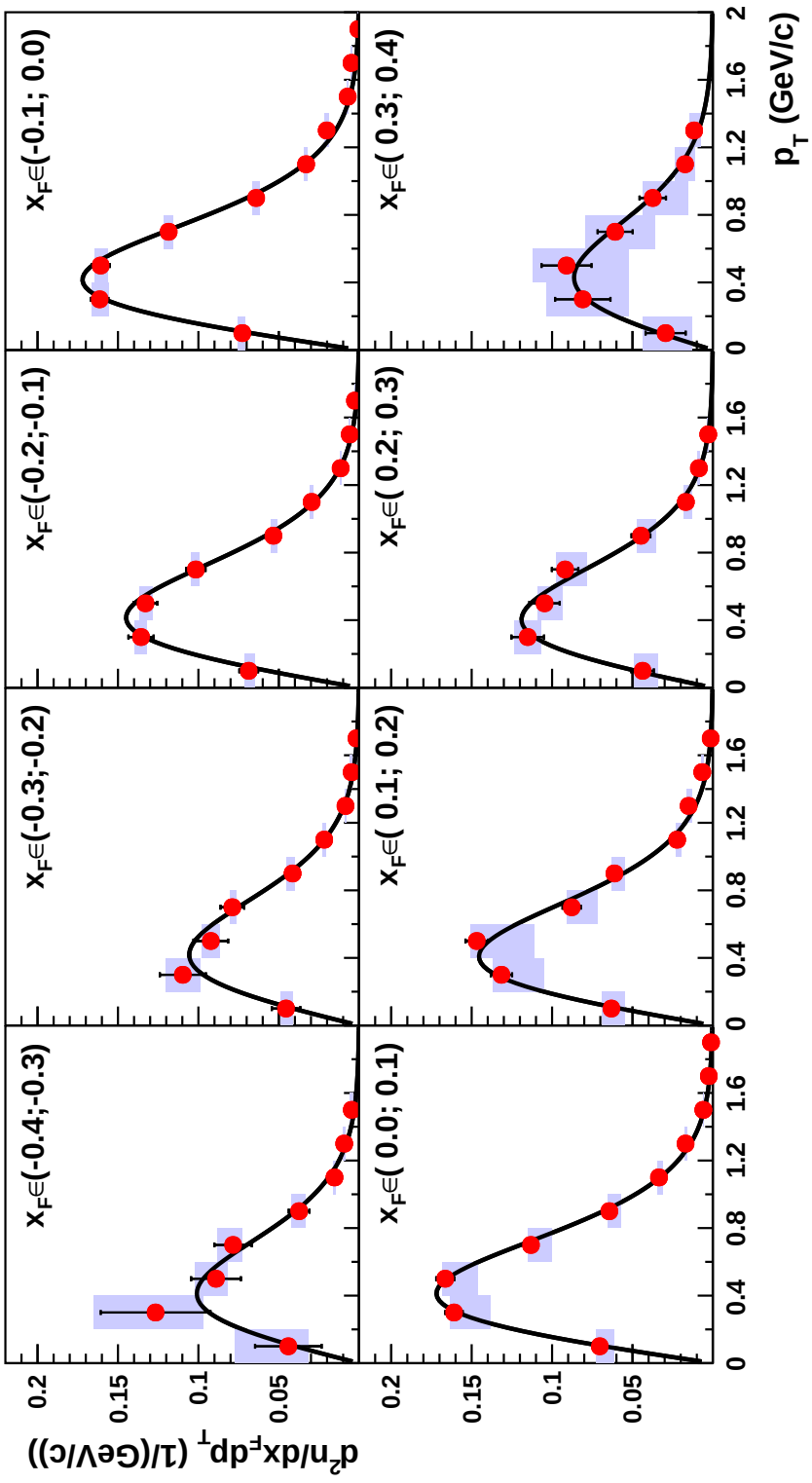

Figure 6.3. Double-differential $\frac{d^2n}{dx_F dp_T}$ spectra for eight x_F bins. The fitting function is given by Eq. (5.13). The numerical data are available in the Tab. C.5 (negative x_F) and C.6 (positive x_F). The systematic uncertainties shown as rectangles in background of the data points.

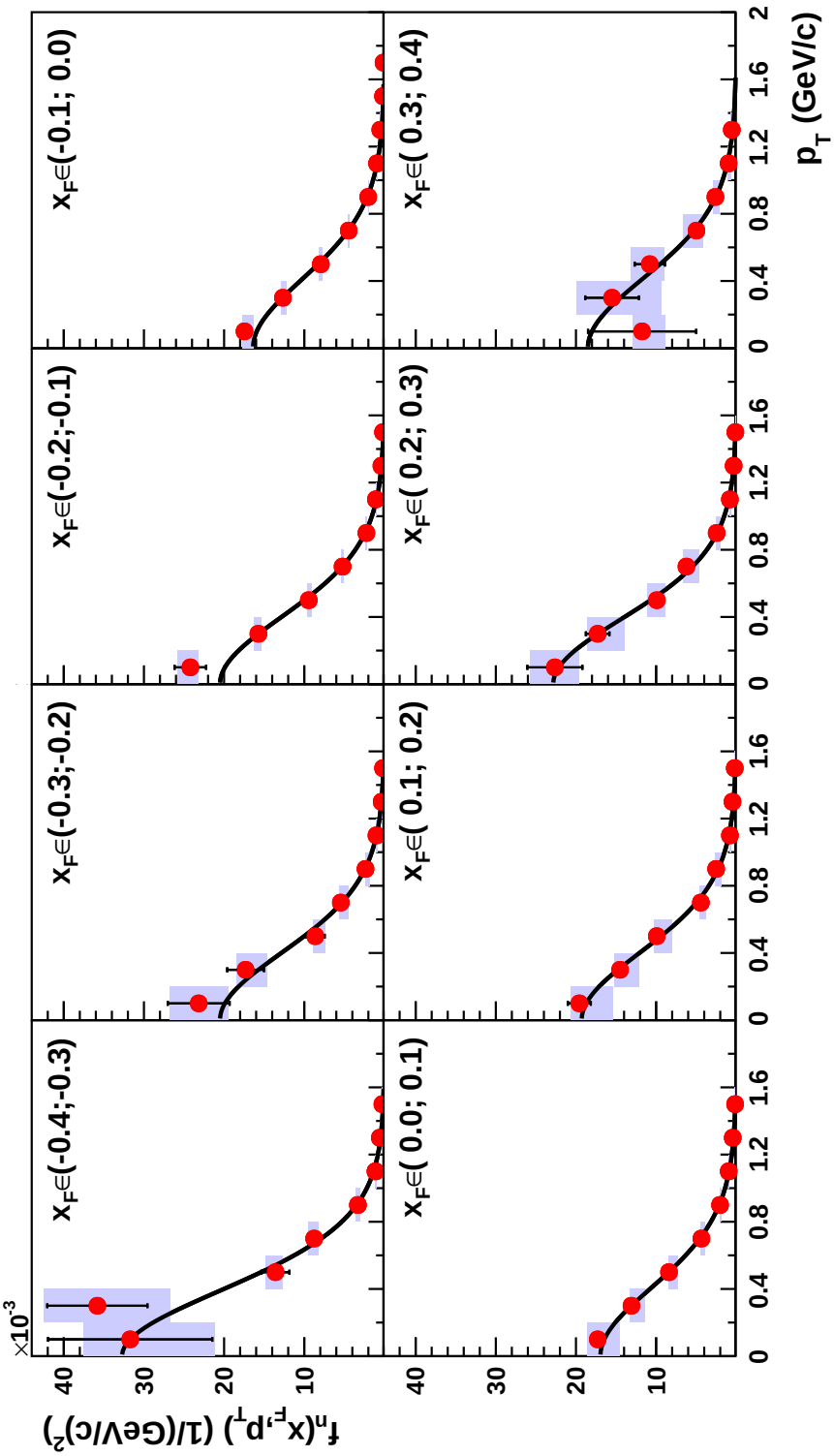

Figure 6.4. Double-differential $f_n(x_F, p_T)$ invariant spectra given by Eq. (5.16) for eight x_F bins. The fitting function is obtained from the Eq. (5.13) by multiplying the right-hand side by p_T. It is not used for any further calculations. The numerical data are available in the Tab. C.5 (negative x_F) and C.6 (positive x_F). The systematic uncertainties shown as rectangles in background of the data points.

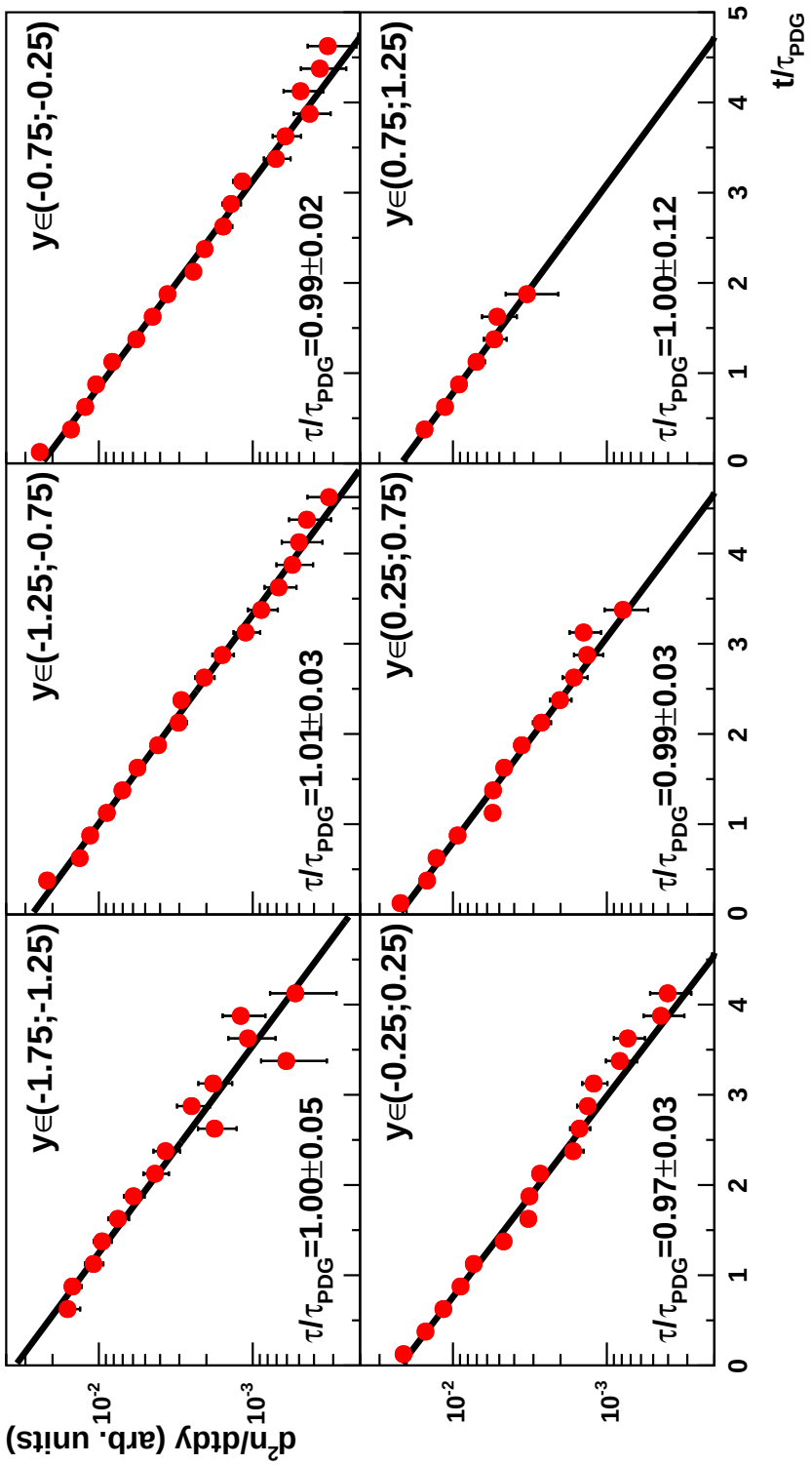

Figure 6.5. Mean lifetime τ is calculated as negative inverse slope parameter of double-differential cross-section dependent on lifetime. The lifetimes are normalised to the PDG value [50].

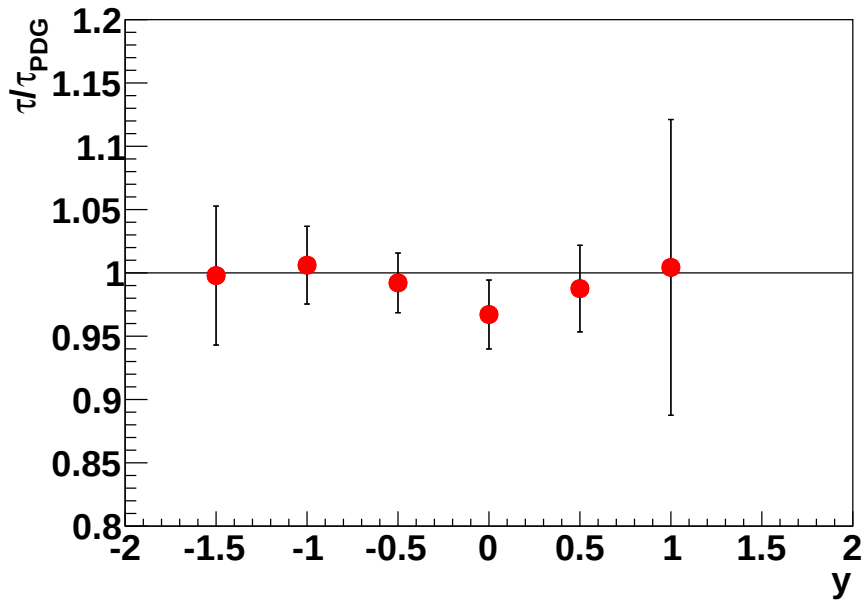

Figure 6.6. Dependence of the mean Λ-lifetime on rapidity. The results are consistent with the PDG value [50].

($t = r/(\gamma\beta)$, where γ, β are Lorentz' variables). After $d^2n/(dydt)$ was calculated, an exponential function was fitted to its dependence on t/τ_{PDG} (Fig. 6.5). From the properties of the exponential function, negative inverse slope equals to the mean lifetime τ/τ_{PDF}. The dependence of the mean lifetime on rapidity was checked for and it is shown in Fig. 6.6.

The values for all the rapidity bins are consistent with the PDG data.

In addition to that, the forward-backward symmetry of the data was checked for. The final double- and single-differential spectra were used for the test. The differences between the results for the backward and the forward hemisphere are within the statistical errors, therefore the test has been passed (see: Appendix C.7).

6.3 Comparison with the World Data

The single-differential multiplicity spectra have been compared to the results of 5 bubble-chamber experiments measuring p+p interactions at beam momenta slightly different from the data presented in this paper (Fig. 6.7). These experiments were able to perform a good-quality measurements in 2π solid angle, covering the whole hemisphere with negative rapidities, although with rather small statistics [74–78]. All the data sets have been normalised to the mean multiplicity of Λ-hyperon, obtained from the referred papers themselves. The same data sets were used also to compute the correction factor used for calculation of the systematic uncertainty of $\langle\Lambda\rangle$ (for

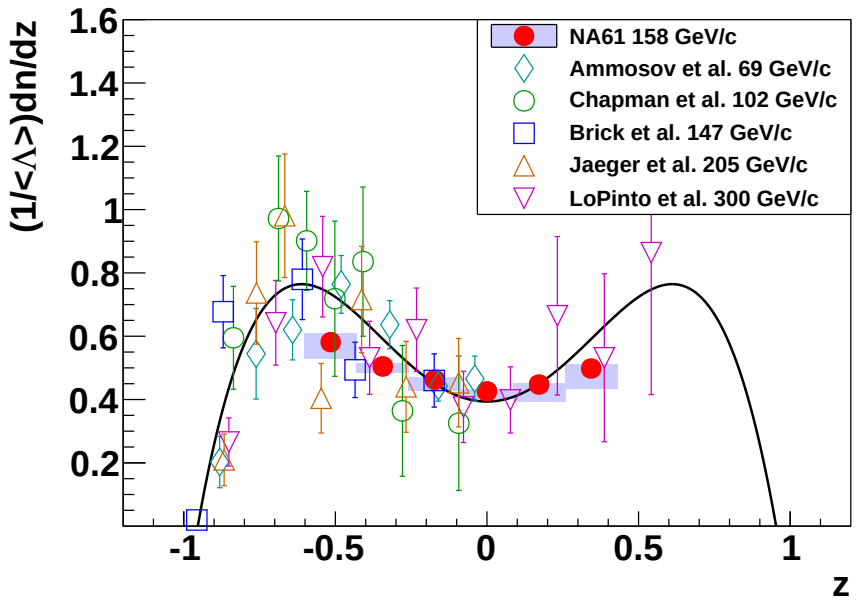

Figure 6.7. Comparison between the NA61/SHINE data and the data obtained with a number of bubble-chamber experiments [74–78]. The function $\frac{1}{\langle\Lambda\rangle}\frac{dn}{dz}(z) = 0.394 + 1.99z^2 - 2.66z^4$ is used for the extrapolation to the full phase-space, where z stands for y/y_{beam}. For details see Section 6.5.

NA61/SHINE calculation of mean multiplicity see: Section 6.5).

Although the statistical error and the systematic uncertainty of the NA61/SHINE measurement is much smaller than for the other experiments, and the results are completely consistent with all the datasets used for the comparison, NA61/SHINE does not observe the general tendency obtained by fitting a symmetric polynomial of 4^{th} order. On the other hand, the dataset by Brick et al. [76], as a dataset for which the beam momentum (147 GeV/c) differs from this thesis (158 GeV/c) at least, shows the best conformity with our experiment (Fig. 6.8). These discrepancies might be caused by a change in production mechanism for higher energies.

Dependence of the invariant spectrum on x_F for NA61/SHINE and some bubble chamber experiments [74, 76–80] is shown in Fig. 6.9. The NA61/SHINE p+p data at 158 GeV/c for central x_F are consistent with the experiments performed at proton beam of lower energy. The effect seems to be caused by an abrupt change in the mechanism responsible for Λ production. The production at middle-x_F seems to be consistent with all the presented energies.

Fig. 6.10 shows $\frac{dn}{dy}$ normalised to the number of wounded nucleons $\langle N_W \rangle$ from this paper compared with the data for heavy-ion collisions from NA49 at 158A GeV/c [82, 83]. Increase in production of Λ with the system size is observed.

Fig. 6.11 compares the yields for the mid-rapidity between p+p and heavy-ion interactions at 158A GeV/c [82, 83]. Increase in the production and the temperature

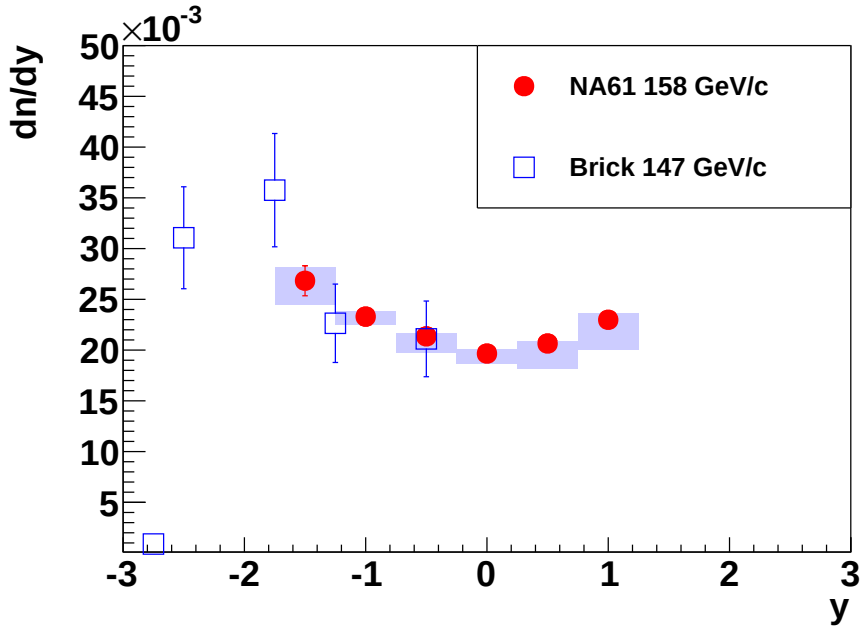

Figure 6.8. A direct comparison with Brick et al. [76].

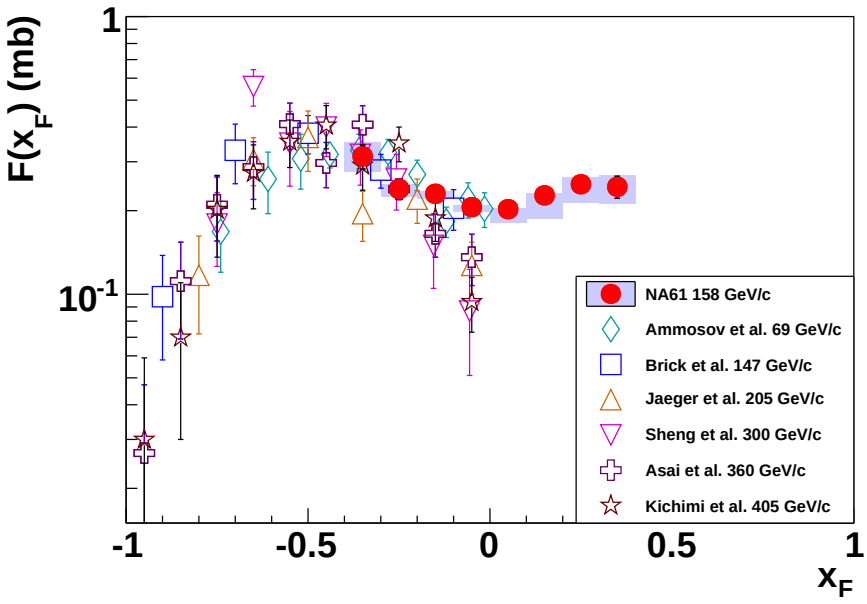

Figure 6.9. Comparison of the invariant cross-section $F(x_F) = \sigma_{inel.} F_n(x_F)$ with the data of a set of experiments performed with the bubble chambers for beam momenta near to 158 GeV/c [74, 76–80]. The NA61/SHINE data points are marked with full circles. The NA61/SHINE invariant yields are multiplied by $\sigma_{inel.} = 31.8$ mb for p+p at 158 GeV/c [81].

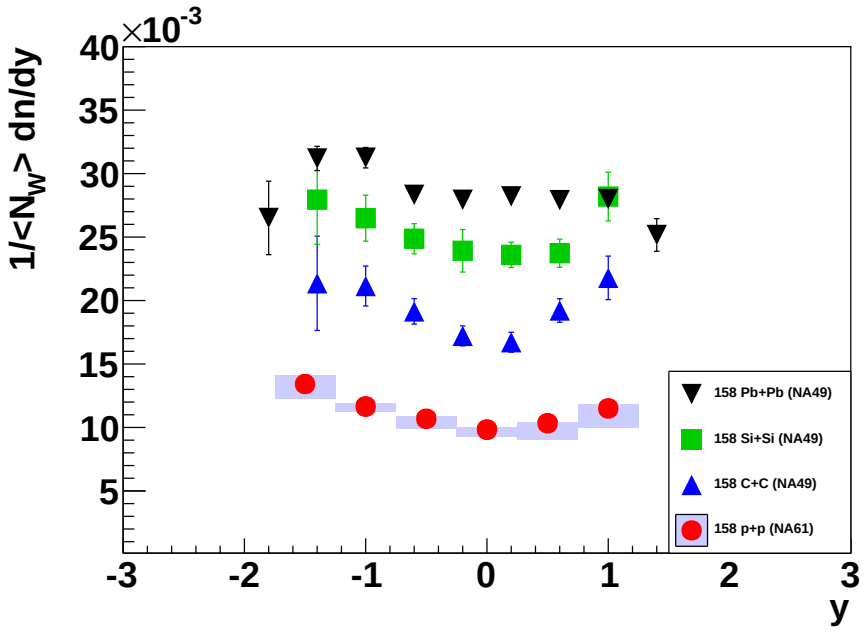

Figure 6.10. Λ-hyperon y-distribution scaled to the number of wounded nucleons. NA61/SHINE data obtained in this thesis for p+p are compared with NA49 central C+C, Si+Si [82], and Pb+Pb [83] data for beam momentum of 158A GeV/c.

(negative inverse slope of the fit increase with the system size) is visible.

Fig. 6.12 shows the dependence of mean transverse mass $\langle m_T \rangle - m_\Lambda$ on rapidity y for Λ produced in p+p interactions at 158 GeV/c (this paper), and is compared with the data on proton production in Pb+Pb reaction at 158A GeV/c [84]. This parameter describes the state of the system at decoupling temperature.

6.4 Comparison with the MC-Generators

The comparison with the model predictions for EPOS 1.99 [66], UrQMD 3.4 [85, 86], and FRITIOF 7.02 [87, 88] (Fig. 6.13). The FRITIOF model was run by employing the HSD 2.0 [89] code. The latter uses FRITIOF for the simulation of nucleon-nucleon interactions in a direct way.

The FRITIOF model assumes that all hadron-hadron interactions are binary reactions, $h_1 + h_2 \rightarrow h_1' + h_2'$, where h_1' and h_2' are excited states of the hadrons with continuous mass spectra. If one of the post- interaction hadrons remains in the ground state ($h_1 + h_2 \rightarrow h_1 + h_2'$) the reaction is referred to as 'single diffraction dissociation'. If neither hadron remains in the ground state the reaction is referred to as 'double diffraction dissociation'. The excited hadrons are considered as QCD-strings, and the corresponding LUND-string fragmentation model is applied for a simulation of their decays [90].

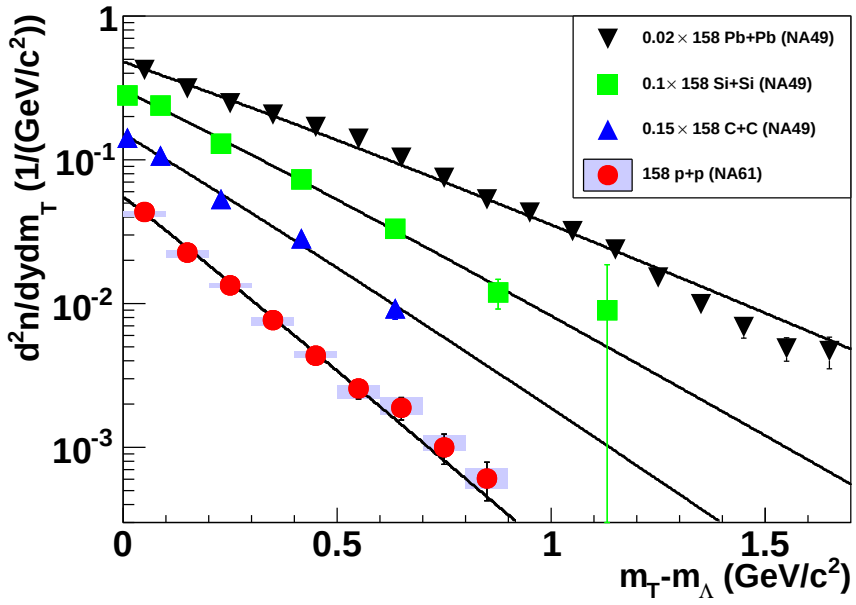

Figure 6.11. Comparison of m_T at mid-rapidity ($|y| \leq 0.4$ for N+N, $|y| \leq 0.25$ for p+p) between NA61/SHINE p+p and central C+C, Si+Si [82], and Pb+Pb [83] data for beam momentum of 158A GeV/c. The lines are fitted using Eq. (5.14).

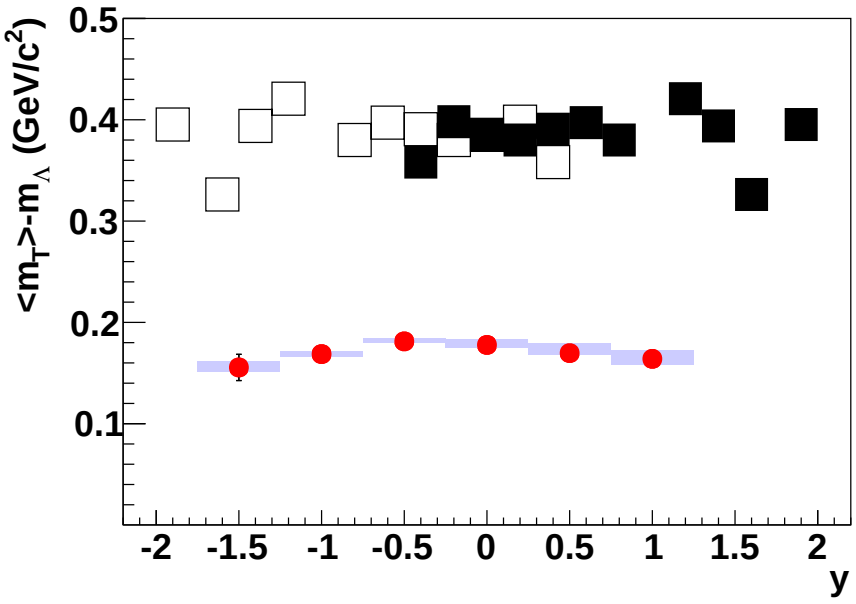

Figure 6.12. Mean transverse mass dependence on rapidity. The round symbols stay for the data on Λ production from NA61/SHINE p+p at 158 GeV/c, while the full squares represent the data on proton production from the central Pb+Pb events at 158A GeV/c from the NA49 experiment [84]. Open symbols are mirrored with respect to $y = 0$.

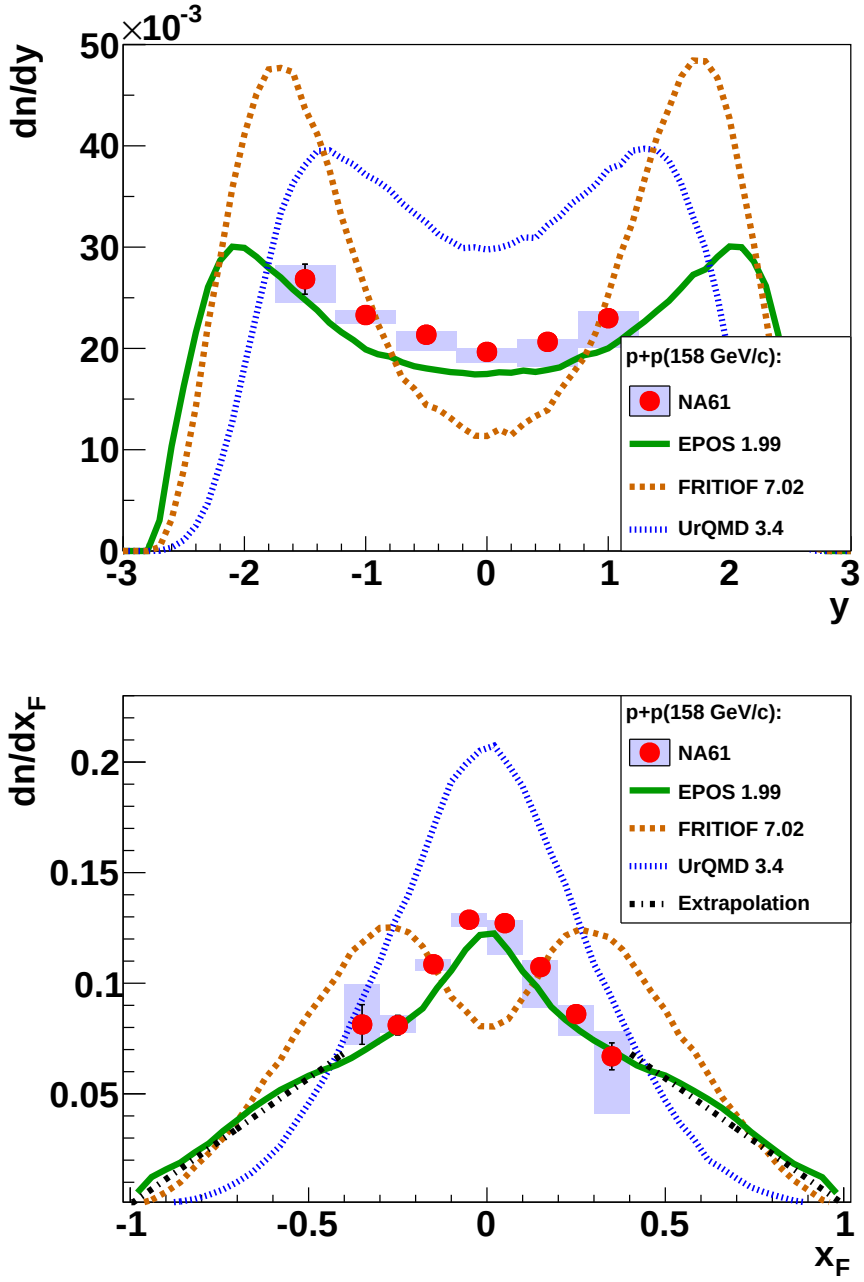

Figure 6.13. Comparison of $\frac{dn}{dy}$, and $\frac{dn}{dx_F}$ spectra with MC models. Although EPOS [66] reproduces the measured data much better than UrQMD [85,86] and FRITIOF [87,88] (run by HSD2.0 [89]), the model predicts the production of Λ well below the experimental data.

The FRITIOF model fails easily due to fragmentation function used by default. It is particularly visible in the $\frac{dn}{dx_F}$ plot, where the maximum is pushed away from the $x_F = 0$.

Significant discrepancies are also present in the normalisation of the UrQMD data, while the shape reproduces the experiment very well.

The UrQMD-model is a microscopic transport theory based on the covariant propagation of all hadrons on classical trajectories in combination with stochastic binary scatterings, colour string formation and resonance decay [86].

The best agreement was found in the EPOS predictions, although it is not perfect, still.

EPOS is a sophisticated multiple scattering approach based on partons and Pomerons (parton ladders), with special emphasis on high parton densities. The latter aspect, particularly important in proton-nucleus or nucleus- nucleus collisions, is taken care of via an effective treatment of Pomeron-Pomeron interactions, referred to as parton ladder splitting. In addition, collective effects are introduced after separating the high density central core from the peripheral corona. EPOS is the successor of the NEXUS model. Transformation of the partons into observable hadrons consists of two steps: given the partons, strings are formed. Then, these strings 'fragment' into hadrons [91].

EPOS code was issued after the NA49 data on p+p were published, which might enable the authors to improve the performance of this model in the SPS-energy range.

6.5 Mean Multiplicity

Mean multiplicity of Λ-hyperons ($\langle\Lambda\rangle$) is determined using $F_n(x_F)$-distribution. As none of the models applicable in the SPS energies range reproduce the NA61/SHINE data very well (Fig. 6.13), the Λ yield in the unmeasured x_F region ($|x_F| > 0.4$) is approximated by the straight line. The extrapolated correction amounts to 34.3% of the total Λ yield.

For the estimation of $\langle\Lambda\rangle$ systematic uncertainty the same procedure as for the yields was applied (Section 5.8). Another source of uncertainty comes from the different approach to the calculation of mean multiplicity. This is done by fitting a symmetric polynomial of 4^{th} order [92] to $(1/\langle n\rangle)(dn/dz)$ distributions obtained by 5 bubble-chamber experiments [74–78], where z stands for y/y_{beam}. The first step of interpolation takes into account only the 5 aforementioned datasets. At the next step, the NA61/SHINE data was normalised to the correction factor obtained at the first step and added to the data as the 6^{th} set for the fit. Then, the procedure is repeated using those 6 datasets until the correction factor converges. Ratio of the integral of the final fit $\frac{1}{\langle\Lambda\rangle}\frac{dn}{dz}(z) = 0.394 + 1.99z^2 - 2.66z^4$ (Fig. 6.7) for the full

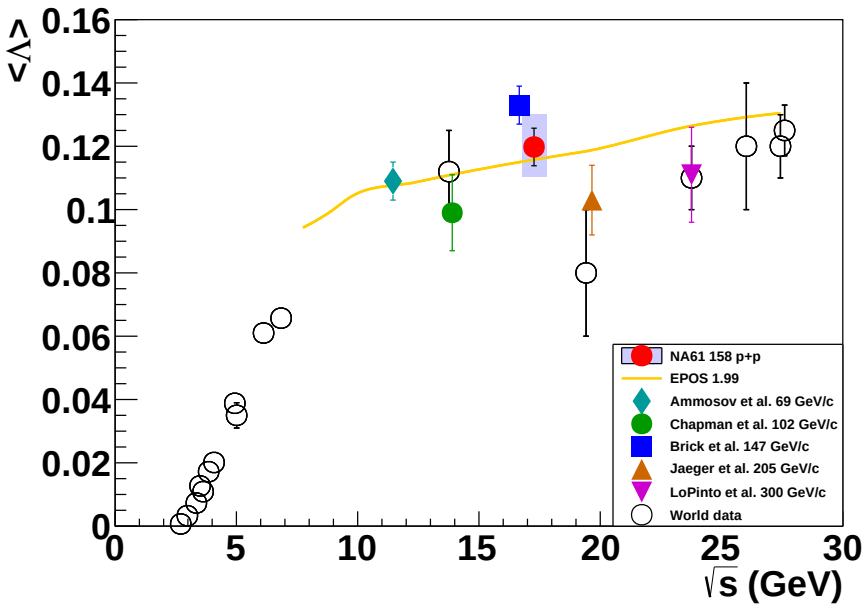

Figure 6.14. Dependence of Λ mean multiplicity on energy. The experiments used for the NA61/SHINE systematic uncertainty calculation are shown as full symbols [74–78]. Open symbols stand for remaining data [93]. The EPOS [66] prediction has been included to guide the eye.

range of rapidity to the integral in the range outside of the acceptance is used as a correction factor. The final correction factor equals to 1.92 ± 0.12, i.e. almost half of the total production of Λ is outside of acceptance for this method. The final value of the mean multiplicity calculated using this method is $\langle \Lambda \rangle = 0.1292 \pm 0.0082$. The difference between mean multiplicity calculated with this method and the linear extrapolation is added in quadrature to the systematic error, in this case contributing to the positive systematic error only.

The final result reads as follows:

$$\langle \Lambda \rangle = 0.1198 \pm 0.0060\ (stat.)\ {}^{+0.010}_{-0.009}\ (sys.).$$

Mean multiplicity of Λ for 158 GeV/c p+p interactions has been compared with the world data [93] in Fig. 6.14. The statistical errors of most of the data are very high, and all of the data points are consistent with the EPOS [66] predictions. EPOS as production model is not applicable to lower energies.

Chapter 7

Summary and Outlook

The main aim of the thesis has been reached. The procedure for the analysis of Λ production at the SPS energy range is ready and fully validated. It has been used to analyse p(158 GeV/c)+p data acquired by NA61/SHINE in 2009.

The results of the analysis are of great importance for the experiment, as for the first time in the history of both NA49 and NA61/SHINE an analysis of Λ production in p+p interactions meet with success!

The outcomes of the thesis are presented in Chapter 6. The results include double-differential spectra $\left(\frac{d2n}{dydp_T}, \frac{d^2n}{dydm_T}, \frac{d2n}{dx_F dp_T}\right)$, single-differential distributions $\left(\frac{dn}{dy}, \frac{dn}{dx_F}\right)$, the $\langle m_T \rangle$ and inverse slope parameter T dependence on y, as well as mean Λ multiplicity extrapolated to 4π, as well as their interpretation and discussion.

The data for p(158 GeV/c)+p interactions presented in this thesis are to be published in EPJ C.

The analysis will be continued for p+p interactions of lower energies. The procedure is ready to be used for the other data-sets recorded by the NA61/SHINE for the momentum of incident proton ranging from 20 to 158 GeV/c. The analysis has been checked also for data with 80 GeV/c, but as recent results they are still awaiting approval from the collaboration. Also a check for 40 GeV/c has been performed, but the whole analysis has not been finish yet. Given the data for lower energies, one has a possibility to check the behaviour of Λ multiplicities in the vicinity of the onset of deconfinement.

After the analysis for the full energy range is finished, the procedure will be tuned up in order to obtain $\bar{\Lambda}$-yields. This is in particular more difficult, as the multiplicity of $\bar{\Lambda}$ are 10 times smaller compared to Λ. Therefore, at least binning has to be changed in order to get reliable results. Then, these data combined with the results of K^0_S analysis will be used as reference for the further measurements with Be+Be, Ar+Sc, Xe+La, and eventually Pb+Pb to find a system and energy where the deconfinement starts to be visible. The analysis for the heavy-ions will be very similar to the one

presented in this thesis, the main difference being the centrality selection.

This work seems to be a nice start in the future analyses of strangeness production, enabling to get data for a wide range of energies and system-sizes, in order to get an answer on the questions asked in the Chapter 2.

Appendix A

Kinematic Variables

Given a Lorentz boost in z-direction

$$\begin{pmatrix} t' \\ z' \end{pmatrix} = \begin{pmatrix} \cosh y & \sinh y \\ \sinh y & \cosh y \end{pmatrix} \begin{pmatrix} t \\ z \end{pmatrix} \tag{A.1}$$

one finds an analogy to rotation through an imaginary angle iy. Modulus of this number y is called rapidity. As a kinematic variable it has an advantage of being additive under Lorentz boosts, what results in the fact, that difference in rapidity does not changes from system to system. Rapidity can be treated as a measure of speed expressed in multiplicities of the velocity of light c, which an object would have had, if there had not been any relativistic effects.

In order to find a way how to measure it in experiment, let us express energy and momentum by y:

$$E = m_T \cosh y, \tag{A.2}$$

$$p_z = m_T \sinh y. \tag{A.3}$$

The equation for y can be easily obtained by dividing Eq. (A.3) by Eq. (A.2):

$$y = \operatorname{artanh} \frac{p_z}{E} = \frac{1}{2} \ln \frac{E + p_z}{E - p_z}, \tag{A.4}$$

where transverse mass

$$m_T = \sqrt{m^2 + p_T^2}, \tag{A.5}$$

and transverse momentum

$$p_T = \sqrt{p_x^2 + p_y^2}, \tag{A.6}$$

are invariant under Lorentz boost.

Another one variable describing kinematics in beam direction is Feynman-x. It was introduced by Feynman as a scaling variable in the discussion of inclusive hadronic interactions at large energies [68]. It is defined as follows:

$$x_F = 2p_z^*/\sqrt{s}, \tag{A.7}$$

where p_z^* is a z-component of momentum observed from the centre-of-mass frame, and $\sqrt{s}/2$ is the maximum allowed z-component of the centre-of-mass momentum, where $\sqrt{s}$ stands for the total centre-of-mass energy.

Appendix B

Two Versions of the Fitting Function

Instead of calculating MC correction for missing acceptance, one might apply an integral approach to that problem. The spectra for given k are predicted to follow the thermal ansatz (Eq. (5.12)).

$$\left.\frac{d^2n}{dkdp_T}\right|_k = Ap_T e^{-\frac{\sqrt{p_T^2+m_\Lambda^2}}{T}}$$

and its integral (for T>0 and m_Λ>0) is given by:

$$S = \int_0^{+\infty} \left.\frac{d^2n}{dkdp_T}\right|_k dp_t = A(T^2+Tm_\Lambda)e^{-\frac{m_\Lambda}{T}}$$

one might multiply the cross section by S/S=1

$$\left.\frac{d^2n}{dkdp_T}\right|_y = \frac{S}{A(T^2+m_\Lambda T)e^{-\frac{m_\Lambda}{T}}} Ap_T e^{-\frac{\sqrt{p_T^2+m_\Lambda^2}}{T}}$$

and obtain a version of the equation dependent on two unknown variables (S, T) to be fitted.

$$\left.\frac{d^2n}{dkdp_T}\right|_y = \frac{Sp_T}{T^2+m_\Lambda T} e^{-\frac{\sqrt{p_T^2+m_\Lambda^2}}{T}+\frac{m_\Lambda}{T}}.$$

In that way one obtain the area and its error from fit in a direct way. In that way we eventually reached Eq. (5.13).

Appendix C

Results: Numerical Data and Plots

C.1 Tables

Table C.1. Single-differential yields binned in y. Inverse slope parameter T calculated by fitting the $\frac{d^2n}{dydp_T}$ yields with the Eq. (5.13). Mean transverse mass is calculated with the Eq. (5.15).

y	$\frac{dn}{dy}$ $\times 10^3$	Δ_{stat}	Δ^-_{sys}	Δ^+_{sys}	T (MeV)	Δ_{stat}	Δ^-_{sys}	Δ^+_{sys}	$\langle m_T \rangle$ $(\frac{GeV}{c^2})$	Δ_{stat}	Δ^-_{sys}	Δ^+_{sys}
-1.5	26.8	1.5	2.4	1.4	143.8	6.3	4.9	2.6	0.156	0.013	0.004	0.006
-1.0	23.30	0.65	0.84	0.48	152.8	3.8	1.8	1.9	0.1687	0.0076	0.0027	0.0023
-0.5	21.35	0.43	1.61	0.34	163.0	3.2	1.1	2.9	0.1813	0.0067	0.0015	0.0033
0.0	19.65	0.40	1.03	0.39	160.7	3.6	1.7	3.7	0.1777	0.0076	0.0027	0.0054
0.5	20.64	0.42	2.49	0.24	154.0	3.6	2.4	7.9	0.1697	0.0070	0.0015	0.0098
1.0	22.98	0.62	2.95	0.68	153.9	4.1	6.8	4.7	0.1640	0.0085	0.0058	0.0082

Table C.2. Single-differential yields binned in x_F. Invariant yields $F_n(x_F)$ given by Eq. (5.17).

x_F	$\frac{dn}{dx_F}$ $\times 10^3$	Δ_{stat}	Δ^-_{sys}	Δ^+_{sys}	$F_n(x_F)$ $\times 10^3$	Δ_{stat}	Δ^-_{sys}	Δ^+_{sys}
-0.35	81.3	9.0	9.3	18.2	314	31	38	39
-0.25	81.1	4.4	3.5	4.4	240	12	15	10
-0.15	108.6	2.9	2.8	2.3	230.0	6.1	8.8	5.0
-0.05	128.7	2.3	3.3	2.8	205.9	3.9	6.9	3.5
0.05	127.2	2.3	14.1	1.4	202.4	3.9	21.1	1.4
0.15	107.3	2.7	18.4	3.1	226.9	5.8	39.3	4.3
0.25	86.0	3.8	9.8	4.0	249	11	36	15
0.35	67.0	6.1	25.8	11.6	244	22	32	25

Table C.3. Double-differential yields binned in y and p_T.

y	p_T	$\frac{d^2n}{dydp_T}$ $\times 10^3$ $(\frac{1}{GeV/c})$	Δ_{stat}	Δ^-_{sys}	Δ^+_{sys}
-1.5	0.1	16.0	2.8	2.2	1.0
	0.3	35.3	4.8	5.0	3.5
	0.5	30.3	3.4	2.9	2.1
	0.7	27.1	2.7	1.8	1.6
	0.9	14.0	1.7	0.5	1.1
	1.1	6.2	1.1	0.4	0.5
	1.3	3.22	0.71	0.44	0.55
	1.5	1.36	0.45	0.18	0.22
-1.0	0.1	14.7	1.2	1.2	1.1
	0.3	28.2	1.7	1.2	0.9
	0.5	27.7	1.7	1.2	1.0
	0.7	20.9	1.3	0.7	0.6
	0.9	12.16	0.89	0.84	0.36
	1.1	6.96	0.64	0.19	0.15
	1.3	2.93	0.39	0.13	0.09
	1.5	1.80	0.30	0.11	0.40
	1.7	0.59	0.16	0.04	0.05
	1.9	0.38	0.14	0.04	0.01
-0.5	0.1	10.74	0.59	1.08	0.25
	0.3	24.31	0.95	2.25	0.59
	0.5	25.5	1.0	2.1	0.4
	0.7	20.68	1.00	1.30	0.49
	0.9	12.05	0.77	0.91	0.29
	1.1	6.61	0.55	0.22	0.19
	1.3	3.74	0.41	0.15	0.10
	1.5	1.62	0.25	0.11	0.08
	1.7	0.87	0.19	0.12	0.05
	1.9	0.42	0.14	0.06	0.06
0.0	0.1	10.06	0.56	0.40	0.34
	0.3	22.89	0.87	1.66	0.54
	0.5	23.26	0.91	1.74	0.50
	0.7	18.58	0.89	1.37	0.61
	0.9	11.50	0.78	0.59	0.57
	1.1	5.63	0.59	0.15	0.31
	1.3	3.74	0.49	0.20	0.20
	1.5	1.45	0.27	0.11	0.07
	1.7	0.69	0.20	0.08	0.04
	1.9	0.34	0.11	0.06	0.08
0.5	0.1	10.79	0.63	1.54	0.19
	0.3	23.89	0.95	4.05	0.76
	0.5	27.4	1.0	3.9	0.4
	0.7	18.03	0.88	1.91	0.38
	0.9	11.04	0.78	1.11	0.30
	1.1	5.87	0.57	0.24	0.11
	1.3	3.50	0.49	0.12	0.34
	1.5	1.47	0.30	0.13	0.24
	1.7	0.65	0.21	0.09	0.05
	1.9	0.45	0.14	0.46	0.01
1.0	0.1	11.91	0.91	1.54	1.21
	0.3	26.6	1.4	3.2	1.7
	0.5	29.0	1.5	6.6	1.2
	0.7	21.2	1.4	2.1	1.1
	0.9	13.4	1.1	1.7	0.6
	1.1	7.65	0.80	2.26	0.06
	1.3	3.32	0.56	0.19	0.29
	1.5	1.06	0.28	0.00	0.00

Table C.4. Double-differential yields binned in y and $m_T - m_\Lambda$.

y	$m_T - m_\Lambda$	$\frac{d^2n}{dydm_T} \times 10^3 (\frac{1}{GeV/c^2})$	Δ_{stat}	Δ^-_{sys}	Δ^+_{sys}
-1.5	0.05	62.0	6.2	8.7	4.4
	0.15	31.9	3.2	2.2	2.7
	0.25	18.5	2.1	0.7	1.1
	0.35	8.4	1.3	0.5	0.7
	0.45	4.51	0.92	0.29	0.75
	0.55	2.91	0.73	0.43	0.61
	0.65	1.26	0.43	0.15	0.08
-1.0	0.05	53.8	2.5	2.0	1.1
	0.15	27.3	1.6	1.3	0.9
	0.25	14.6	1.0	0.8	0.6
	0.35	8.40	0.72	0.43	0.24
	0.45	5.10	0.54	0.21	0.32
	0.55	2.50	0.36	0.19	0.06
	0.65	1.44	0.28	0.11	0.22
	0.75	1.16	0.24	0.06	0.20
	0.85	0.58	0.16	0.04	0.10
-0.5	0.05	45.9	1.4	4.1	0.9
	0.15	25.9	1.1	1.6	0.4
	0.25	14.56	0.86	0.96	0.48
	0.35	8.28	0.63	0.59	0.19
	0.45	4.54	0.45	0.17	0.29
	0.55	3.23	0.38	0.17	0.05
	0.65	1.83	0.28	0.06	0.09
	0.75	0.89	0.18	0.04	0.06
	0.85	0.79	0.19	0.08	0.05
	0.95	0.51	0.16	0.07	0.07
0.0	0.05	43.4	1.3	2.8	0.8
	0.15	22.63	0.93	1.73	1.07
	0.25	13.38	0.79	0.57	0.36
	0.35	7.67	0.67	0.65	0.38
	0.45	4.34	0.52	0.16	0.31
	0.55	2.56	0.39	0.39	0.12
	0.65	1.89	0.34	0.18	0.35
	0.75	1.00	0.24	0.05	0.22
	0.85	0.61	0.18	0.09	0.11
0.5	0.05	46.2	1.4	6.9	7.6
	0.15	25.7	1.0	3.5	4.2
	0.25	13.10	0.79	1.10	2.14
	0.35	7.28	0.63	0.75	1.19
	0.45	4.17	0.48	0.10	0.69
	0.55	3.05	0.43	0.16	0.60
	0.65	1.44	0.32	0.08	0.27
	0.75	0.77	0.21	0.09	0.18
	0.85	0.92	0.25	0.11	0.21
	0.95	0.32	0.13	0.03	0.06
1.0	0.05	52.8	2.1	9.4	8.5
	0.15	26.6	1.5	3.0	4.3
	0.25	16.5	1.2	1.9	2.7
	0.35	9.04	0.94	1.19	1.97
	0.45	4.00	0.61	0.66	0.88
	0.55	2.51	0.49	0.31	0.33
	0.65	1.90	0.49	0.16	0.47
	0.75	0.63	0.22	0.08	0.13

Table C.5. Double-differential yields binned in x_F and p_T for $x_F < 0$. Invariant yields $f_n(x_F, p_T)$ given by Eq. (5.16).

x_F	p_T	$\frac{d^2n}{dx_F dp_T}$ $\times 10^3$ $(\frac{1}{GeV/c})$	Δ_{stat}	Δ^-_{sys}	Δ^+_{sys}	$f_n(x_F, p_T)$ $\times 10^3$ $\left(\frac{1}{(GeV/c)^2}\right)$	Δ_{stat}	Δ^-_{sys}	Δ^+_{sys}
-0.35	0.1	44	21	13	33	32	10	11	6
	0.3	127	34	30	38	35.8	6.3	9.1	6.7
	0.5	89	15	7	13	13.6	1.7	0.8	1.3
	0.7	78	12	6	10	8.76	0.98	0.47	0.78
	0.9	37.4	6.4	3.7	4.9	3.31	0.44	0.29	0.24
	1.1	15.4	3.4	0.8	1.0	1.12	0.20	0.08	0.05
	1.3	9.3	2.2	0.7	1.0	0.57	0.12	0.05	0.03
	1.5	4.6	1.5	0.8	1.5	0.248	0.076	0.036	0.052
-0.25	0.1	45.5	8.9	3.9	3.4	23.2	3.9	3.6	3.6
	0.3	110	14	11	10	17.3	2.3	2.7	1.1
	0.5	92	11	6	5	8.6	1.2	1.2	0.3
	0.7	78.9	7.4	2.2	1.7	5.44	0.67	0.97	0.14
	0.9	41.4	4.5	1.1	3.9	2.36	0.34	0.51	0.07
	1.1	21.8	2.8	0.9	0.9	0.99	0.18	0.17	0.04
	1.3	8.5	1.6	0.6	0.6	0.347	0.092	0.080	0.012
	1.5	4.7	1.1	0.3	1.1	0.170	0.060	0.033	0.034
	1.7	1.71	0.58	0.12	0.19	0.057	0.031	0.008	0.005
-0.15	0.1	68.7	5.8	3.9	2.5	24.2	2.0	0.9	1.6
	0.3	135.6	7.8	3.2	4.2	15.72	0.84	0.39	0.50
	0.5	132.9	7.4	4.2	3.7	9.43	0.53	0.32	0.24
	0.7	101.6	6.0	2.1	3.1	5.22	0.35	0.11	0.20
	0.9	53.4	3.9	2.7	1.3	2.25	0.20	0.10	0.06
	1.1	29.6	2.7	0.9	1.1	1.06	0.13	0.04	0.04
	1.3	11.6	1.6	0.5	0.4	0.372	0.070	0.015	0.011
	1.5	5.9	1.1	0.6	0.5	0.174	0.047	0.017	0.015
	1.7	2.64	0.73	0.19	0.09	0.071	0.030	0.005	0.002
-0.05	0.1	72.7	3.4	2.0	2.5	17.45	0.85	1.14	0.28
	0.3	161.4	5.4	5.4	4.9	12.66	0.46	0.45	0.27
	0.5	160.8	5.6	4.6	3.5	7.93	0.33	0.24	0.24
	0.7	118.5	5.2	3.0	2.8	4.45	0.25	0.11	0.07
	0.9	64.1	4.0	2.0	2.2	2.02	0.17	0.06	0.05
	1.1	33.0	2.9	0.8	1.3	0.92	0.11	0.02	0.04
	1.3	20.2	2.3	1.3	1.7	0.516	0.092	0.032	0.037
	1.5	7.2	1.2	0.6	0.4	0.174	0.048	0.017	0.008
	1.7	4.8	1.2	0.4	0.3	0.110	0.046	0.010	0.006
	1.9	0.55	0.32	0.07	0.16	0.012	0.011	0.002	0.003

Table C.6. Double-differential yields binned in x_F and p_T for $x_F > 0$. Invariant yields $f_n(x_F, p_T)$ given by Eq. (5.16).

x_F	p_T	$\frac{d^2n}{dx_F dp_T}$ $\times 10^3$ $(\frac{1}{GeV/c})$	Δ_{stat}	Δ^-_{sys}	Δ^+_{sys}	$f_n(x_F, p_T)$ $\times 10^3$ $\left(\frac{1}{(GeV/c)^2}\right)$	Δ_{stat}	Δ^-_{sys}	Δ^+_{sys}
0.05	0.1	70.3	3.5	8.7	2.2	17.29	0.84	2.77	1.23
	0.3	160.9	5.4	22.5	2.4	13.07	0.47	1.71	0.17
	0.5	166.4	5.6	20.4	1.9	8.39	0.34	1.02	0.09
	0.7	113.1	4.9	13.0	1.7	4.35	0.24	0.47	0.08
	0.9	64.4	4.2	7.3	1.0	2.03	0.17	0.17	0.04
	1.1	33.5	3.2	2.4	1.0	0.94	0.12	0.07	0.03
	1.3	17.0	2.3	1.1	0.7	0.440	0.086	0.037	0.018
	1.5	6.0	1.3	0.2	0.4	0.144	0.045	0.005	0.009
	1.7	2.56	0.82	0.33	0.13	0.059	0.029	0.008	0.003
	1.9	1.19	0.51	0.21	0.23	0.026	0.018	0.005	0.006
0.15	0.1	63.1	4.5	8.5	5.6	19.6	1.4	4.2	1.0
	0.3	131.5	6.6	26.6	5.5	14.50	0.77	2.36	0.74
	0.5	146.8	7.0	35.4	4.0	9.92	0.54	1.84	0.36
	0.7	87.8	5.7	16.2	3.2	4.41	0.32	0.55	0.20
	0.9	61.2	4.7	6.6	1.6	2.51	0.23	0.65	0.09
	1.1	22.3	2.7	2.3	1.0	0.79	0.12	0.08	0.04
	1.3	15.1	2.5	2.2	1.3	0.472	0.099	0.040	0.044
	1.5	6.6	1.4	1.0	0.4	0.186	0.055	0.032	0.012
	1.7	1.39	0.63	0.28	0.29	0.039	0.023	0.008	0.007
0.25	0.1	43.7	7.0	9.4	5.2	22.6	3.4	3.0	3.0
	0.3	115	10	8	9	17.3	1.5	3.4	1.2
	0.5	104.7	9.4	11.0	4.7	9.91	0.87	1.03	1.24
	0.7	91.9	8.2	13.4	5.4	6.21	0.58	1.60	0.42
	0.9	44.7	5.8	8.9	2.7	2.45	0.33	0.48	0.10
	1.1	16.8	3.3	3.5	1.5	0.80	0.17	0.18	0.05
	1.3	8.7	2.1	0.7	0.9	0.329	0.093	0.038	0.044
	1.5	2.9	1.1	0.4	0.4	0.113	0.048	0.016	0.012
0.35	0.1	29	12	16	14	11.7	6.7	2.9	1.2
	0.3	81	17	28	23	15.5	3.3	6.2	4.4
	0.5	91	16	39	21	10.8	1.9	1.7	2.4
	0.7	61	11	25	19	4.97	0.93	0.76	1.69
	0.9	37.4	8.2	22.3	6.1	2.61	0.58	0.49	0.26
	1.1	17.3	5.1	6.3	6.0	0.96	0.30	0.28	0.12
	1.3	11.7	3.6	4.3	2.6	0.56	0.20	0.17	0.14

C.2 2D-Plots: Dependence on y,p_T

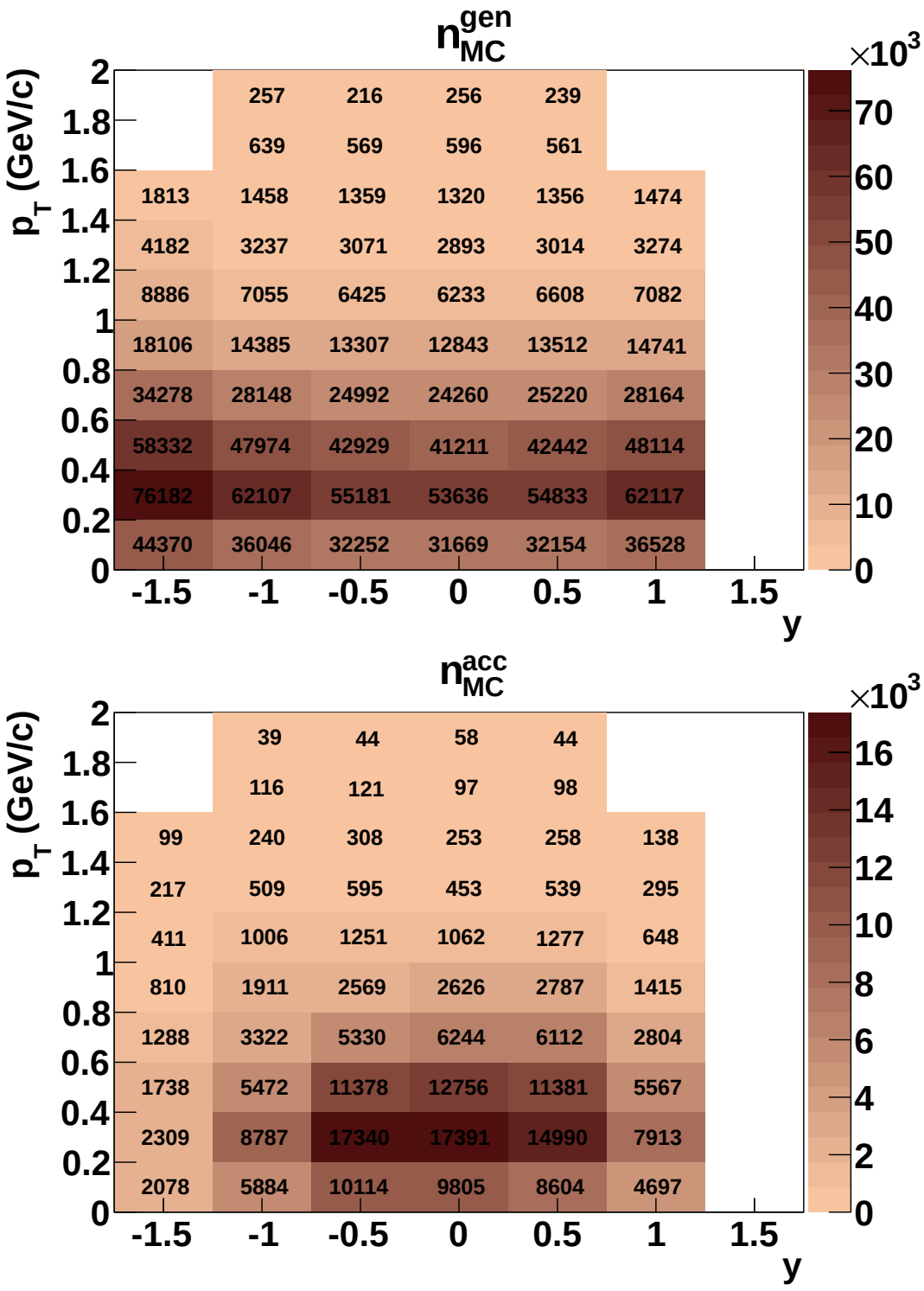

Figure C.1. *Top:* Raw number of generated Λ-particles (n^{gen}_{MC}). *Bottom:* Reconstructed, extracted and accepted number of Λ candidates from the simulation n^{acc}_{MC}.

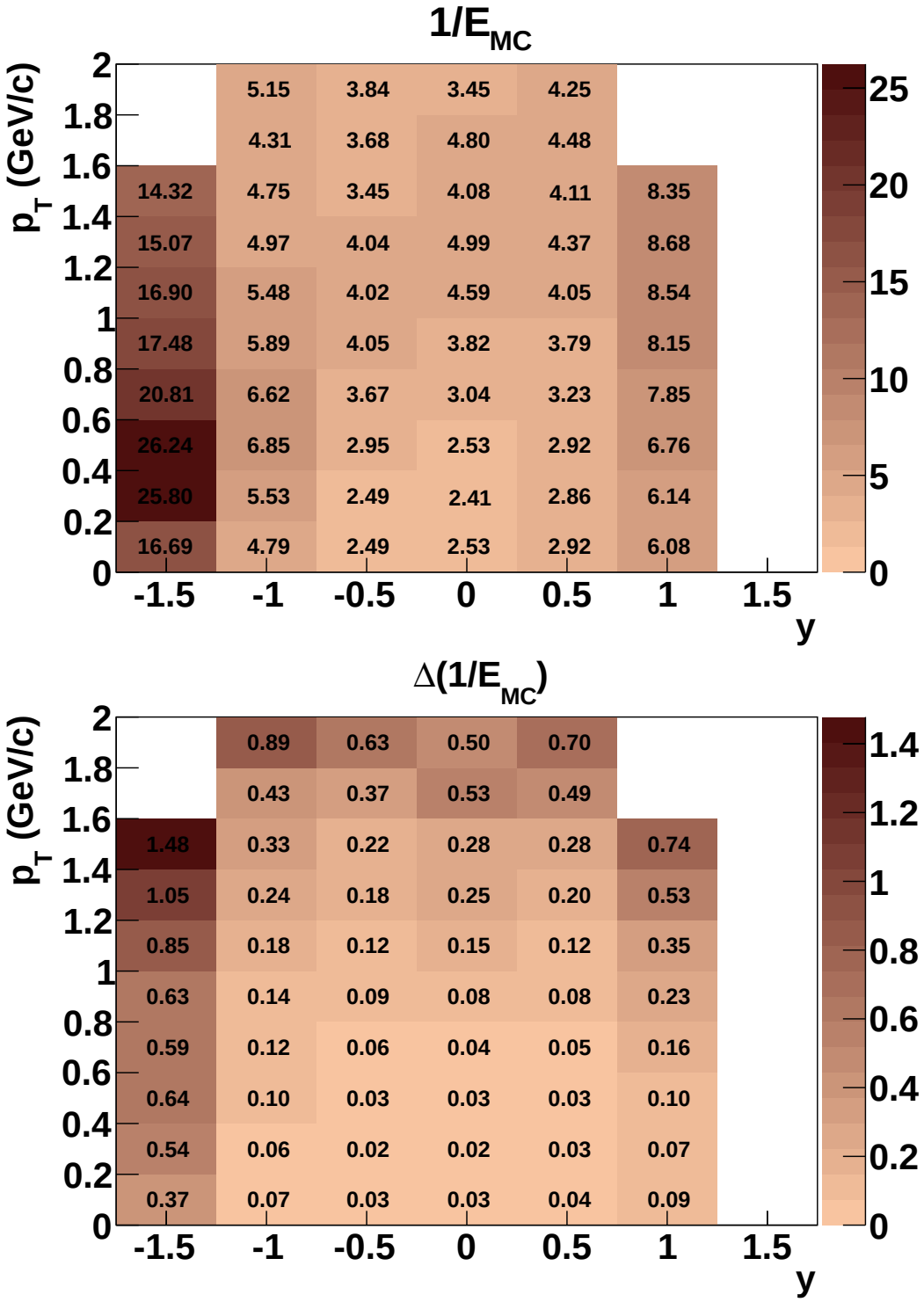

Figure C.2. *Top:* MC-correction factor $1/E_{MC}$. *Bottom:* Statistical error of the correction factor $\Delta(1/E_{MC})$.

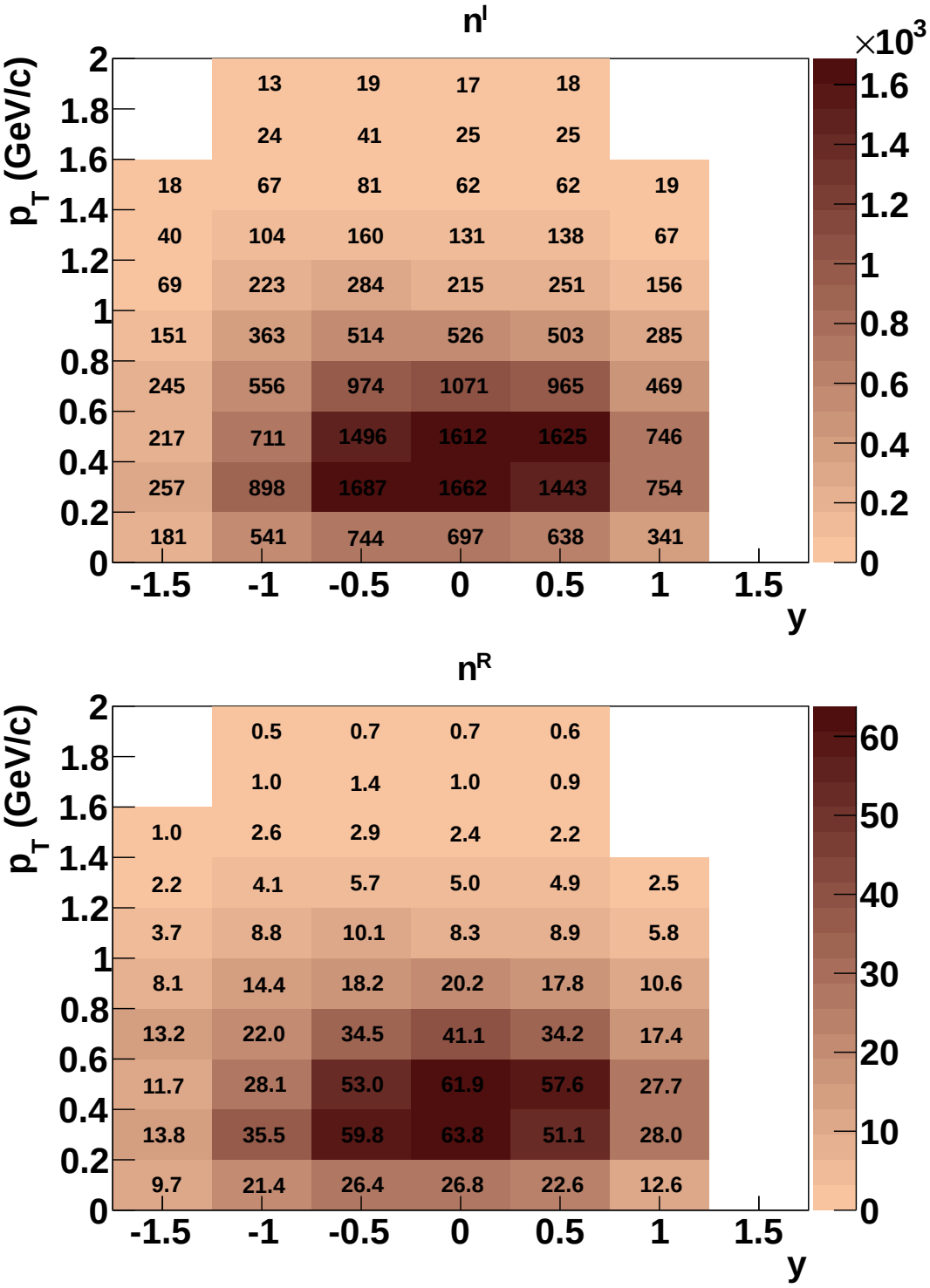

Figure C.3. Raw number of Λ-particles extracted from the experimental data with the LH-inserted configuration of the target (n^I, *top*), and for the LH-removed configuration (n^R, *bottom*).

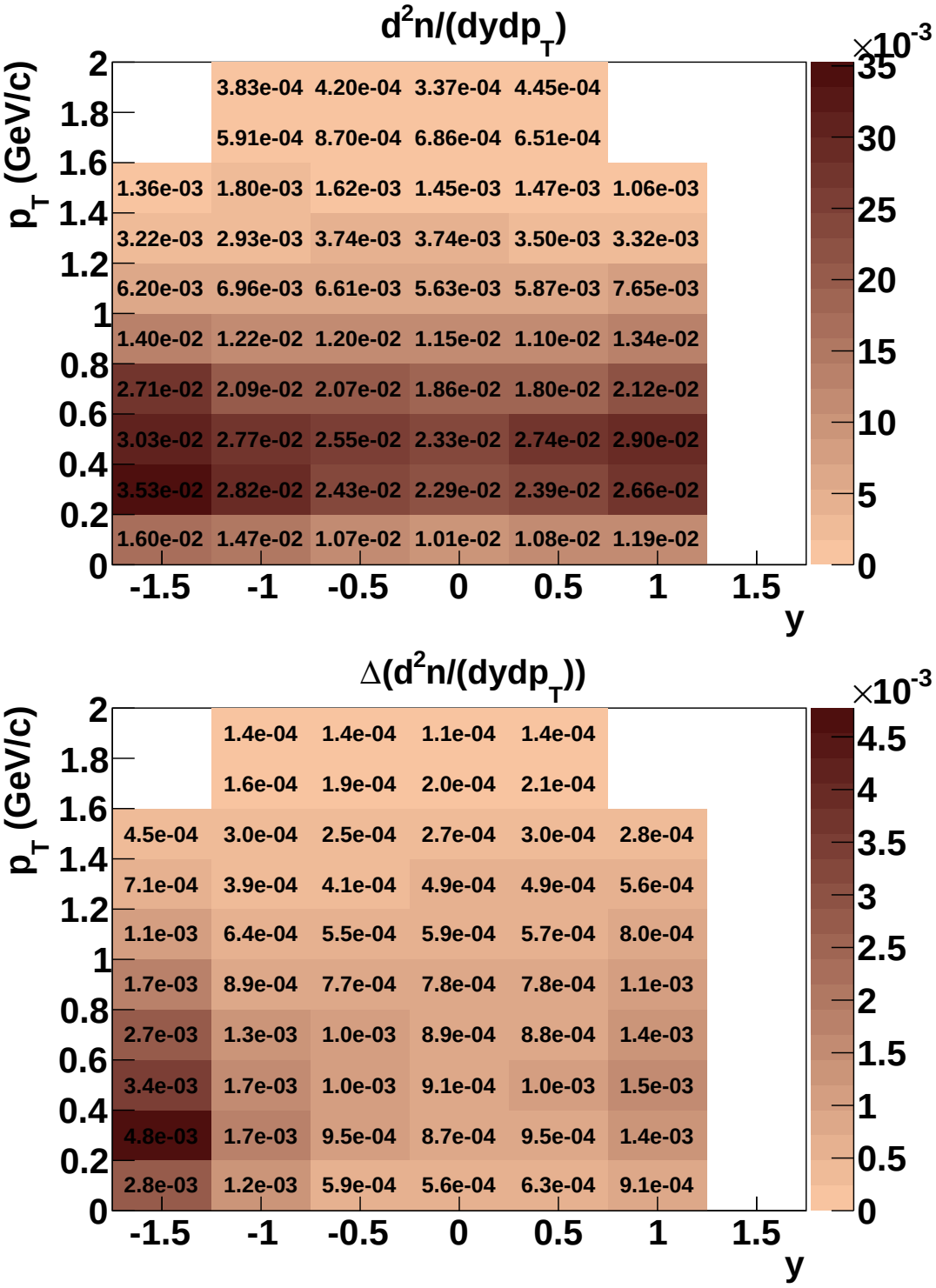

Figure C.4. Corrected spectrum of Λ ($\frac{d^2n}{dydp_T}$, *top*), and its statistical error (*bottom*).

C.3 2D-Plots: Dependence on y,m_T

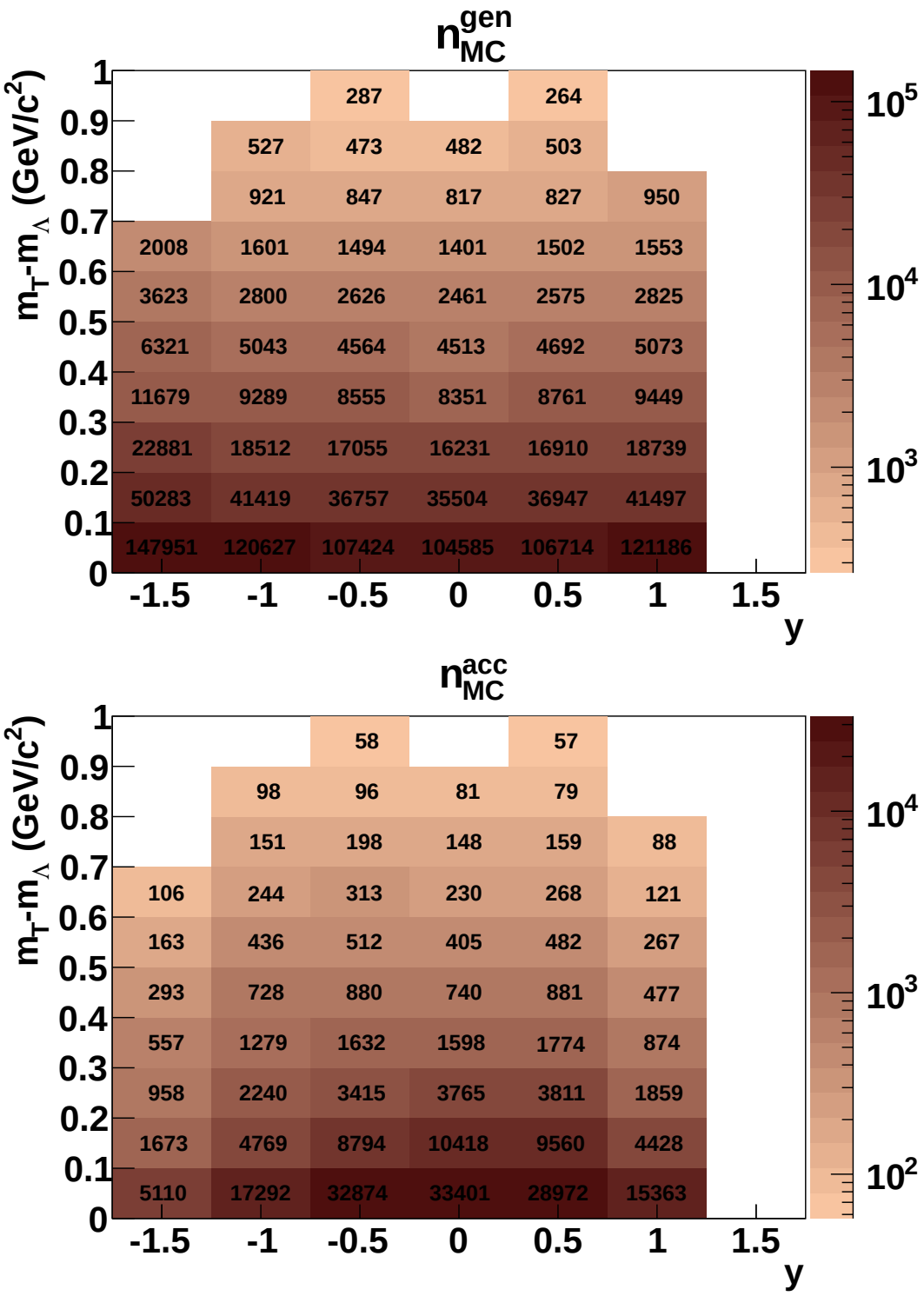

Figure C.5. *Top:* Raw number of generated Λ-particicles (n_{MC}^{gen}). *Bottom:* Reconstructed, extracted and accepted number of Λ candidates from the simulation n_{MC}^{acc}.

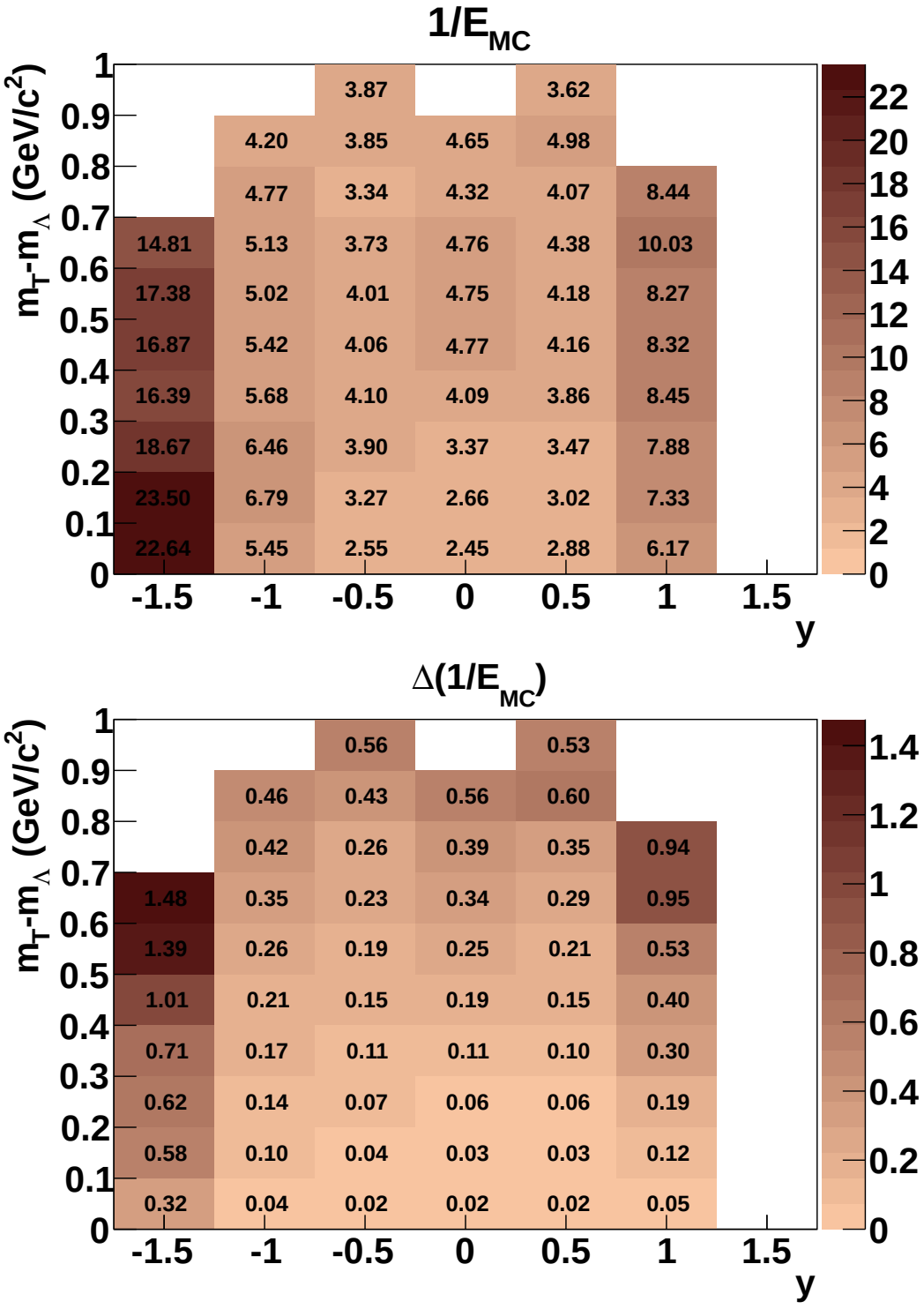

Figure C.6. *Top:* MC-correction factor $1/E_{MC}$. *Bottom:* Statistical error of the correction factor $\Delta(1/E_{MC})$.

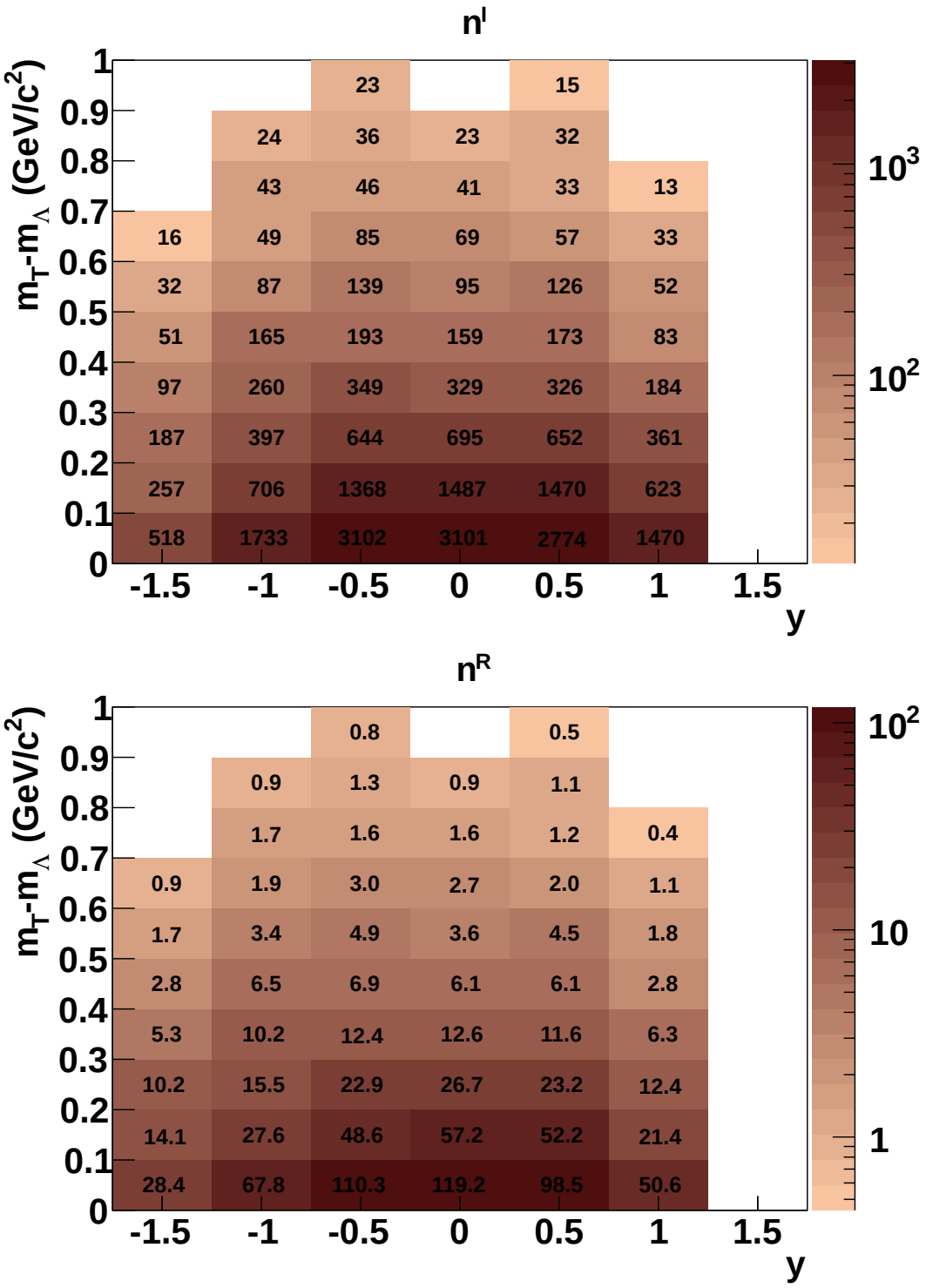

Figure C.7. Raw number of Λ-particles extracted from the experimental data with the LH-inserted configuration of the target (n^I, *top*), and for the LH-removed configuration (n^R, *bottom*).

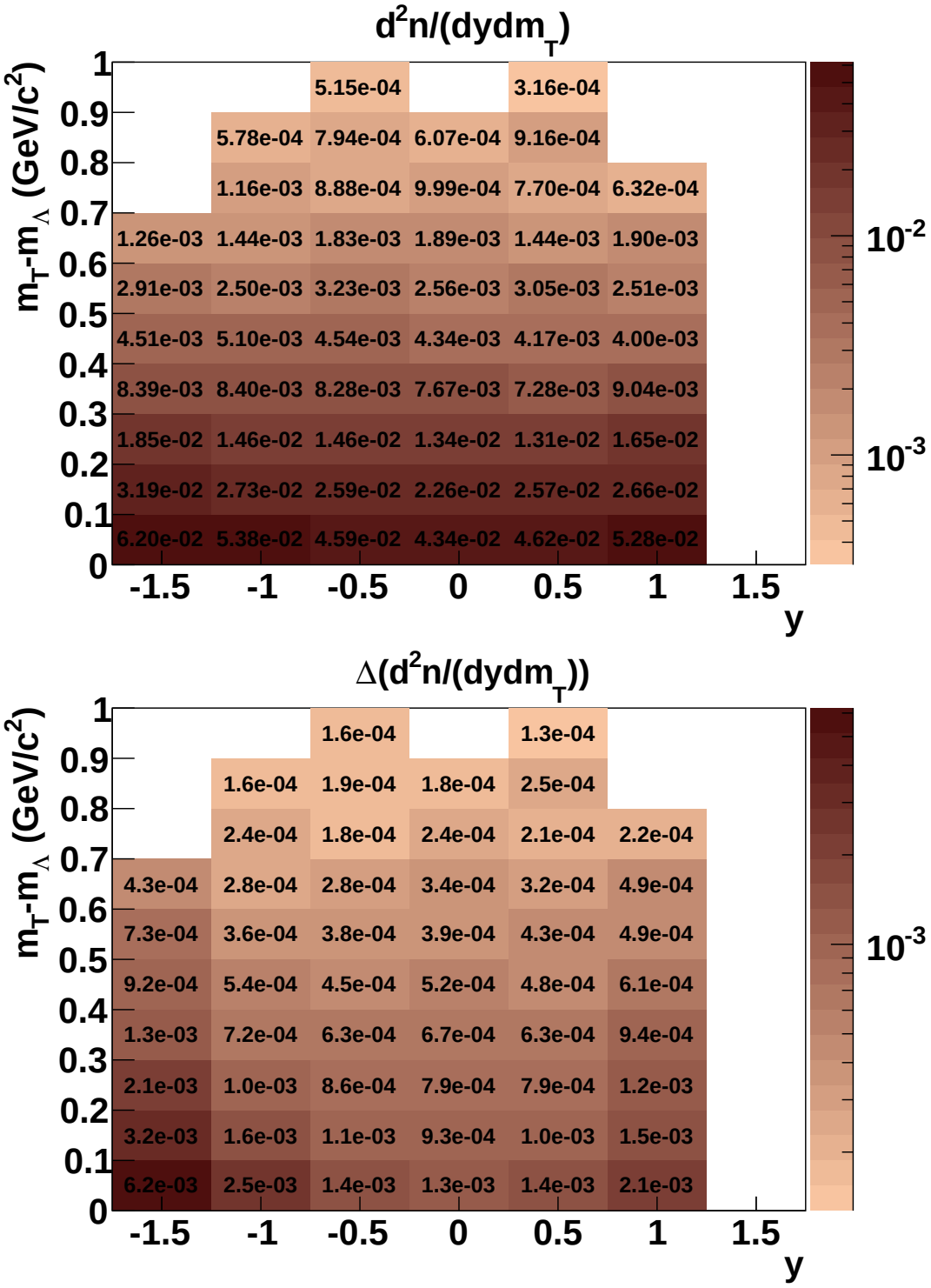

Figure C.8. Corrected spectrum of Λ ($\frac{d^2n}{dydm_T}$, *top*), and its statistical error (*bottom*).

C.4 2D-Plots: Dependence on x_F,p_T

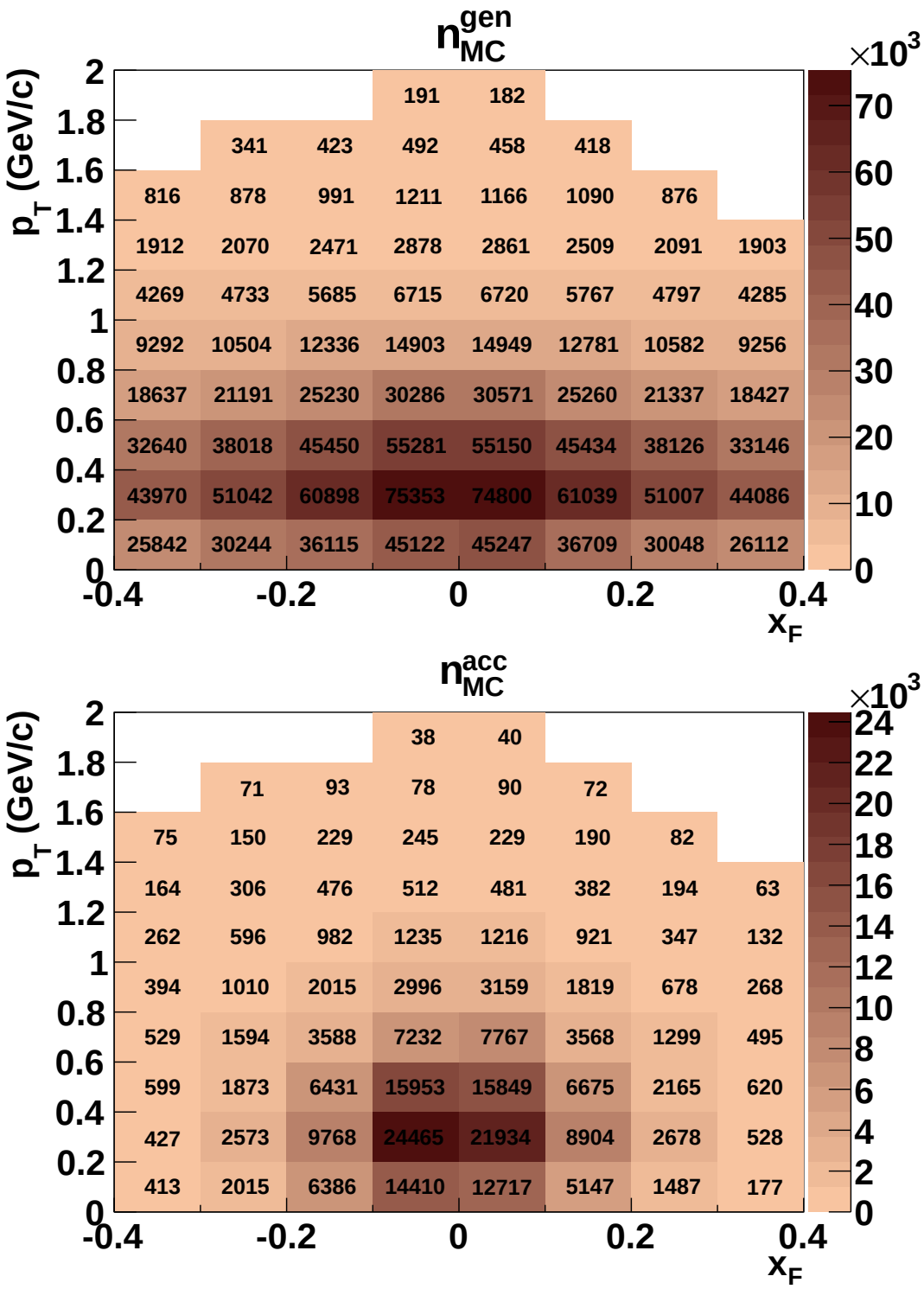

Figure C.9. *Top:* Raw number of generated Λ-particles (n^{gen}_{MC}). *Bottom:* Reconstructed, extracted and accepted number of Λ candidates from the simulation n^{acc}_{MC}.

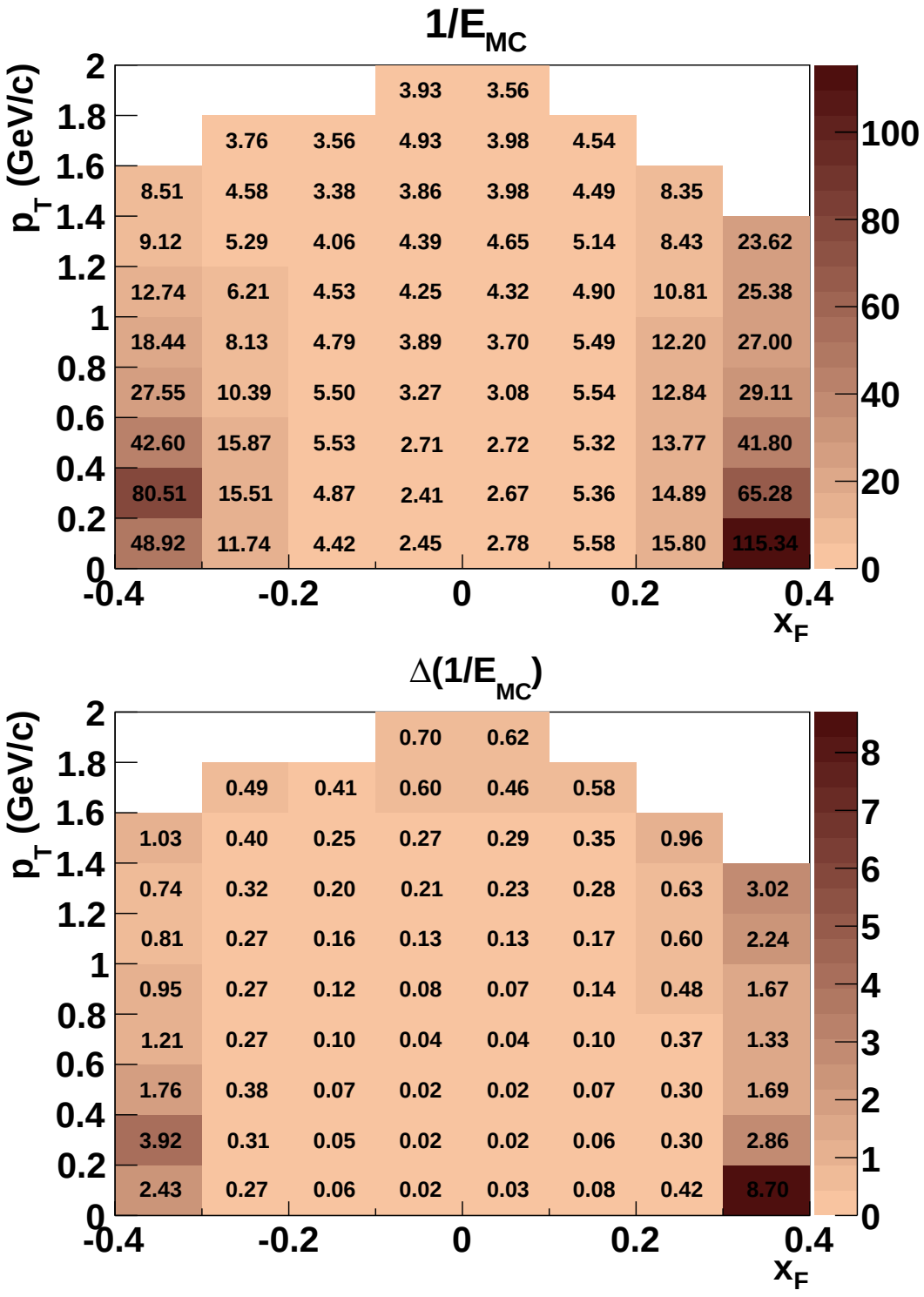

Figure C.10. *Top:* MC-correction factor $1/E_{MC}$. *Bottom:* Statistical error of the correction factor $\Delta(1/E_{MC})$.

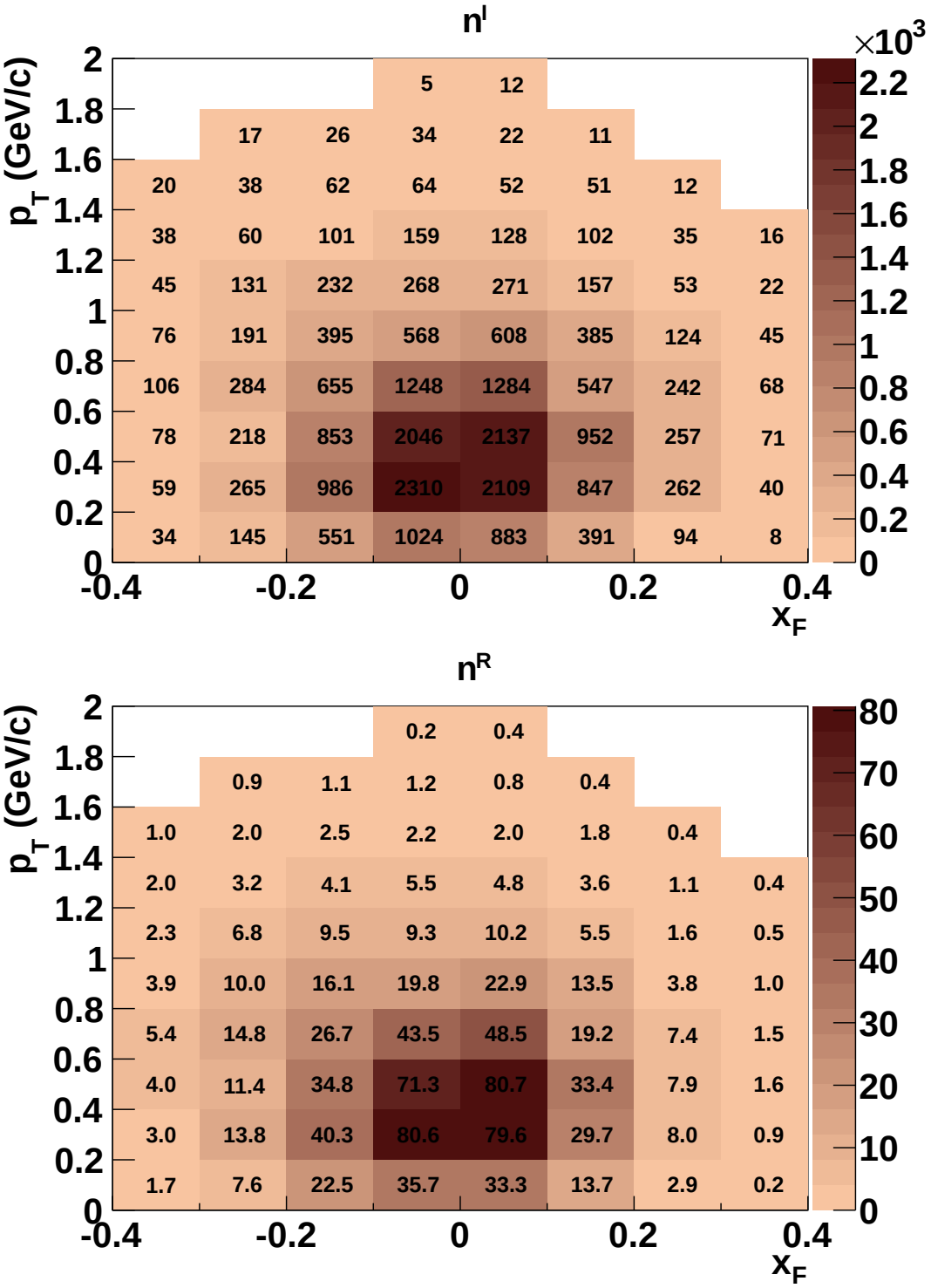

Figure C.11. Raw number of Λ-particles extracted from the experimental data with the LH-inserted configuration of the target (n^I, *top*), and for the LH-removed configuration (n^R, *bottom*).

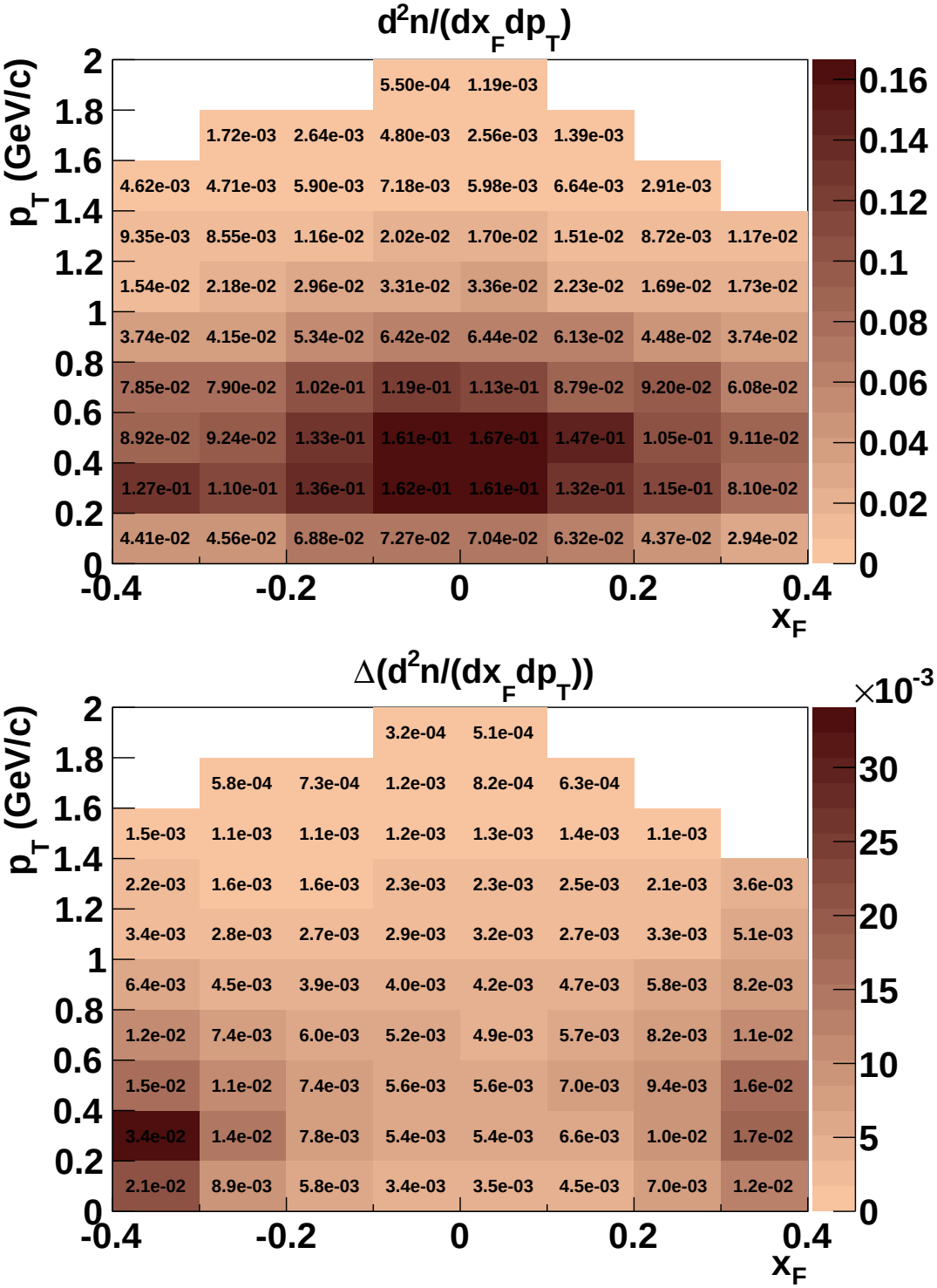

Figure C.12. Corrected spectrum of Λ ($\frac{d^2n}{dx_F dp_T}$, *top*), and its statistical error (*bottom*).

C.5 2D-Plots: Dependence on x_F,p_T - scaled by $2\langle E^*\rangle/(\pi\sqrt{s})$

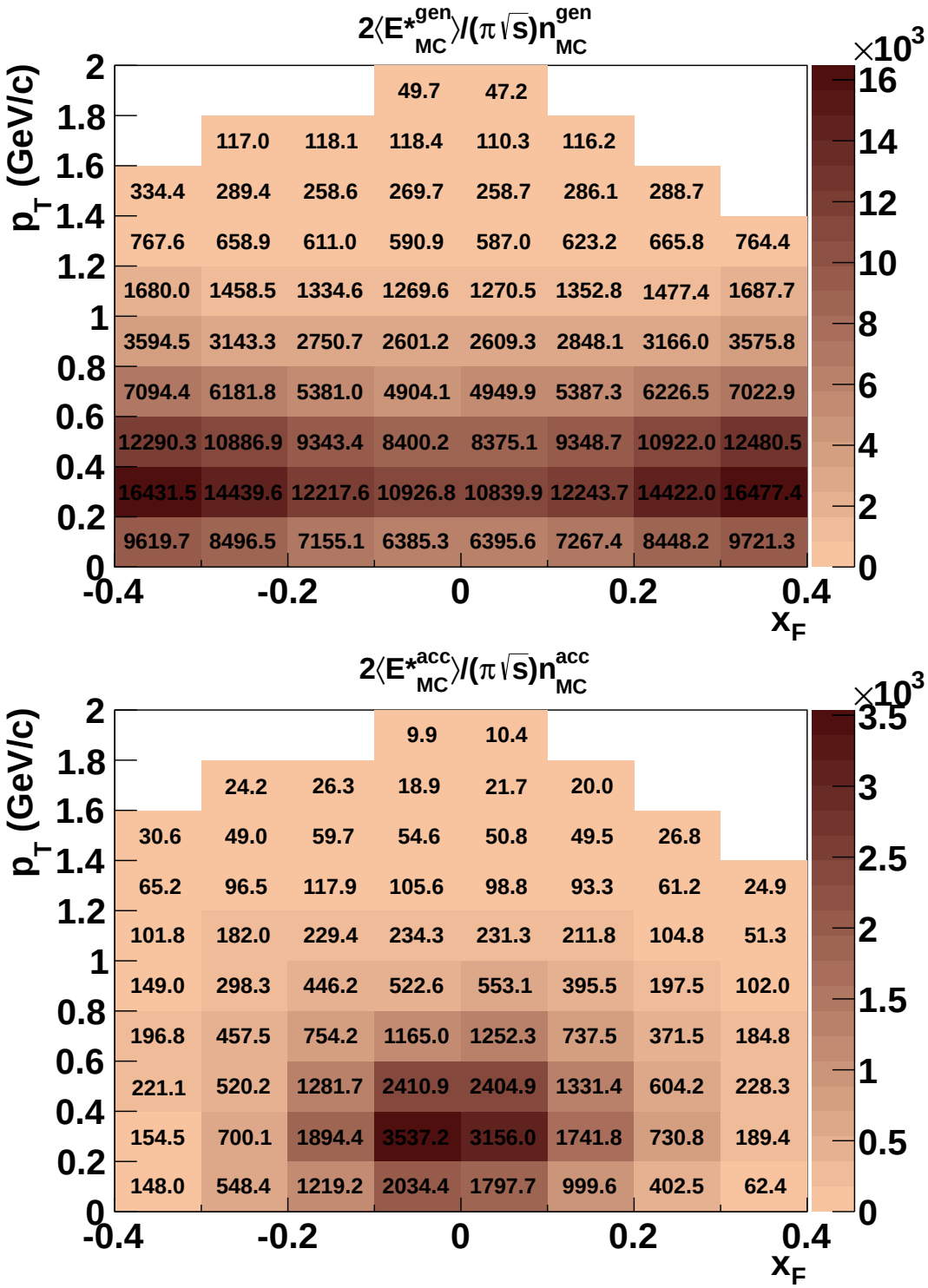

Figure C.13. *Top:* Raw number of generated Λ-particles (n_{MC}^{gen}). *Bottom:* Reconstructed, extracted and accepted number of Λ candidates from the simulation n_{MC}^{acc}. Both observables scaled by $2\langle E^*\rangle/(\pi\sqrt{s})$.

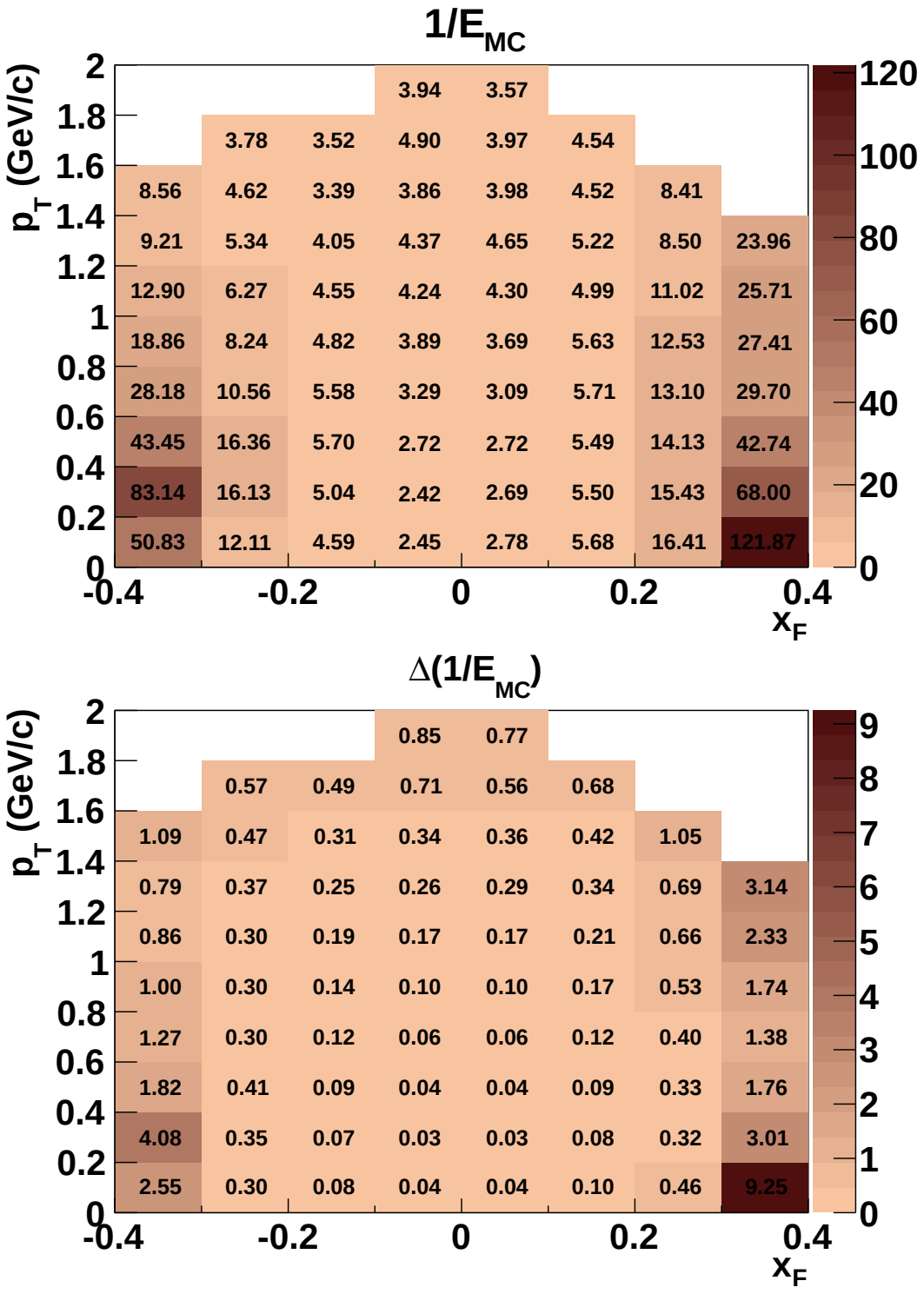

Figure C.14. *Top:* MC-correction factor $1/E_{MC}$. *Bottom:* Statistical error of the correction factor $\Delta(1/E_{MC})$.

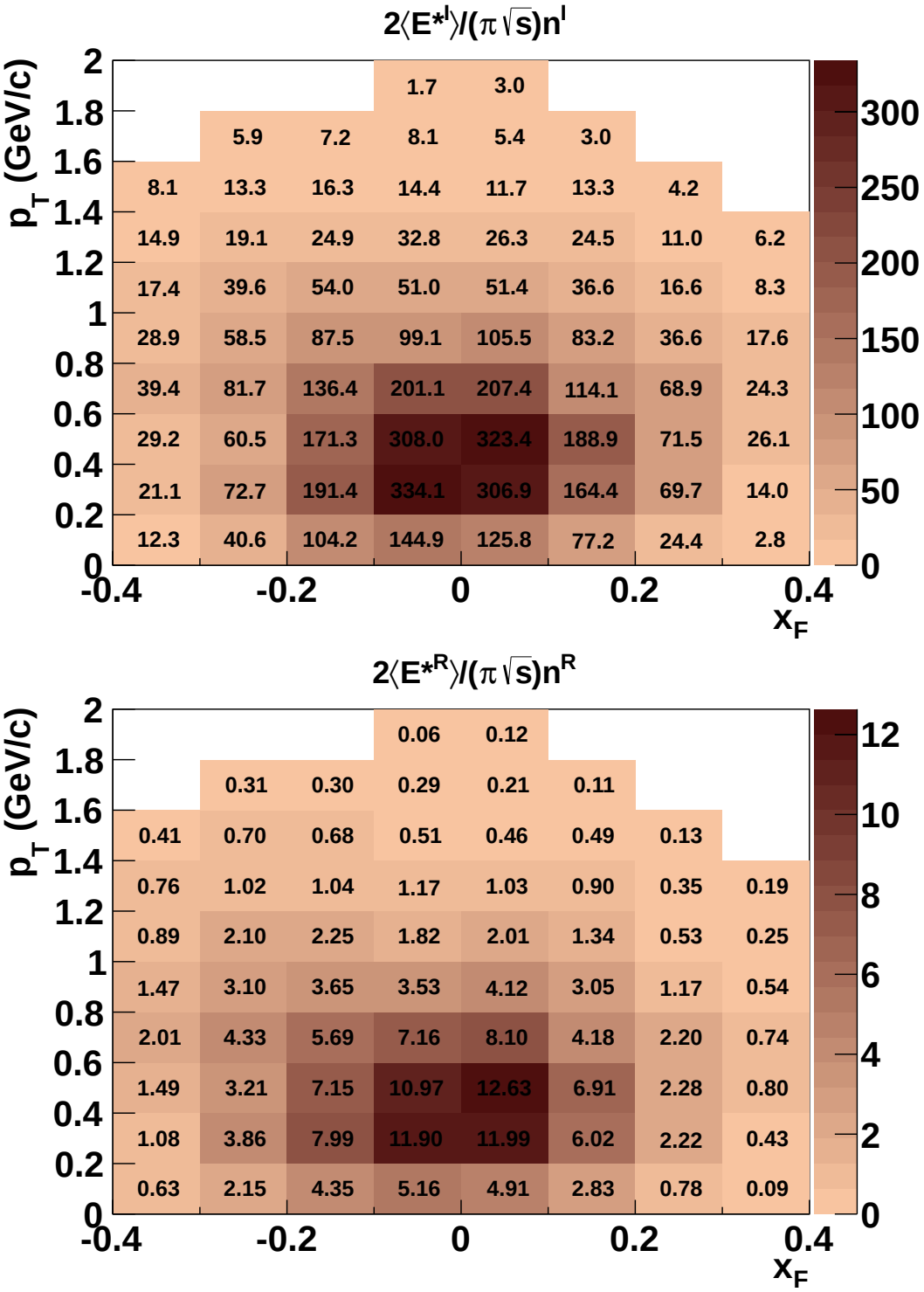

Figure C.15. Raw number of Λ-particles extracted from the experimental data with the LH-inserted configuration of the target (n^I, *top*), and for the LH-removed configuration (n^R, *bottom*) scaled by $2\langle E^*\rangle/(\pi\sqrt{s})$.

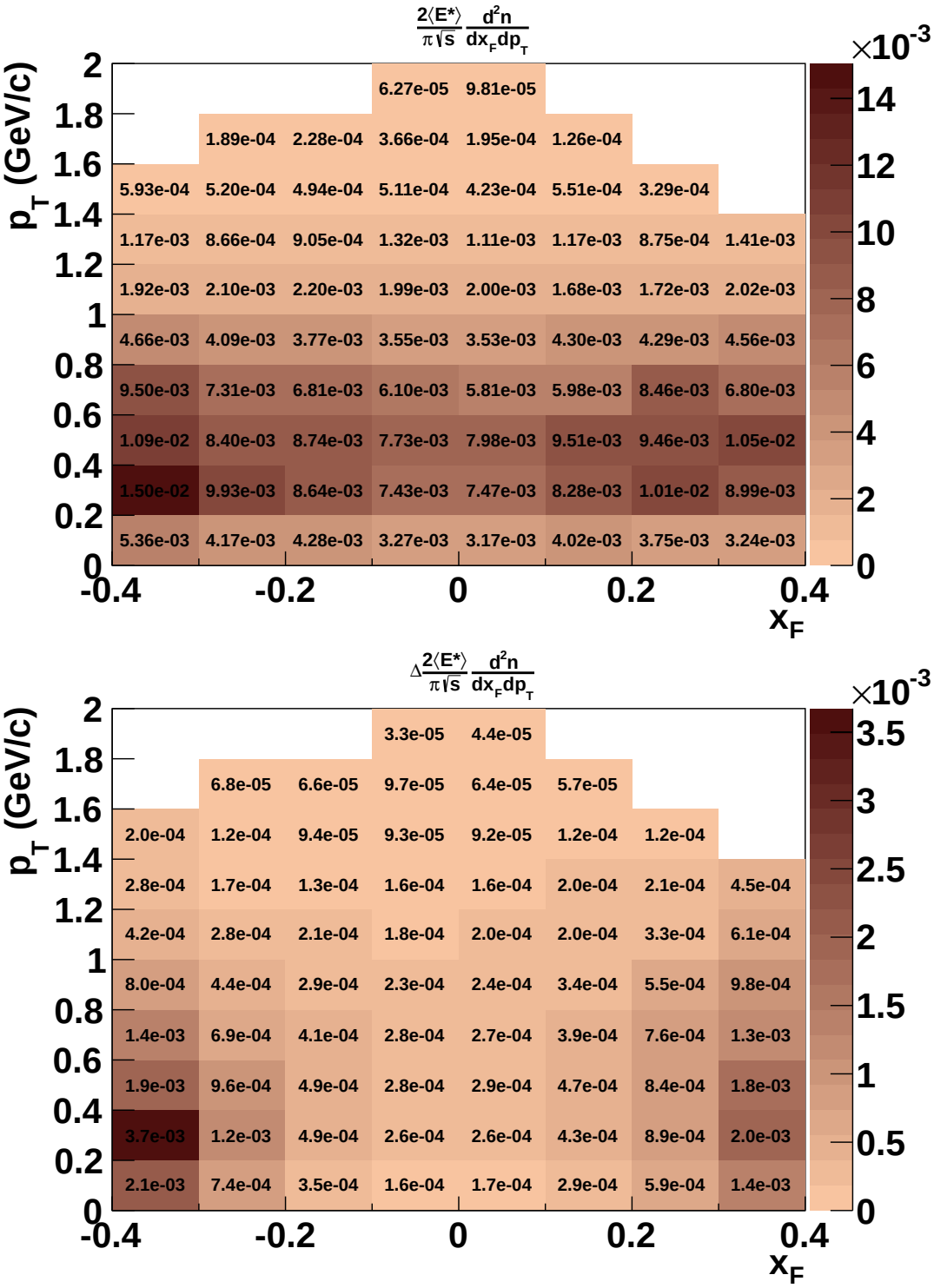

Figure C.16. Corrected spectrum of Λ ($\frac{2\langle E^*\rangle}{\pi\sqrt{s}}\frac{d^2n}{dx_F dp_T}$, *top*), and its statistical error (*bottom*).

C.6 2D-Plots: Dependence on x_F,p_T scaled by $\langle E^* \rangle / (\pi \sqrt{s} \langle p_T \rangle)$

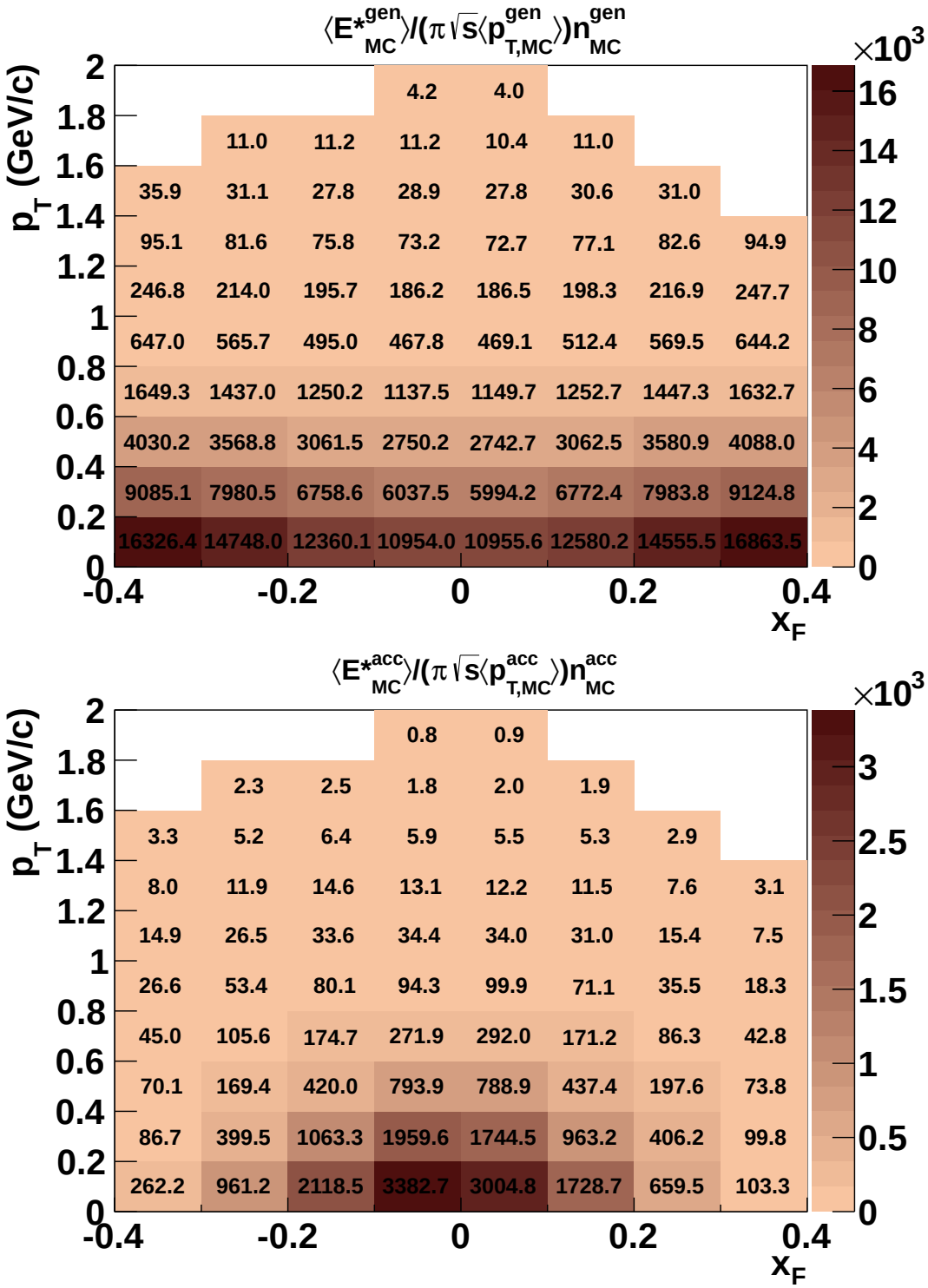

Figure C.17. *Top:* Raw number of generated Λ-particles (n_{MC}^{gen}). *Bottom:* Reconstructed, extracted and accepted number of Λ candidates from the simulation n_{MC}^{acc}. Both observables scaled by $\langle E^* \rangle / (\pi \sqrt{s} \langle p_T \rangle)$.

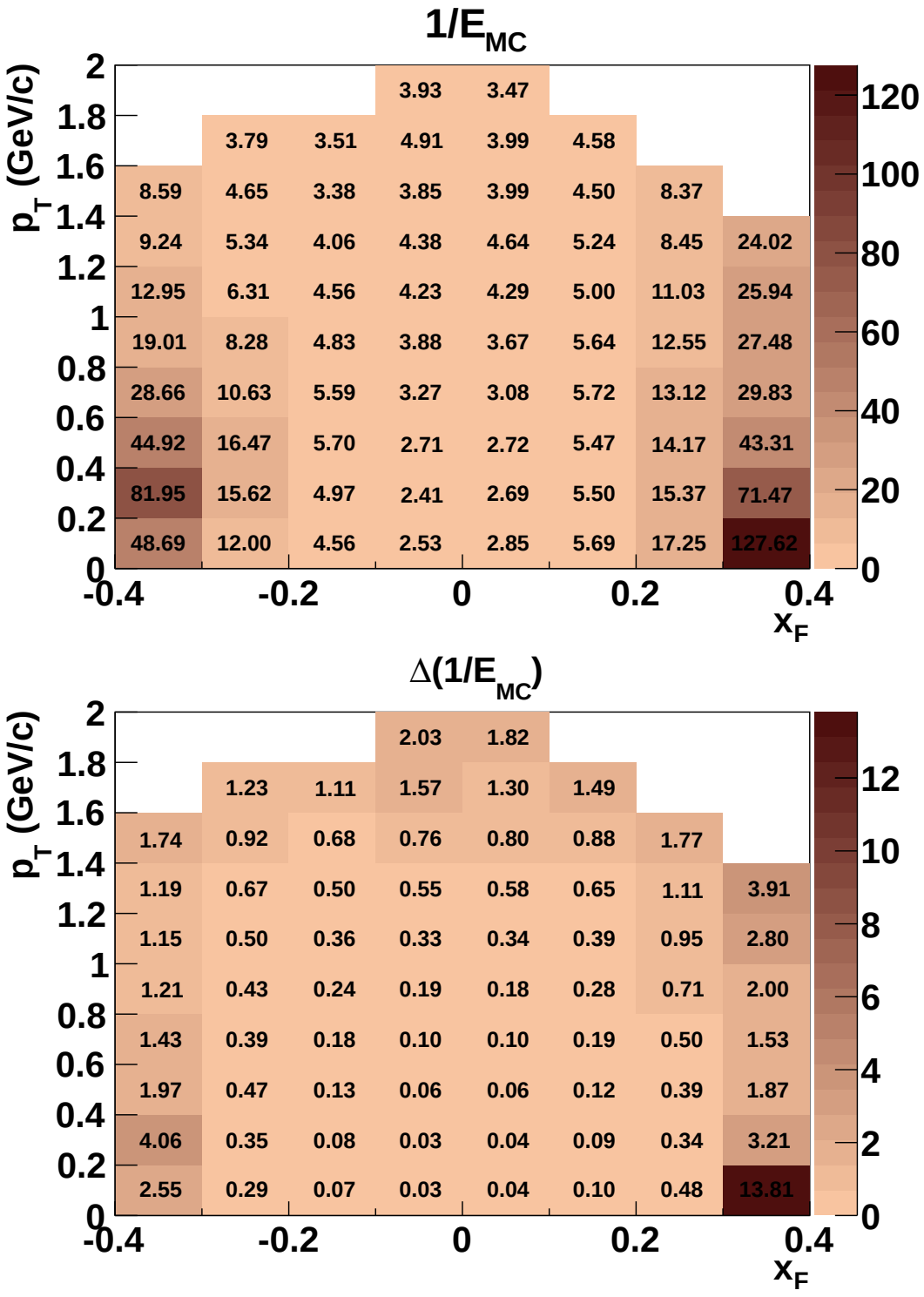

Figure C.18. *Top:* MC-correction factor $1/E_{MC}$. *Bottom:* Statistical error of the correction factor $\Delta(1/E_{MC})$.

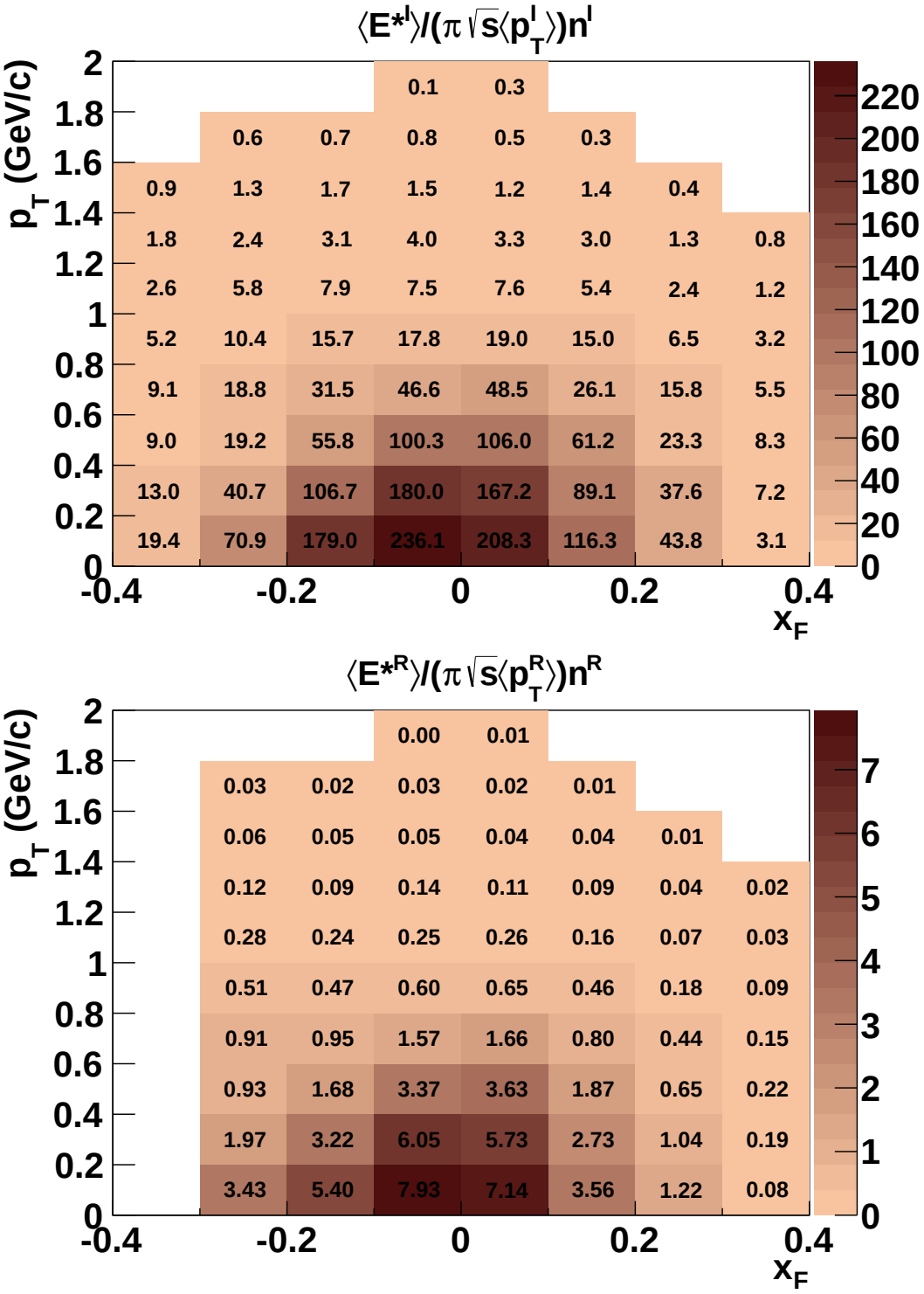

Figure C.19. Raw number of Λ-particles extracted from the experimental data with the LH-inserted configuration of the target (n^I, *top*), and for the LH-removed configuration (n^R, *bottom*) scaled by $\langle E^* \rangle / (\pi \sqrt{s} \langle p_T \rangle)$. The peak at Λ inv. mass was not present at $x_F = -0.35$ for the LH-removed configuration .

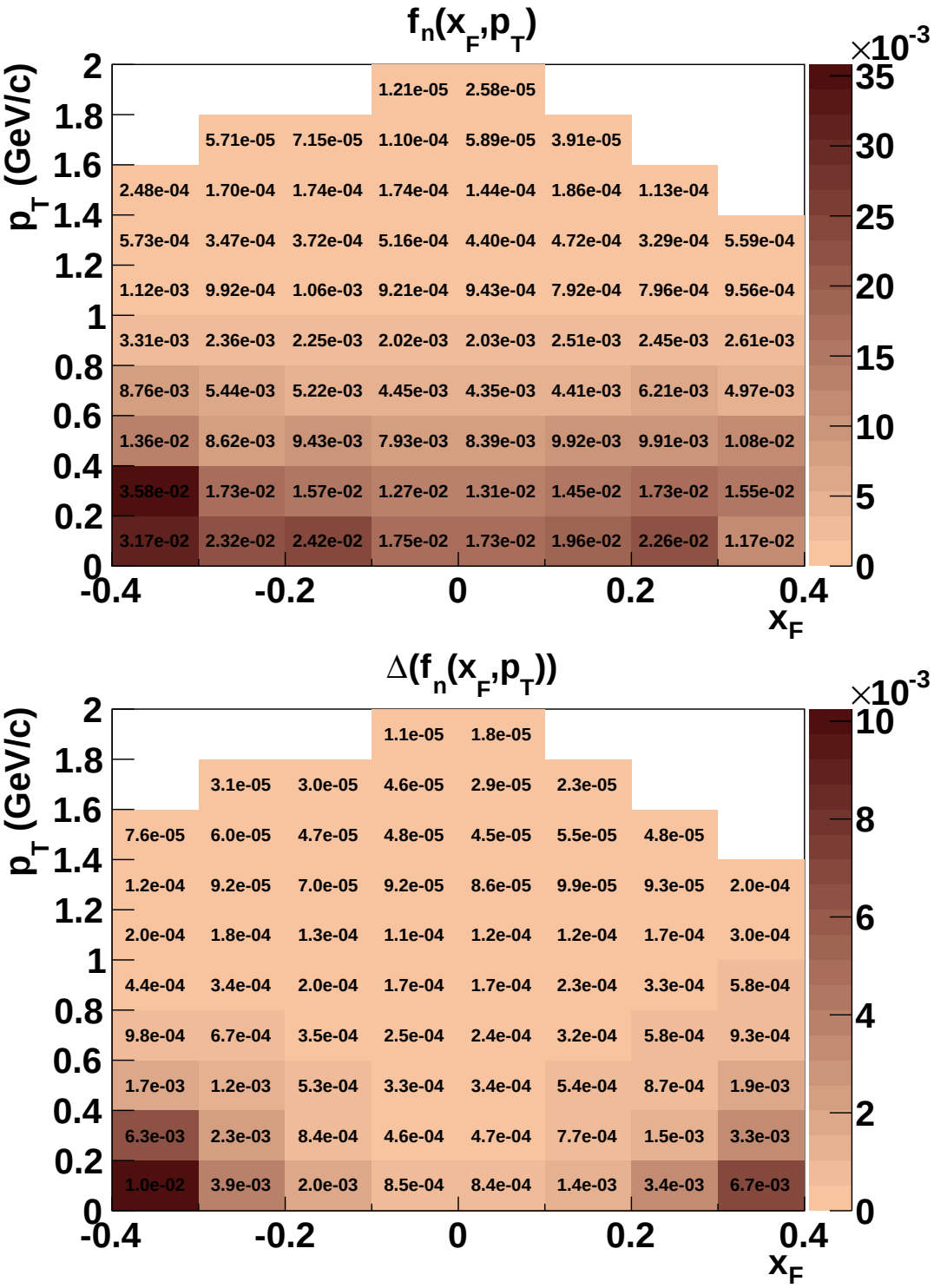

Figure C.20. Corrected invariant spectrum of Λ ($f_n(x_F, p_T)$, *top*), and its statistical error (*bottom*).

C.7 Symmetry checks

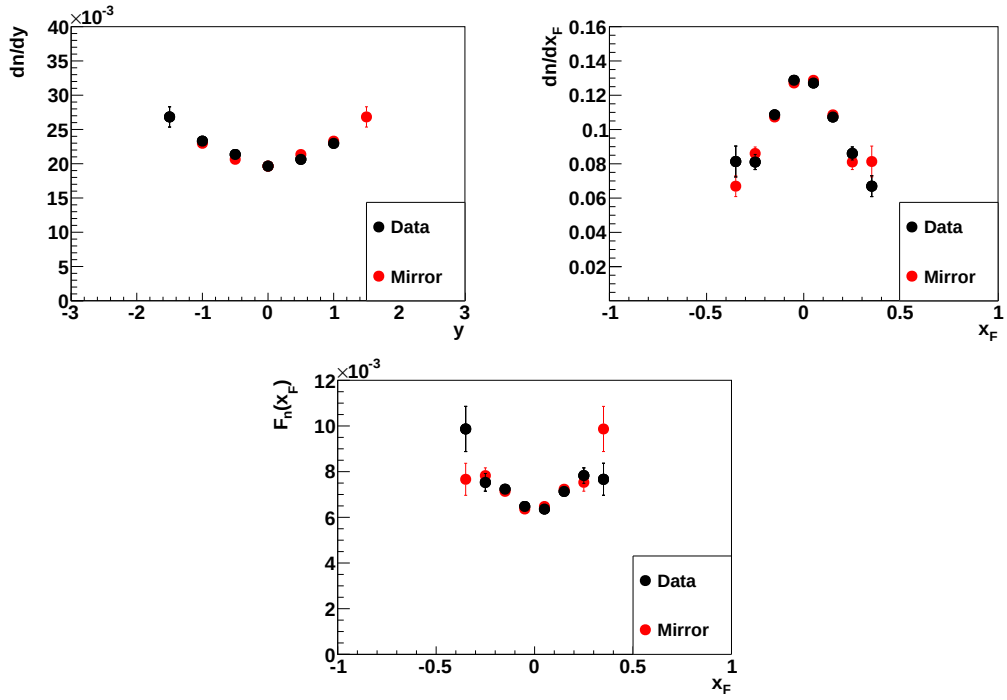

Figure C.21. Forward-backward symmetry test for rapidity distribution dn/dy (*top-left*), Feynman-x distribution dn/dx_F (*top-right*), and invariant Feynman-x distribution $F_n(x_F)$ (*bottom*). Black points correspond to the measured distribution. Red points are mirrored with respect to the mid-rapidity (under exchange $y \rightarrow -y$). Both black and red points agree within the statistical errors.

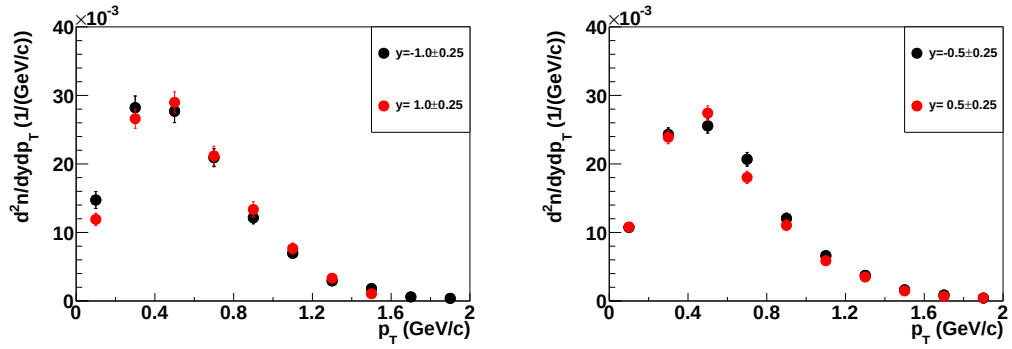

Figure C.22. Forward-backward symmetry for $d^2n/(dydp_T)$. The data for negative rapidity (black points) compared with a superimposed plot for positive rapidity of the same absolute value (red points) show a good agreement.

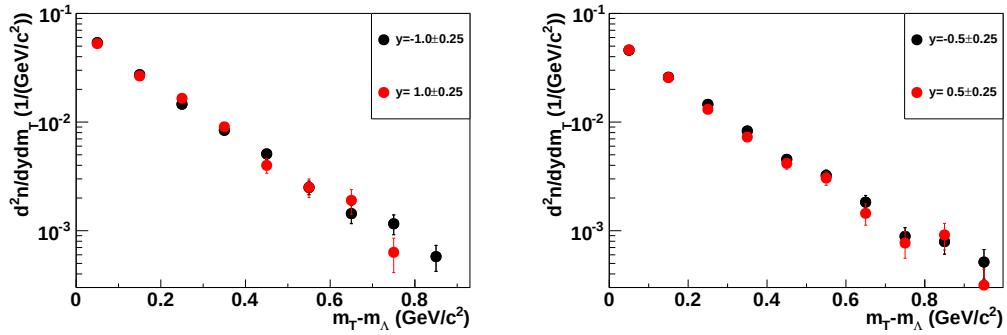

Figure C.23. Forward-backward symmetry for $d^2n/(dydm_T)$. The data for negative rapidity (black points) compared with a superimposed plot for positive rapidity of the same absolute value (red points) show a good agreement.

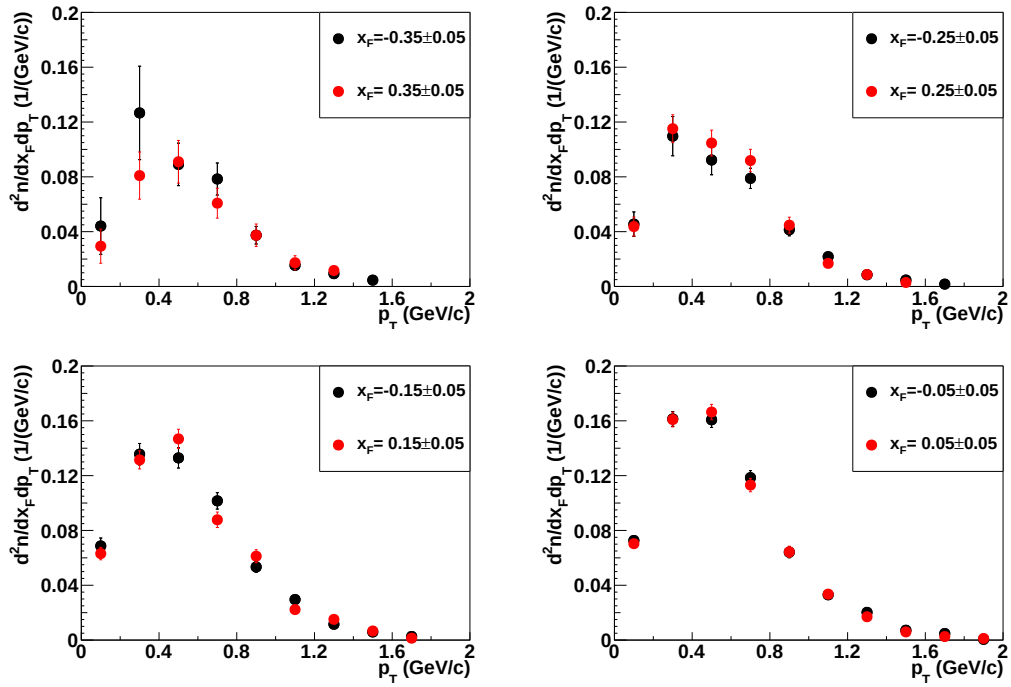

Figure C.24. Forward-backward symmetry for $d^2n/(dx_F dp_T)$. The data for negative x_F (black points) compared with a superimposed plot for positive x_F of the same absolute value (red points) show a good agreement.

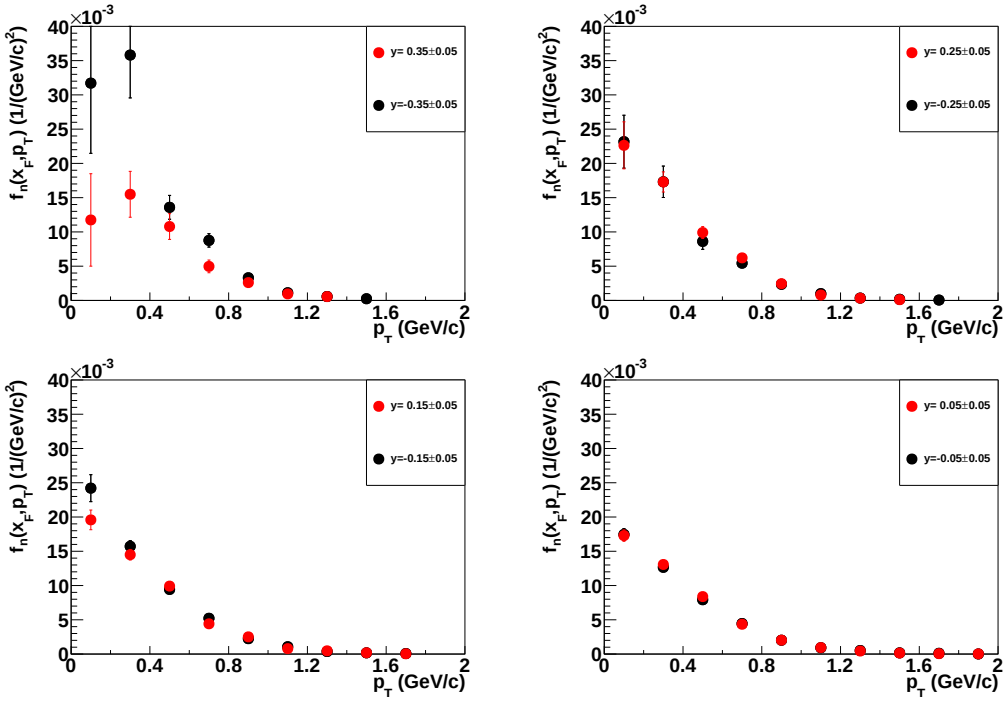

Figure C.25. Forward-backward symmetry for $f_n(x_F, p_T)$. The data for negative x_F (black points) compared with a superimposed plot for positive x_F of the same absolute value (red points) show a good agreement.

Acknowledgements

The work presented in this thesis has been supported by the National Science Centre of Poland (Narodowe Centrum Nauki, Grant No. UMO-2011/03/N/ST2/03691).

My presence at CERN, in particular my duties during data-taking campaingn, as well as my work for magnetic field calibration received support from the National Science Centre of Poland (Narodowe Centrum Nauki, Grant No. UMO-2012/04/M/ST2/0081).

I would like to express my thanks to the people who supported me and helped be in the preparations of this thesis:

- Prof. Dr. habil. Wiktor Zipper, my supervisor and adviser
- Dr. habil. Seweryn Kowalski, my co-supervisor and the director of the heavy-ion research group
- Dr. sc. Tatjana Šuša from Ruďer Bošković Institute in Zagreb, HR. She is the person, who helped me to overcome some difficulties and brought new life to this project during her visit to Katowice. She supervises the weekly meetings on V^0-analysis and helped me much in writing the paper on the results presented in this thesis as a supervisor of the editorial board

In the following I like to thank to the members of the heavy-ion group at the University of Silesia in Katowice for the valuable discussions during our meeting and all over the week:

- Dr. Katarzyna Schmidt
- M.Sc. Kamila Gąsior
- M.Sc. Szymon Puławski
- M.Sc. Emil Kaptur
- M.Sc. Andrzej Grzeszczuk
- B.S. Agnieszka Grzanka
- B.S. Bartosz Łysakowski
- Kamil Wójcik

My special thanks go to the members of the NA49 and NA61/SHINE collaborations

- Prof. Dr. Herbert Ströbele
- Dr. Peter Seyboth

for the best advices and your efforts in providing with extraordinary useful comments to my work.

My thanks go to the other members of the editorial board, which are responsible for the quality of the paper concerning my results and also for your telling comments:

- Prof. Dr. habil. Joanna Stepaniak
- Prof. Dr. habil. Marek Gaździcki, the spokesman of the NA61/SHINE
- Dr. habil. Katarzyna Grebieszkow

Thanks to M.Sc. Jacek Holeczek for revealing the arcana of ROOT-framework.

Thanks to the members of other experimental groups, who made my work in the Division of Nuclear Physics and its Application of the University of Silesia in Katowice very comfortable and friendly:

- Dr. habil. Elżbieta Stephan, who awaken my interest for basic research. Thanks for your readiness to help and for the coffee.
- Dr. Barbara Kłos, who bake delicious cakes
- Dr. habil. Beata Kozłowska
- Dr. Arkadiusz Bubak, who I'm sharing office with, especially for the LaTeX-style I'm using
- M.Sc. Jerzy Dorda

And a number of people I'm not able to mention here.

But what would be my work without my family? Many thanks to my father Horst for your love, support and time spent with me. I am also very grateful to my sister Gabriela and her family for assistance.

You all did a great work!

Bibliography

[1] M. Gell-Mann, *A schematic model of baryons and mesons*, Physics Letters **8** (1964) 214 .

[2] G. Zweig, *An SU(3) model for strong interaction symmetry and its breaking. Version 1*, CERN-TH-401 (1964).

[3] G. Zweig, *An SU(3) model for strong interaction symmetry and its breaking. Version 2*, CERN-TH-412, NP-14146, PRINT-64-170 (1964) 22.

[4] F. Tkachov, *A Contribution to the history of quarks: Boris Struminsky's 1965 JINR publication*, (2009), 0904.0343.

[5] M.Y. Han and Y. Nambu, *Three-Triplet Model with Double* SU(3) *Symmetry*, Phys. Rev. **139** (1965) B1006.

[6] O.W. Greenberg, *Spin and Unitary-Spin Independence in a Paraquark Model of Baryons and Mesons*, Phys. Rev. Lett. **13** (1964) 598.

[7] B. Andersson et al., *Parton fragmentation and string dynamics*, Physics Reports **97** (1983) 31.

[8] F. Halzen and A. Martin, Quarks and leptons: an introductory course in modern particle physics (Wiley, 1984).

[9] D.H. Perkins, Introduction to High Energy Physics, Fourth ed. (Cambridge University Press, 2000), Cambridge Books Online.

[10] D.J. Gross and F. Wilczek, *Ultraviolet Behavior of Non-Abelian Gauge Theories*, Phys. Rev. Lett. **30** (1973) 1343.

[11] A.W. Thomas and W. Weise, The Structure of the Nucleon (Wiley-VCH, 2001).

[12] M. Jezabek and M. Praszalowicz, *Skyrmions and Anomalies. Proceedings, Workshop, Krakow, Poland, February 20-24, 1987*, (1987).

[13] W. Ochs, *The Status of Glueballs*, J.Phys. **G40** (2013) 043001, 1301.5183.

[14] K. Miyamoto, Plasma Physics and Controlled Nuclear Fusion, First ed. (Springer-Verlag Berlin Heidelberg, 2005).

[15] N. Itoh, *Hydrostatic Equilibrium of Hypothetical Quark Stars*, Progress of Theoretical Physics **44** (1970) 291, http://ptp.oxfordjournals.org/content/44/1/291.full.pdf+html.

[16] J.C. Collins and M.J. Perry, *Superdense Matter: Neutrons or Asymptotically Free Quarks?*, Phys. Rev. Lett. **34** (1975) 1353.

[17] E. Shuryak, *Quark-gluon plasma and hadronic production of leptons, photons and psions*, Physics Letters B **78** (1978) 150 .

[18] E. Shuryak, *Quantum chromodynamics and the theory of superdense matter*, Physics Reports **61** (1980) 71 .

[19] J.D. Bjorken, *Highly relativistic nucleus-nucleus collisions: The central rapidity region*, Phys. Rev. D **27** (1983) 140.

[20] R. Hagedorn, *Statistical thermodynamics of strong interactions at high energies*, Supplemento al Nuovo Cimento **III** (1965) 147.

[21] A. Enokizono, Space-time evolution of hot and dense matter probed by Bose-Einstein correlation in Au+Au collisions at $\sqrt{s_{NN}} = 200$ GeV, PhD thesis, Hiroshima University, 2004.

[22] C. Alt et al., *Directed and elliptic flow of charged pions and protons in* Pb + Pb *collisions at* $40A$ *and* $158A$GeV, Phys. Rev. C **68** (2003) 034903.

[23] M.M. Aggarwal et al., *Observation of Direct Photons in Central* $158A$ *GeV* $^{208}P^{208}b + Pb$ *Collisions*, Phys. Rev. Lett. **85** (2000) 3595.

[24] G. Agakichiev et al., *Low-mass* e^+e^- *pair production in 158 A GeV Pb-Au collisions at the {CERN} SPS, its dependence on multiplicity and transverse momentum1*, Physics Letters B **422** (1998) 405 .

[25] B. Lenkeit et al., *New results on low-mass lepton pair production in Pb-Au collisions at 158 GeV per nucleon*, Nuclear Physics A **654** (1999) 627c .

[26] G. Aad et al., *Observation of a Centrality-Dependent Dijet Asymmetry in Lead-Lead Collisions at* $\sqrt{s_{\rm NN}} = 2.76$ TeV *with the ATLAS Detector at the LHC*, Phys. Rev. Lett. **105** (2010) 252303.

[27] T. Matsui and H. Satz, J/ψ *suppression by quark-gluon plasma formation*, Physics Letters B **178** (1986) 416 .

[28] S.V. Afanasiev et al., *Energy dependence of pion and kaon production in central Pb+Pb collisions*, Phys. Rev. C **66** (2002) 054902.

[29] M. Stephanov, K. Rajagopal and E. Shuryak, *Signatures of the Tricritical Point in QCD*, Phys. Rev. Lett. **81** (1998) 4816.

[30] J. Rafelski and B. Müller, *Strangeness Production in the Quark-Gluon Plasma*, Phys. Rev. Lett. **48** (1982) 1066.

[31] J. Rafelski and B. Müller, *Strangeness Production in the Quark-Gluon Plasma*, Phys. Rev. Lett. **56** (1986) 2334.

[32] P. Koch, B. Müller and J. Rafelski, *Strangeness in relativistic heavy ion collisions*, Physics Reports **142** (1986) 167 .

[33] J. Eschke, *Strangeness enhancement in sulphur—Nucleus collisions at 200 A GeV/c*, Acta Physica Hungarica New Series Heavy Ion Physics **4** (1996) 105.

[34] U.W. Heinz and M. Jacob, *Evidence for a new state of matter: An Assessment of the results from the CERN lead beam program*, (2000), nucl-th/0002042.

[35] M. Gazdzicki and M.I. Gorenstein, *On the early stage of nucleus-nucleus collisions*, Acta Phys.Polon. **B30** (1999) 2705, hep-ph/9803462.

[36] E. Fermi, *High Energy Nuclear Events*, Progress of Theoretical Physics **5** (1950) 570, http://ptp.oxfordjournals.org/content/5/4/570.full.pdf+html.

[37] M. Gazdzicki, M. Gorenstein and P. Seyboth, *Onset of deconfinement in nucleus-nucleus collisions: Review for pedestrians and experts*, Acta Phys.Polon. **B42** (2011) 307, 1006.1765.

[38] A. Andronic et al., *Hadron production in ultra-relativistic nuclear collisions: Quarkyonic matter and a triple point in the phase diagram of {QCD}*, Nuclear Physics A **837** (2010) 65 .

[39] A. Andronic, P. Braun-Munzinger and J. Stachel, *Hadron production in central nucleus–nucleus collisions at chemical freeze-out*, Nuclear Physics A **772** (2006) 167 .

[40] F. Karsch, *Lattice QCD at High Temperature and the QGP*, AIP Conference Proceedings **842** (2006).

[41] B. Liu et al., *Hadron-quark phase coexistence in a hybrid MIT-Bag model*, The European Physical Journal A **47** (2011).

[42] R. Venugopalan, *From glasma to quark–gluon plasma in heavy-ion collisions*, Journal of Physics G: Nuclear and Particle Physics **35** (2008) 104003.

[43] F. Gelis et al., *The Color Glass Condensate*, Annual Review of Nuclear and Particle Science **60** (2010) 463, http://dx.doi.org/10.1146/annurev.nucl.010909.083629.

[44] P. de Forcrand and O. Philipsen, *The chiral critical line of N f = 2+1 QCD at zero and non-zero baryon density*, Journal of High Energy Physics **2007** (2007) 077.

[45] P. de Forcrand and O. Philipsen, *The chiral critical point of N_f=3 QCD at finite density to the order $(\mu/T)^4$*, Journal of High Energy Physics **2008** (2008) 012.

[46] L. Ferroni, V. Koch and M.B. Pinto, *Multiple critical points in effective quark models*, Phys. Rev. C **82** (2010) 055205.

[47] M.I. Gorenstein, M. Gaździcki and W. Greiner, *Critical line of the deconfinement phase transitions*, Phys. Rev. C **72** (2005) 024909.

[48] NA61, M. Gazdzicki, Z. Fodor and G. Vesztergombi, CERN preprint SPSC-P-330. CERN-SPSC-2006-034 (2006), revised version submitted on 2006-11-06 12:38:20.

[49] J. Letessier and J. Rafelski, Hadrons and Quark–Gluon Plasma (Cambridge University Press, 2002), Cambridge Books Online.

[50] K. Olive and P.D. Group, *Review of Particle Physics*, Chinese Physics C **38** (2014) 090001.

[51] E. Boldt, D.O. Caldwell and Y. Pal, *Λ^0, ${\theta_1}^0$, ${\theta_2}^0$, and $\overline{\theta}^0$ Lifetimes*, Phys. Rev. Lett. **1** (1958) 148.

[52] A. Pais, *Some Remarks on the V-Particles*, Phys. Rev. **86** (1952) 663.

[53] T. Nakano and K. Nishijima, *Charge Independence for V-particles*, Progress of Theoretical Physics **10** (1953) 581, http://ptp.oxfordjournals.org/content/10/5/581.full.pdf+html.

[54] K. Nishijima, *Charge Independence Theory of V Particles*, Progress of Theoretical Physics **13** (1955) 285, http://ptp.oxfordjournals.org/content/13/3/285.full.pdf+html.

[55] A. Wroblewski, *Average multiplicities of charged particles in meson-proton and proton-proton collisions*, Acta Phys.Polon. **B15** (1984) 785.

[56] A. Mischke, Λ und $\bar{\Lambda}$ Produktion in zentralen Blei-Blei-Kollisionen bei 40, 80 und 158 GeV pro Nukleon, PhD thesis, Johann Wolfgang Goethe-Universität in Frankfurt am Main, 2002.

[57] J. Podolanski and R. Armenteros, *III. Analysis of V-events*, The London, Edinburgh, and Dublin Philosophical Magazine and Journal of Science **45** (1954) 13, http://dx.doi.org/10.1080/14786440108520416.

[58] C. Grupen, *Physics of particle detection*, AIP Conference Proceedings **536** (2000).

[59] N. Abgrall et al., *NA61/SHINE facility at the CERN SPS: beams and detector system*, Journal of Instrumentation **9** (2014) P06005.

[60] P. Coet, N.T. Doble and S. Reucroft, *Beam possibilities for the European Hybrid Spectrometer*, (1981) 28 p.

[61] C. Bovet, S. Milner and A. Placci, CERN preprint CERN-LabII-EA-74-4 (1975).

[62] S. Afanasiev et al., *The {NA49} large acceptance hadron detector*, Nuclear Instruments and Methods in Physics Research Section A: Accelerators, Spectrometers, Detectors and Associated Equipment **430** (1999) 210 .

[63] J. Myrheim and L. Bugge, *A fast Runge-Kutta method for fitting tracks in a magnetic field*, Nuclear Instruments and Methods **160** (1979) 43 .

[64] K. Levenberg, *A method for the solution of certain problems in least squares*, Quart. Applied Math. **2** (1944) 164.

[65] D.W. Marquardt, *An Algorithm for Least-Squares Estimation of Nonlinear Parameters*, Journal of the Society for Industrial and Applied Mathematics **11** (1963) 431.

[66] K. Werner, F.M. Liu and T. Pierog, *Parton ladder splitting and the rapidity dependence of transverse momentum spectra in deuteron-gold collisions at the BNL Relativistic Heavy Ion Collider*, Phys. Rev. C **74** (2006) 044902.

[67] S. E, Λ polarisation in Lead-Lead Collisions, PhD thesis, Universiteit Utrecht, 2003.

[68] R.P. Feynman, *Very High-Energy Collisions of Hadrons*, Phys. Rev. Lett. **23** (1969) 1415.

[69] B. Friman et al., "The CBM Physics Book" (Springer-Verlag Berlin Heidelberg, 2011).

[70] N. Abgrall et al., *Measurements of production properties of K^0_S mesons and Λ hyperons in proton-carbon interactions at 31 GeV/c*, NA61/SHINE Collaboration, Phys. Rev. C **89** (2014) 025205.

[71] R. Hagedorn and J. Ranft, *Statistical thermodynamics of strong interactions at high energies. II. Momentum spectra of particles produced in pp-collisions*, Supplemento al Nuovo Cimento **VI** (1968) 169.

[72] V. Blobel et al., *Multiplicities, topological cross sections, and single particle inclusive distributions from pp interactions at 12 and 24 GeV/c*, Nuclear Physics B **69** (1974) 454 .

[73] T. Šuša, *Cascade production in p+p, p+A and A+A interactions at 158A GeV*, Nuclear Physics A **698** (2002) 491 , 15th Int. Conf. on Ultra-Relativistic Nucleus-Nucleus Collisions (Quark Matter 2001).

[74] V. Ammosov et al., *Neutral strange particle production in pp interactions at 69 GeV/c*, Nuclear Physics B **115** (1976) 269 .

[75] J. Chapman et al., *Production of γ, Λ^0, K^0_S and $\overline{\Lambda^0}$ in pp collisions at 102 GeV/c*, Physics Letters B **47** (1973) 465 .

[76] D. Brick et al., *Inclusive production of neutral strange particles by 147 GeV/c $\pi^+/K^+/p$ interactions in hydrogen*, Nuclear Physics B **164** (1980) 1 .

[77] K. Jaeger et al., *Characteristics of V^0 and γ production in* pp *interactions at 205 GeV/c*, Phys. Rev. D **11** (1975) 2405.

[78] F. LoPinto et al., *Inclusive K^0, Λ^0, $K^{*\pm}(890)$, and $\Sigma^{*\pm}(1385)$ production in* pp *collisions at 300 GeV/ c*, Phys. Rev. D **22** (1980) 573.

[79] M. Asai et al., *Inclusive K^0_S, Λ and $\overline{\Lambda}$ production in 360 GeV/cp p interactions using the European hybrid spectrometer*, Zeitschrift für Physik C: Particles and Fields **27** (1985) 11.

[80] H. Kichimi et al., *Inclusive study of strange-particle production in* pp *interactions at 405 GeV/ c*, Phys. Rev. D **20** (1979) 37.

[81] K. Hagiwara et al., *Review of Particle Properties*, Phys. Rev. D **66** (2002) 010001.

[82] C. Alt et al., *System-Size Dependence of Strangeness Production in Nucleus-Nucleus Collisions at* $\sqrt{s_{NN}} = 17.3$ GeV, Phys. Rev. Lett. **94** (2005) 052301.

[83] C. Alt et al., *Energy dependence of* Λ *and* Ξ *production in central* Pb + Pb *collisions at* $20A, 30A, 40A, 80A$*, and 158A GeV measured at the CERN Super Proton Synchrotron*, Phys. Rev. C **78** (2008) 034918.

[84] T. Anticic et al., *Centrality dependence of proton and antiproton spectra in Pb+Pb collisions at* $40A$ *GeV and* $158A$ *GeV measured at the CERN Super Proton Synchrotron*, Phys. Rev. C **83** (2011) 014901.

[85] S. Bass et al., *Microscopic models for ultrarelativistic heavy ion collisions*, Progress in Particle and Nuclear Physics **41** (1998) 255 .

[86] M. Bleicher et al., *Relativistic hadron-hadron collisions in the ultra-relativistic quantum molecular dynamics model*, Journal of Physics G: Nuclear and Particle Physics **25** (1999) 1859.

[87] B. Andersson, G. Gustafson and H. Pi, *The FRITIOF model for very high energy hadronic collisions*, Zeitschrift für Physik C: Particles and Fields **57** (1993) 485.

[88] B. Nilsson-Almqvist and E. Stenlund, *Interactions between hadrons and nuclei: The Lund Monte Carlo - {FRITIOF} version 1.6 -*, Computer Physics Communications **43** (1987) 387 .

[89] J. Geiss, W. Cassing and C. Greiner, *Strangeness Production in the HSD Transport Approach from SIS to SPS energies*, Nuclear Physics A **644** (1998) 107.

[90] V. Uzhinsky, *Tuning of the GEANT4 FRITIOF (FTF) Model Using NA61/SHINE Experimental Data*, arXiv:1109.6768 (2011).

[91] K. Werner, *The hadronic interaction model {EPOS}*, Nuclear Physics B - Proceedings Supplements **175–176** (2008) 81 , Proceedings of the {XIV} International Symposium on Very High Energy Cosmic Ray Interactions.

[92] M. Gaździcki and O. Hansen, *Hadron-production in nucleon nucleon collisions at 200 GeV/c - a compilation*, Nuclear Physics A **528** (1991) 754.

[93] M. Gaździcki and D. Röhrich, *Strangeness in nuclear collisions*, Zeitschrift für Physik C: Particles and Fields **71** (1996) 55.